FOCUS

ENVIRONMENTAL ENGINEERING SERIES

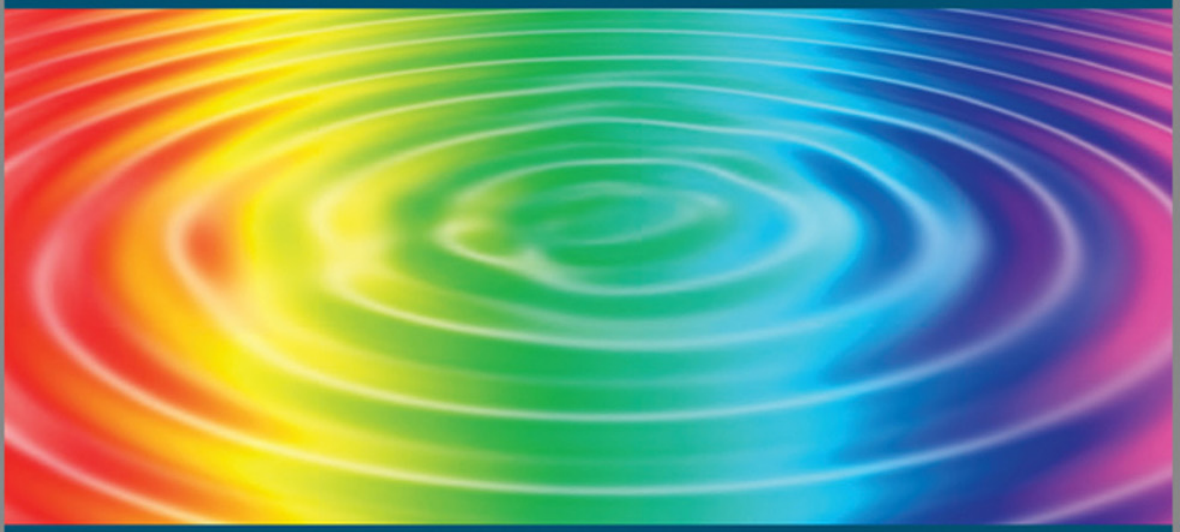

Magnetic Resonance Imaging for Groundwater

Anatoly Legchenko

iSTE

WILEY

Magnetic Resonance Imaging for Groundwater

To the memory of my teacher A.G. Semenov,
the pioneer of SNMR.

FOCUS SERIES

Series Editor François Nicot

Magnetic Resonance Imaging for Groundwater

Anatoly Legchenko

iSTE

WILEY

First published 2013 in Great Britain and the United States by ISTE Ltd and John Wiley & Sons, Inc.

Apart from any fair dealing for the purposes of research or private study, or criticism or review, as permitted under the Copyright, Designs and Patents Act 1988, this publication may only be reproduced, stored or transmitted, in any form or by any means, with the prior permission in writing of the publishers, or in the case of reprographic reproduction in accordance with the terms and licenses issued by the CLA. Enquiries concerning reproduction outside these terms should be sent to the publishers at the undermentioned address:

ISTE Ltd
27-37 St George's Road
London SW19 4EU
UK

www.iste.co.uk

John Wiley & Sons, Inc.
111 River Street
Hoboken, NJ 07030
USA

www.wiley.com

© ISTE Ltd 2013
The rights of Anatoly Legchenko to be identified as the author of this work have been asserted by him in accordance with the Copyright, Designs and Patents Act 1988.

Library of Congress Control Number: 2013948059

British Library Cataloguing-in-Publication Data
A CIP record for this book is available from the British Library
ISSN: 2051-2481 (Print)
ISSN: 2051-249X (Online)
ISBN: 978-1-84821-568-9

FSC
www.fsc.org
MIX
Paper from responsible sources
FSC® C013604

Printed and bound in Great Britain by CPI Group (UK) Ltd., Croydon, Surrey CR0 4YY

Contents

PREFACE vii

ACKNOWLEDGEMENTS ix

CHAPTER 1. SNMR IMAGING FOR GROUNDWATER 1

1.1. Brief history of SNMR development 1
1.2. The basic principles 2
1.3. Magnetic Resonance Sounding 5
1.4. Measuring setup 8
1.5. Geophysical tool for hydrogeologists 12

CHAPTER 2. THE BASICS OF NMR 15

2.1. NMR phenomenon 15
2.1.1. Precession of free spins 15
2.1.2. Macroscopic spin magnetization 16
2.2. NMR relaxation 22
2.2.1. Longitudinal relaxation 22
2.2.2. Transverse relaxation 24
2.2.3. Diffusion in non-homogeneous magnetic field 26
2.3. NMR measurements. 31
2.3.1. Free induction decay (FID) 31
2.3.2. Spin echo (SE) 38

CHAPTER 3. FORWARD MODELING 45

3.1. The imaging equation 45
3.2. The Earth's magnetic field 54
3.3. Modeling typical SNMR signals 59

3.4. 3-D sensitivity of the SNMR loop 68
3.5. Experimental verification 76

CHAPTER 4. INVERSION 85

4.1. The SNMR inverse problem 85
4.2. Linearization 89
4.3. Discretization. 92
4.3.1. The 1-D inverse problem 92
4.3.2. The 3-D inverse problem 105
4.4. Linear inverse problems 113
4.5. Nonlinear inverse problems 115
4.5.1. Inversion of the geomagnetic field variations 116
4.5.2. Inversion of the resistivity distribution 118

CHAPTER 5. LINK BETWEEN SNMR AND AQUIFER PARAMETERS 121

5.1. Parameters used for characterizing an aquifer 122
5.2. Available SNMR estimates on aquifer parameters 126
5.2.1. Detection of groundwater 126
5.2.2. Aquifers and geometry. 128
5.2.3. Storage-related parameters 131
5.2.4. Flow-related parameters 134
5.3. Joint use of SNMR and resistivity data 138

BIBLIOGRAPHY 143

INDEX 155

Preface

The surface Nuclear Magnetic Resonance method (SNMR) is a new application of Nuclear Magnetic Resonance (NMR) for groundwater investigation. It is already an established method, but still, not all of the problems with the method's applications have been resolved; that requires further research effort. The encouragement of geophysicists and hydrologists to use this method in their practical work and the attraction of new researchers to contribute to further developments necessitate a good understanding of SNMR by a broad community of scientists across different disciplines. To contribute to such understanding is the main goal of the book.

SNMR is a product of joint effort by many scientists and engineers who started developing this method in the USSR under the guidance of A.G. Semenov and continued this work all over the world. It is my special pleasure to mention my colleagues who participated at the very beginning of this development: Michael Schirov, Alexandre Pusep, Alexandre Portcelan (Russia), Pierre Valla, Alain Beauce, Jean Bernard, Jean-Michel Baltassat (France), Ugur Yaramanci, Marian Hertrich, Martina Braun (Germany), Jean Roy (Canada), Juan Plata (Spain), Aldo Mazzella and Pete Haeni (USA). I would also like to thank all my colleagues who contributed to the leading knowledge of the method and thus directly or indirectly participated in the writing of this book.

This book has been written based on lectures regularly given by the author to Masters degree students in applied geophysics at Pierre and Marie Curie University (UPMC) in Paris. Readers are assumed to have a geophysical background, and necessary supplementary material in physics and hydrogeology that should allow for a better understanding of the method is provided.

Chapter 1 presents an overview of the method. Those readers who are looking for very general information may put the book aside after reading this chapter. Chapter 2 presents the basics of NMR that should be sufficient for the understanding

of the measurement procedures and for appreciating the information about aquifers that can be obtained with SNMR. The imaging equations and examples of numerical modeling presented in Chapter 3 should help the reader learn about SNMR performance and the physical limitations of the method. Chapter 4 is linked to Chapter 3 and presents analysis of the inverse problem and inversion algorithms actually used for interpretation of field measurements. The fifth and final chapter presents a brief discussion on the link between SNMR derived parameters and aquifer parameters used by hydrogeologists.

This book has been prepared as a textbook and a lot of care has been taken to present the material clearly in order to make the subject more accessible. Consequently, many simplifications are used and the presentation of the method does not include many specific details. It was impossible to present here signal processing, nonlinear and joint inversion, instrumentation, and practical experience and recommendations. Readers are invited to read additional literature, which is easily available. If at least some part of the audience reads this book with interest, then the author will consider his goal as fully achieved.

Anatoly LEGCHENKO
September 2013

Acknowledgements

I am thankful to all my colleagues in different countries who spent time and energy in making this book possible.

I acknowledge the IRD (*Institut de recherche pour le développement*), a French research organization, which continuously supported my work.

I am also grateful to the following journals for permission to use tables and figures.

Ground Water (published by the National Ground Water Assosciation (NGWA), USA)

Table 5.2, Figures 5.14 and 5.15

LEGCHENKO A., BALTASSAT J.-M., BOBACHEV A., MARTIN C., ROBAIN H., VOUILLAMOZ J.-M., "Magnetic resonance sounding applied to aquifer characterization", *Ground Water*, 42, 363-373, Table 2, Figures 11 and 12, 2004.

Boletin Geológico y Minero (published by the *Instiuto Geológico y Minero España* in collaboration with both the Spanish and international world of Earth Sciences).

Figures 5.6, 5.10 and 5.12

VOUILLAMOZ J.-M., BALTASSAT J.-M., GIRARD J.-F., PLATA J., and LEGCHENKO A., "Hydrogeological experience in the use of MRS", *Boletin Geológico y Minero*, 118 (3), 531-549, ISSN: 0366-0176, Figures 1, 3 and 4, 2007.

1

SNMR Imaging for Groundwater

1.1. Brief history of SNMR development

Surface Nuclear Magnetic Resonance (SNMR) imaging is a non-invasive geophysical technique developed for groundwater investigation. This method was initially used for investigating a homogeneous subsurface. In a one-dimensional (1-D) implementation, the subsurface is assumed to be horizontally stratified and the method is known as the Magnetic Resonance Sounding (MRS) method or Surface Nuclear Magnetic Resonance (SNMR). In France, the name RMP (*sondage par la Résonance Magnétique Protonique*) is used.

The MRS method was developed in Russia in the early 1980s by a team of Russian scientists under the guidance of A.G. Semenov. Their research program started from the Varian patent [VAR 62] where using the Nuclear Magnetic Resonance phenomenon (NMR) was proposed for non-invasive detection of proton-containing liquids (hydrocarbons or water) in the subsurface. The very first MRS instrument, named HYDROSCOPE, was built in 1981 [SEM 89]. The method was used in Russia and has been tested in other countries: [SCH 91], [GOL 94], [LIE 94], [LEG 95] and [GEV 96]. In 1996, IRIS Instruments (France), in cooperation with the Bureau de Recherches Géologiques et Minières (BRGM (The French Geological Survey), France) and the Institute of Chemical Kinetics and Combustion (ICKC, Russia), released the first commercial MRS instrument (NUMIS), thus rendering MRS commercially available and easily accessible for the international scientific community. Since then, MRS has been intensively tested by different teams and in different countries. A two-dimensional (2-D) implementation named the Surface Magnetic Resonance Tomography or 2D-SNMR was developed around 2005 [HER 07], which was further extended to the three-dimensional (3-D) applications named 3D-SNMR [LEG 11]. MRS equipment was also improved and MRS instruments of the new generation were developed in France, USA, Germany and China.

Today, SNMR imaging for groundwater is an emerging geophysical method which is routinely used for groundwater investigations but it is still a subject of research and development for an international community composed of geophysicists and hydrogeologists.

1.2. The basic principles

The phenomenon of nuclear magnetic resonance (NMR) consists of selective absorption and transmission by atomic nuclei of electromagnetic energy of a specific frequency, particular to different nuclei. This phenomenon was discovered in 1946. The Nobel Prize in Physics, 1952, was jointly awarded to Felix Bloch and Edward Mills Purcell for their development of new methods for nuclear magnetic precision measurements and discoveries in connection therewith: [BLO 46] and [PUR 46]. The NMR phenomenon can be observed in nuclei possessing both magnetic moments and angular momentum. The SNMR method is based on the observation of the NMR phenomenon in hydrogen or protons (H^1) contained in water and oil [ABR 61]. In the first 200 m of the subsurface, the probability of finding oil reservoirs is negligibly small and hence SNMR is principally targeted at groundwater. The resonance behavior of proton magnetic moments in the geomagnetic field ensures that the method is selective and sensitive only to groundwater. Thus, a non-invasive detection of subsurface water is the competitive advantage of SNMR compared with other geophysical tools used for hydrogeological investigation. SNMR is a large-scale method, and the investigated volume can be approximated by a cube of $1.5 \times a$, where $10 \le a \le 150$ m is the side of a square loop.

In the classical model, nuclei are represented as macroscopic magnetic moments $\mathbf{M}$. A typical scheme of magnetic resonance measurement consists of three phases (Figure 1.1). In the natural, non-perturbed state (equilibrium position), all magnetic moments $\mathbf{M}$ are oriented along the static magnetic field $\mathbf{B}_0$ and do not produce any measurable signal. Nuclei are able to absorb electromagnetic energy at the Larmor frequency $f_0 = \gamma B_0 / 2\pi$. The gyromagnetic ratio γ has a specific value for each type of nucleus, and hence the Larmor frequency is a physical property of the nuclei. Thus, when an external electromagnetic field is applied to a sample, the nuclei absorb the energy and magnetic moments precess from their equilibrium. After the external field is cut off, they return to their initial position and generate a magnetic field, which is also oscillating at the Larmor frequency. This field can be measured, and then analyzed. For data acquisition, a pulse of current, oscillating at the Larmor frequency is generated in the transmitting coil. The magnetic resonance response is

recorded at the same frequency after the pulse is terminated. A typical scheme of the data acquisition is presented in Figure 1.1.

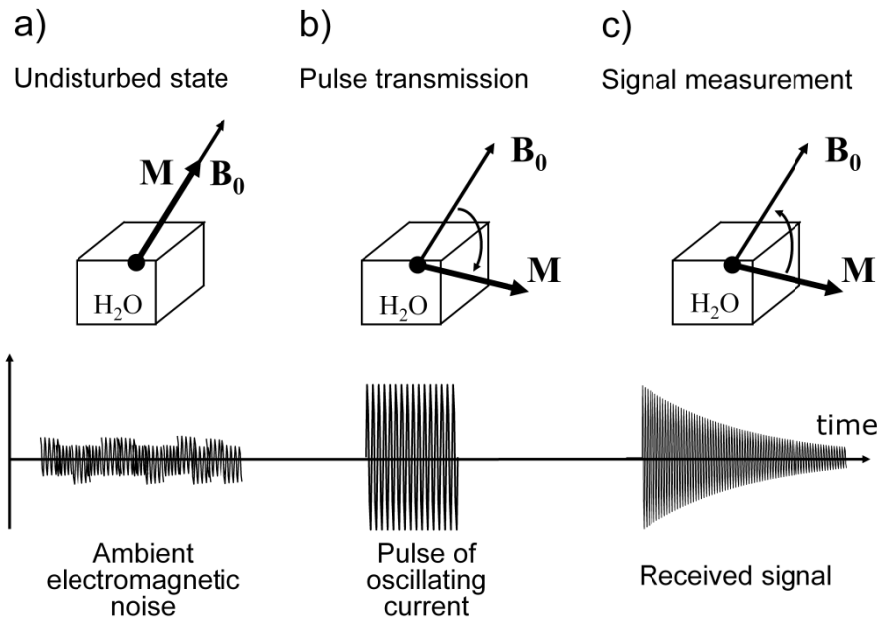

Figure 1.1. *Typical phases of a magnetic resonance experiment (top) and corresponding magnetic resonance measurements (bottom)*

Electromagnetic noise is recorded during a few hundreds of milliseconds before the outgoing pulse. After an instrument delay, called the "dead time", the magnetic resonance signal is then measured. Comparison of records before and after the pulse determines whether a magnetic resonance response is detected or not. As noise is independent of the transmitted pulse, a stacking procedure is used to improve the signal-to-noise ratio. The amplitude, the relaxation times and the phase of the magnetic resonance signal are measured.

A similarity between the well-known proton magnetometer and the SNMR is shown in Figure 1.2. The magnetometer is used for measuring the magnitude of the Earth's magnetic field using the linear relationship between the Larmor frequency and the magnetic field: $f_0=\gamma B_0/2\pi$. A container with kerosene or some other

hydrogen-rich liquid (or just water) is put inside the acquisition coil of the magnetometer, and we are looking only for the frequency of the magnetic resonance signal. For performing SNMR measurements, the coil is enlarged and becomes a wire loop that is spread out on the surface and groundwater acts as a hydrogen-containing liquid. The Larmor frequency may be known from the magnitude of the Earth's magnetic field when measured with a magnetometer. Thus, when tuning the SNMR system at the Larmor frequency we are looking for the magnetic resonance response that allows us to either detect groundwater, or may confirm the absence of water in the investigated volume of the subsurface.

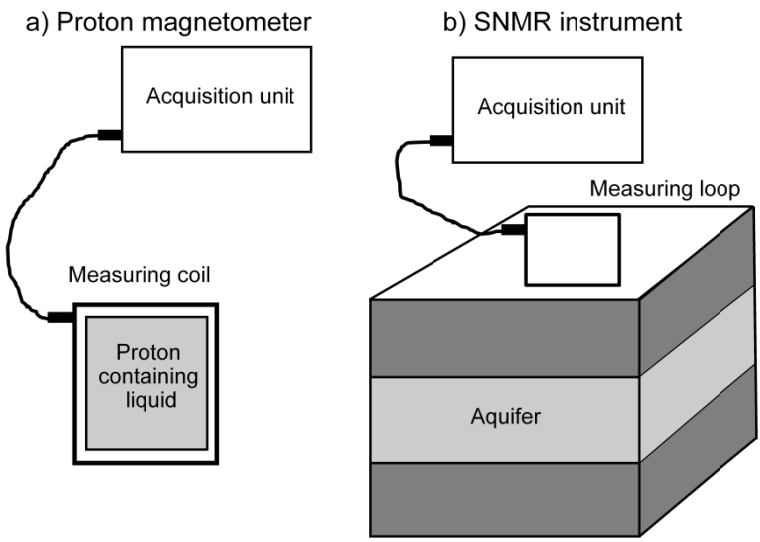

Figure 1.2. *Similarity between SNMR tool and proton magnetometer*

Since only protons of groundwater can generate the magnetic resonance signal at this frequency, SNMR is really a direct method for groundwater detection from the surface.

It will be shown later that the amplitude of the magnetic resonance response is proportional to the volume of the investigated sample and to the square of the static magnetic field $E_0 \sim B_0^2 V$. Thus, to increase the signal-to-noise ratio, the static magnetic field and/or the volume of the sample should be increased. Consequently, NMR instruments can be classified according to the volume of the investigated sample (Figure 1.3).

Investigated volume		
V~mm^3 Artificial static magnetic field Lab. NMR	V~cm^3 Artificial static magnetic field NMR logging	V~m^3 Geomagnetic field SNMR

Figure 1.3. *Classification of NMR applications by investigated volume*

In the majority of applications, the static magnetic field is artificially created in a relatively small volume. Chemical NMR spectrometers and Magnetic Resonance Imaging (MRI) instruments used in medicine, which offer a very high spatial resolution and are commonly used in laboratories, operate in a broad artificial static magnetic field and a small sample volume (a few mm^3). Much larger sample volumes (a few cm^3) and smaller artificial static magnetic fields are used in borehole geophysics, whereas only a limited number of applications use the Earth's magnetic field [PAC 54; CAL 82; STE 90; CAL 98; TAI 02; APP 06; MIC 10]. SNMR equipment operates in the geomagnetic field and uses sample volumes of a few thousand m^3.

1.3. Magnetic Resonance Sounding

For demonstrating SNMR experiments let us use the classical model [ABR 61].

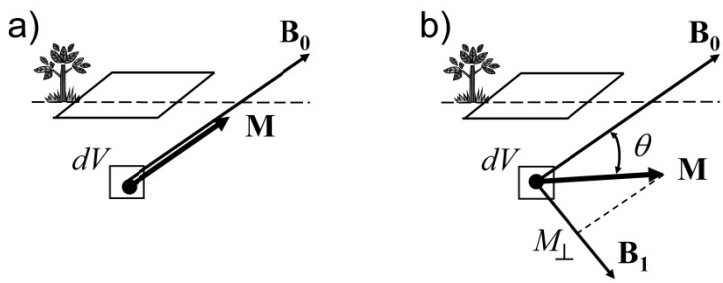

Figure 1.4. *Macroscopic magnetic moment* **M** *of the volume dV below SNMR loop: a) equilibrium position along with the static magnetic field* $\mathbf{B_0}$*; b) position after the excitation pulse* $\mathbf{B_1}$ *and the projection of* **M** *on the plan transversal to* $\mathbf{B_0}$

The macroscopic magnetic moment $\mathbf{M}$ of the volume *dV* which is located below a surface loop is oriented along the static magnetic field $\mathbf{B}_0$ as shown in Figure 1.4. The Earth's magnetic field acts as the static field $\mathbf{B}_0$. A pulse of alternating current generated in the loop produces an electromagnetic field within the volume *dV*. The frequency of the current is set as equal to the resonance frequency for protons in the geomagnetic field (Larmor frequency). The component of the loop's magnetic field $\mathbf{B}_1$ transversal to the Earth's magnetic field $\mathbf{B}_0$ makes rotating the magnetic moment $\mathbf{M}$ in the plane perpendicular to the plane ($\mathbf{B}_0, \mathbf{B}_1$) at the angle $\theta = \gamma B_1 \tau$ (flip angle), where τ is the pulse duration and γ is the gyromagnetic ratio. Magnetic resonance signal induced in the loop is proportional to the projection of $\mathbf{M}$ on $\mathbf{B}_1$: $E_0 \sim M_\perp$. As $M_\perp = M\sin(\theta)$, the signal also depends on θ and hence $E_0 \sim \sin(\theta)$. For the same loop the flip angle θ depends on two parameters: current in the loop I_0 and distance between the loop and the sample *dV*. I_0 is known and hence, by measuring θ, we obtain information on the depth of water saturated formations. A magnetic resonance signal is generated by water molecules and simple observation of the NMR response using an SNMR field setup is sufficient for reliably detecting groundwater. The maximum sensitivity of the method with regard to groundwater will be achieved when the flip angle $\theta = 90°$ (Figure 1.4).

However, SNMR can also be used in a sounding mode. In this case depth to water saturated formations can be derived from SNMR measurements. Implementation of a Magnetic Resonance Sounding (MRS) is schematically presented in Figure 1.5. Two distinct cases are presented: a shallow aquifer and a deep one. If the pulse duration is fixed, then for the same current in the loops the flip angle θ of the macroscopic magnetic moment $\mathbf{M}$ will be larger for a shallow water saturation formation than for a deeper one. One sounding consists of measuring the amplitude of the SNMR signal E_0 for different values of the current I_0 in the loop. The amplitude is then plotted versus the current, as shown in Figure 1.5. The shape of the sounding curve $E_0(I_0)$ allows us to resolve the depth to the aquifer.

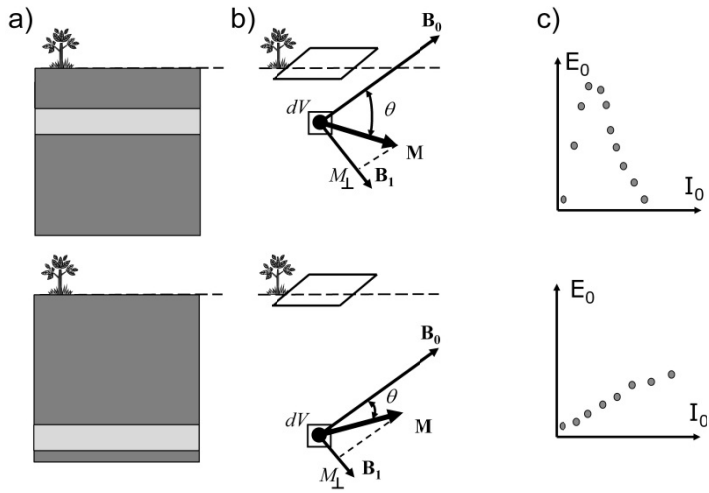

Figure 1.5. *Schematic presentation of SNMR sounding (MRS): a) aquifer location (top – shallow aquifer, bottom – deep aquifer); b) position of the macroscopic magnetic moment* **M** *after the excitation pulse with the current I_0 considering shallow (top) and deep (bottom) aquifers; c) amplitude of SNMR signal versus current in the loop for shallow (top) and deep (bottom) aquifers*

For performing SNMR sounding, a wire loop is laid out on the ground, normally in a circle or a square with a size of between 10 and 200 m (diameter or side respectively). The depth of investigation is proportional to the loop size (Figure 1.6).

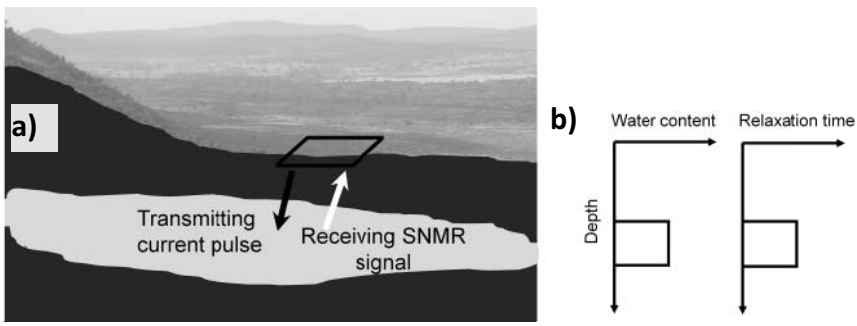

Figure 1.6. *SNMR system: a) field setup; b) measuring scheme; c) results*

The loop is then energized by a pulse of alternating current $i(t) = I_0 \cos(\omega_0 t)$.

The frequency of the current is equal to the Larmor frequency of the protons in the geomagnetic field. The Larmor frequency is obtained from measurements of the

geomagnetic field (B_0) on the surface using a proton magnetometer. Depending on the global geographical location of the investigated area, the geomagnetic field varies between approximately 20,000 and 60,000 nT, and the Larmor frequency correspondingly varies between 800 and 2,800 Hz. The pulse causes precession of spin magnetization of the protons in groundwater around the geomagnetic field, which creates an alternating magnetic field that can be measured after the pulse is terminated (the free induction decay method). SNMR can be used in the coincident transmitting/receiving (Tx/Rx) loop mode when the same loop is used as a transmitter and receiver or in a separated Tx and Rx mode when one loop is a transmitter and another a receiver. Oscillating with the Larmor frequency, the MRS signal has an exponential envelope and depends on the pulse moment $q = I_0 \tau$ with I_0 and τ being respectively the amplitude and duration of the pulse. Measurements of the magnetic resonance signal are performed, varying the pulse moment and then inversion of the data reveals the distribution of the water content and of the relaxation time in the subsurface. The depth interval in the sounding log with increased values of the water content and relaxation time correspond to an aquifer.

1.4. Measuring setup

SNMR field setup is composed of one or more surface loops. One loop is the transmitting loop (Tx) and one or more loops are the receiving loops. The coincident loop configuration allows us to use the same loop for both transmitting and receiving (Tx/Rx loop). The commonly used loops are shown in Figure 1.7.

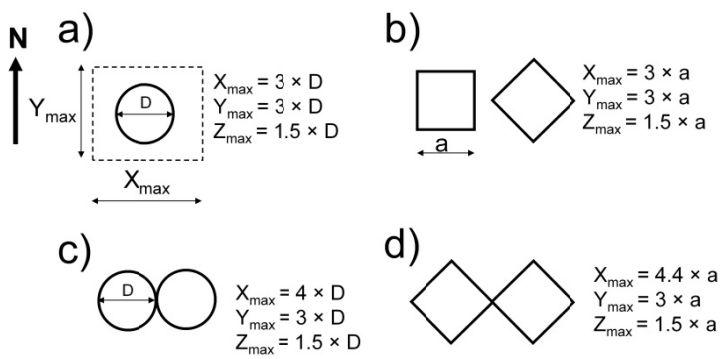

Figure 1.7. *SNMR field setup: a) circular loop; b) square loop; c) figure-eight circular loop; d) figure-eight square loop*

The loop sizes may vary between a=20 m and a=150 m. Loops larger than 80 m usually have one turn and small loops may have 2 to 5 turns of wire. Each transmitting loop is made of electrical cable with a cross-section of more than 6 mm^2. Such a thick wire allows generating large current pulses (up to 600 A). Special attention should be paid to the electrical insulation of the wire because of a high-pulse voltage (up to 4 kV). The volume affected by each Tx loop depends on the loop size and shape. Approximate volume affected by different loops is shown in Figure 1.7.

For a wire of fixed length, circular and square loops allow getting the maximum amplitude of SNMR signal and the maximum depth of investigation. Often, the figure-eight loop can be used for improving the signal-to-noise ratio (S/N). The figure-eight-shaped loop consists of two equal squares or circles connected as shown in Figure 1.8.

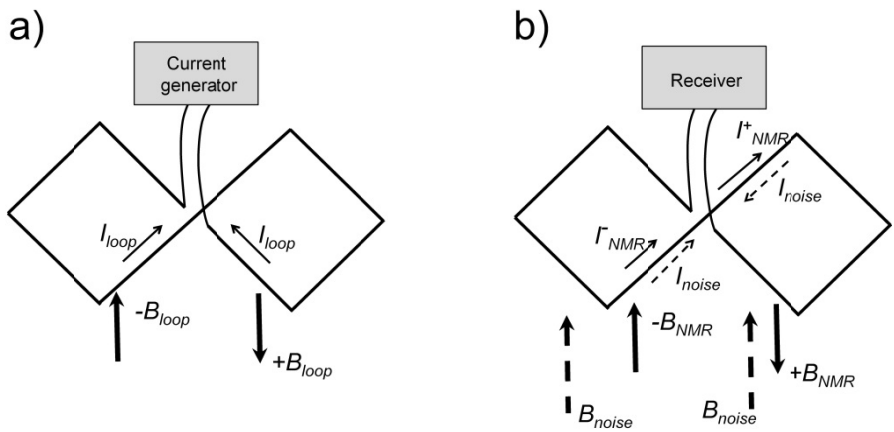

Figure 1.8. *Principle of the noise cancellation with the figure-eight loop: a) transmitting current pulse; b) receiving SNMR signal and noise*

Indeed, the magnetic fields generated by the squares of the figure-eight loop (B_{loop}) are oriented in the opposite directions (Figure 1.8a). Consequently, SNMR signals induced in each square (I^-_{NMR} and I^+_{NMR}) also have inverse polarity (Figure 1.8b). Note that noise induced in each square has the same polarity. The squares of the loop are connected so that the currents induced in each square are subtracted and the signal is doubled, but the noise is canceled. Using the figure-eight loop one may get up to a tenfold improvement in S/N [TRU 95].

For canceling noise with the figure-eight loop, the principal axis of the loop has to be set parallel to the noise source (Figure 1.9a). Otherwise, the noise induced in

the squares of the loop will be not equal and the noise cancellation may be not efficient (Figure 1.9b).

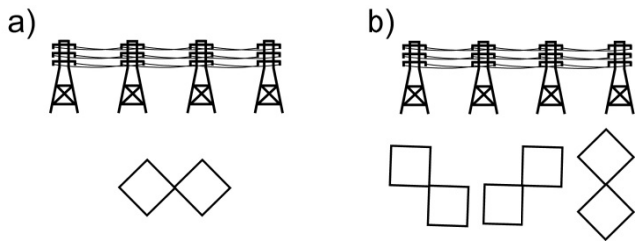

Figure 1.9. *The orientation of the figure-eight loop relative to a power line for canceling a magnetic field generated by the power line: a) correct orientation; b) incorrect orientations*

The figure-eight loop is efficient when it can be oriented so that the squares are symmetric relative the noise source. It is relatively easy to obtain when only one power line is located in the investigated area. However, the power line may change direction, or two or more power lines may cross the area (Figure 1.10). In this case the figure-eight loop may be inefficient, but the signal-to-noise ratio may be improved by using one measuring loop and one or more additional reference loops. The reference loops should be located far enough from the transmitting loop to measure only noise. In this configuration, voltages induced in each loop are recorded separately and special processing algorithms allow subtracting noise from signal records [WAL 08].

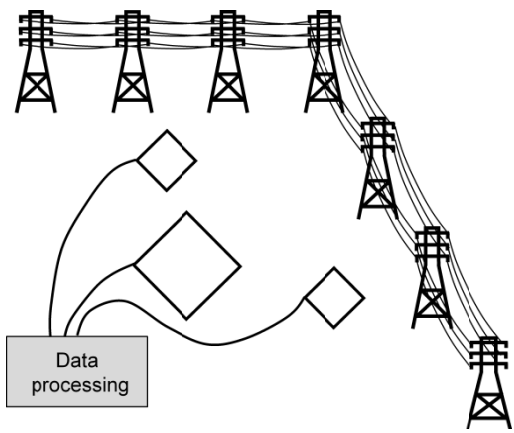

Figure 1.10. *Measuring setup consisting of one Tx/Rx loop (large square) and two noise measuring loops (small squares)*

If SNMR loops are separated at the distance of more than *a* (Figure 1.7) then measurements within each loop are independent and these measurements should be considered as a 1-D survey (Figure 1.11a). When loops are set side by side (Figure 1.11b) measurements can be interpreted as a 2-D profile. The resolution of a 2-D survey may be improved by using half-overlapped loops (Figure 1.11c). Note that setting loops closer than the half-overlapped loops will increase the labor proportionally to the number of the loops without proportional improvement in resolution.

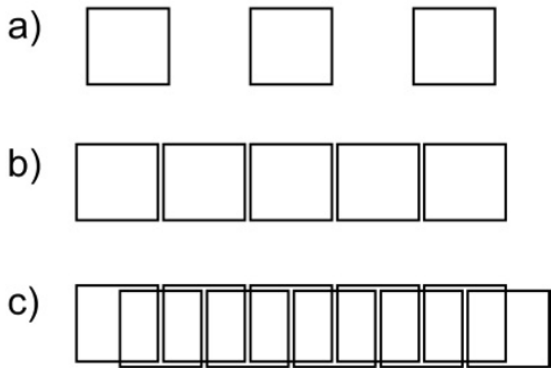

Figure 1.11. *SNMR field setup: a) 1-D; b) 2-D minimal coverage; c) 2-D optimal coverage*

3-D field setups are shown in Figure 1.12. In order to be well resolved, an investigable anomaly should be located within the area occupied by SNMR loops. The half overlapped loop setup seems to be a good compromise between the resolution, and the time and labor consumption.

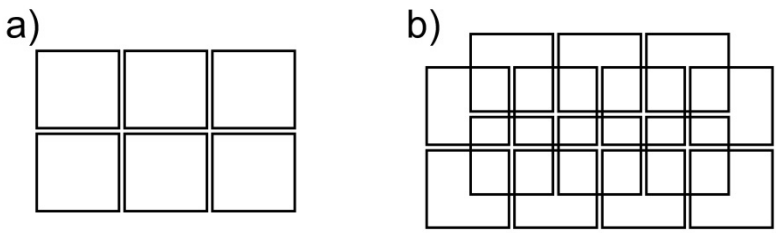

Figure 1.12. *SNMR field setup: a) 3-D minimal coverage; b) 3-D optimal coverage*

1.5. Geophysical tool for hydrogeologists

SNMR imaging is a non-invasive geophysical method that can be used independently or in conjunction with other geophysical and hydrogeological tools for groundwater investigation [ROY 03; LUB 04]. SNMR has a selective sensitivity to groundwater and could provide complementary hydrogeological information about aquifers. The following features of the method render it particularly efficient for hydrogeological surveying: the reliable detection of groundwater, information on the aquifer geometry and the estimation of aquifers' hydrodynamic properties.

Detection of groundwater in the area investigated with SNMR loop is the most reliable parameter provided by SNMR. Correct use of the measuring procedure and experimental setup allows unambiguous identification of the magnetic resonance signal and thus of groundwater. There is no other source that could produce a signal that could mislead interpretation of SNMR results. If the magnetic resonance signal is not observed and external electromagnetic noises are low, then SNMR points to the absence of aquifer formation. The threshold of water detection in the rocks with hydraulic permeability of more than 10^{-5} m/s depends on the measuring conditions, but typically the water content should be more than 0.5%. Water in rocks with hydraulic conductivity of less than 10^{-6} m/s (clay, for example) is undetectable with SNMR. In the SNMR log, low permeable rocks are presented as dry intervals.

Aquifers' geometry can be derived from distribution of the water content in the subsurface provided by SNMR inversion. Depending on the survey design, SNMR results can be presented as a 1-D, 2-D or 3-D distribution of the water content and relaxation times. Figure 1.11 shows discretization of the subsurface for these three cases.

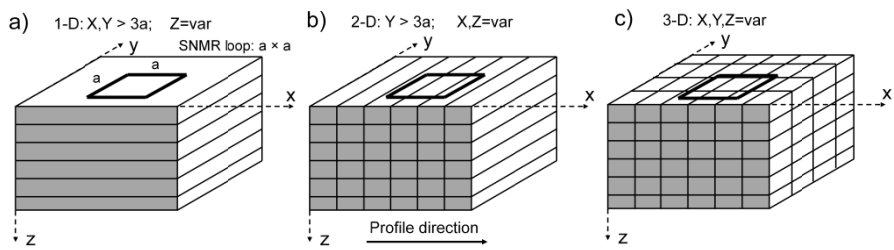

Figure 1.13. *Visualization of SNMR results: a) 1-D survey: the water content and relaxation times are represented as infinite horizontal layers; b) 2-D survey: the water content and relaxation times are represented as parallelepipeds, infinite in the transversal to the profile direction; c) 3-D survey: the water content and relaxation times are represented as cells smaller than the loop size*

Resolution of the inversion is limited by the properties of the linear equation used for inversion, but also depends on the survey design and the signal-to-noise ratio. In general, SNMR is a low-resolution method, and water-saturated structures can be resolved with the uncertainty of a few meters to a few tens of meters. This will be discussed in more detail in Chapter 4.

Aquifer hydrodynamic properties. Porosity and hydraulic conductivity are the basic parameters that characterize the productivity of an aquifer formation [LAC 05]. Actually, existing SNMR instruments allow the investigation of only hydraulically permeable rocks. For example, clay may contain a lot of water but, being a low permeable material, is seen with SNMR as a dry rock. The water content w derived from SNMR inversion allows the estimation of the effective porosity $n_e \approx w$ and an empirical relationship $k = C_p w T_1^2$ allows the prediction of the hydraulic conductivity k. C_p is an empirical constant that needs to be calibrated. w and T_1 are the water content and the relaxation time derived from SNMR inversion. In some rocks, T_1 can be replaced by T_2 or T_2^*. The transmissivity $T = k\Delta z$ is a product of the hydraulic conductivity k and the aquifer thickness Δz both estimated with SNMR. T is a more robust parameter than k and Δz separately.

Finally, for positioning SNMR in the geophysical toolbox let us compare SNMR with other popular surface geophysical methods.

Method	***Measured parameter***	***Rock property***	***Information about subsurface***
Electric and/or electromagnetic	Electrical resistivity	Electrical properties of rocks	Subsurface formations of different electrical resistivity
Seismic	Velocity of propagation of seismic waves	Elastic properties of rocks	Structural geological information
SNMR	Magnetic resonance response of groundwater	Water saturation	Rock hydraulic properties

Table 1.1. *Comparison of SNMR with electric/electromagnetic and seismic methods*

For example, Table 1.1 shows that electric and EM methods provide distribution of the electrical resistivity in the subsurface, and seismic methods provide elastic properties of rocks. These physical parameters of the rock have indirect and often non-unique information about groundwater and hydrodynamic properties of water-saturated formations. On the contrary, the SNMR signal is directly linked with groundwater which allows more reliable interpretation of SNMR results in terms of groundwater.

2

The Basics of NMR

2.1. NMR phenomenon

2.1.1. *Precession of free spins*

The phenomenon of Nuclear Magnetic Resonance (NMR) could be observed by studying nuclei which possess both a magnetic moment and angular momentum. The hydrogen nucleus, a proton, has a spin angular momentum $\mathbf{J}$ and an associated magnetic moment μ. Since they are parallel to each other, we can write

$$\mu = \gamma \mathbf{J} \ , \qquad [2.1]$$

with γ being the gyromagnetic ratio. It is a constant, which has different values for different nuclei. For protons $\gamma_p / 2\pi = 4.257707 \times 10^7$ Hz/Tesla.

When a proton is placed in an external magnetic field $\mathbf{B}$, the magnetic field will produce a torque on the magnetic moment of amount $\mu \times \mathbf{B}$. Hydrogen nuclei also possess an angular momentum and hence the nucleus acts as a gyroscope and precesses about the external magnetic field. The equation of motion for this precession is

$$\frac{d\mathbf{J}}{dt} = \mu \times \mathbf{B} \ . \qquad [2.2]$$

Since $\mu = \gamma \mathbf{J}$, we obtain

$$\frac{d\mu}{dt} = \mu \times (\gamma \mathbf{B}) \ . \qquad [2.3]$$

Assuming a laboratory reference frame with the axes (x, y, z) with the corresponding unit vectors $(\mathbf{i}, \mathbf{j}, \mathbf{k})$ and that the magnetic field $\mathbf{B}$ is applied along the z-axis, precession of the magnetic moment is shown in Figure 2.1.

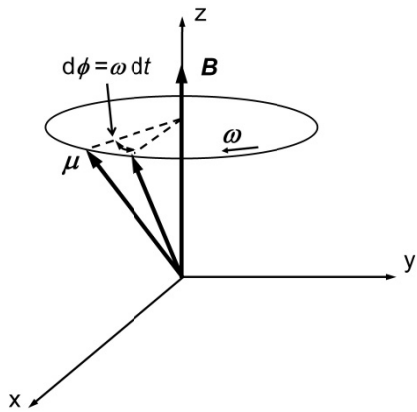

Figure 2.1. *Precession of the magnetic moment about an external magnetic field*

A spin's magnetic moment μ is precessing about the applied magnetic field $\mathbf{B}$ with the Larmor frequency

$$f = \omega / 2\pi = \gamma B / 2\pi \ . \qquad [2.4]$$

The Larmor frequency is the resonance frequency of the magnetic nuclei. As the gyromagnetic ratio γ is a constant, which has different values for different nuclei, the Larmor frequency is also a property of the nuclei. Magnetic nuclei can absorb or emit energy only at their Larmor frequency.

2.1.2. *Macroscopic spin magnetization*

When there is no external magnetic field $\mathbf{B}$, the proton spins are randomly oriented, resulting in zero macroscopic magnetization. When $\mathbf{B}$ is applied, the macroscopic magnetization gradually builds an equilibrium value M_0. Whilst the dynamics of a single spin needs a quantum mechanical explanation, the description of the behavior of the macroscopic spin magnetization can be given using classical physics [ABR 61]. The classical treatment is an approximation, but in many cases, it allows simplifying the treatment of the NMR phenomenon with sufficient accuracy.

We assume that in the investigated area, the equilibrium spin magnetization for protons per unit volume M_0 is constant and that $M = |\mathbf{M}| = M_0 dV$. M_0 is described by the Curie equation

$$M_0 = \mathrm{N}B\frac{\gamma^2\hbar^2}{4k\mathrm{T}}, \qquad [2.5]$$

where N is the number of protons per unit volume, T is the absolute temperature, $\hbar$ is the Planck constant and the Boltzmann constant $k = 1.3805 \cdot 10^{-23}$ [J/°]. Since $\mathrm{N} = 6.692 \cdot 10^{28}$ [/m^3] then $M_0 = 3.287 \cdot 10^{-3} B_0$ at 293K (20°C).

Using the classical model, the NMR phenomenon can be described by a set of equations proposed in 1946 by Felix Bloch [BLO 46]. The Bloch equations have provided, for liquid samples at least, in most cases a correct quantitative description of the behavior of the magnetic resonance phenomenon.

In an arbitrary homogeneous magnetic field $\mathbf{B}$, the equation of motion of the macroscopic spin magnetization $\mathbf{M}$ is

$$\frac{d\mathbf{M}}{dt} = \gamma(\mathbf{M} \times \mathbf{B}). \qquad [2.6]$$

Assuming that the applied magnetic field is the sum of a static field $\mathbf{B}_0$ and a much smaller radio frequency field $\mathbf{B}_1$, in the laboratory frame the Bloch equations can be written as

$$\frac{dM_z}{dt} = \gamma(\mathbf{M} \times \mathbf{B})_z + \frac{M_0 - M_z}{T_1},$$

$$\frac{dM_x}{dt} = \gamma(\mathbf{M} \times \mathbf{B})_x + \frac{M_x}{T_2}, \qquad [2.7]$$

$$\frac{dM_y}{dt} = \gamma(\mathbf{M} \times \mathbf{B})_y + \frac{M_y}{T_2},$$

where $\mathbf{B} = \mathbf{B}_0 + \mathbf{B}_1$; T_1 is called the longitudinal, or spin-lattice relaxation time; and T_2 the transverse, or spin-spin relaxation time. In the laboratory frame the vector $\mathbf{M}$ is rotating about the static field $\mathbf{B}_0$ with the Larmor frequency $\omega_0 = -\gamma \mathbf{B}_0$ (clockwise). A linearly polarized, oscillating magnetic field applied in the x-direction $\mathbf{B}_x = 2B_1 \cos(\omega t)$ can be presented as two rotating components with the angular frequency $+\omega$ and $-\omega$. Only co-rotating with the spin system part (clockwise) with the amplitude B_1 has an effect on the spin magnetization. The field $\mathbf{B}_1$ will be the co-rotating component of the applied oscillating field. The effect of the counter-rotating component is usually neglected.

In a reference frame, rotating around $\mathbf{B}_0$ with the angular frequency ω there is an effective static field

$$\mathbf{B}_{\mathbf{eff}} = \mathbf{i}B_1 + \mathbf{k}(B_0 - \omega/\gamma), \qquad [2.8]$$

where ω/γ component called the fictitious field.

In the rotating frame the Bloch equations can be rewritten as

$$\frac{dM_z}{dt} = \gamma(\mathbf{M} \times \mathbf{B}_{eff})_z + \frac{M_0 - M_z}{T_1},$$

$$\frac{dM_x}{dt} = \gamma(\mathbf{M} \times \mathbf{B}_{eff})_x + \frac{M_x}{T_2}, \qquad [2.9]$$

$$\frac{dM_y}{dt} = \gamma(\mathbf{M} \times \mathbf{B}_{eff})_y + \frac{M_y}{T_2}.$$

At the exact resonance ($\omega = \omega_0$) the fictitious field cancels the static field $\mathbf{B}_0$ and considering equations [2.4] we can write $B_0 - \omega/\gamma = 0$. Then, from equation [2.8] it follows that

$$\mathbf{B}_{\mathbf{eff}} = \mathbf{i}B_1, \qquad [2.10]$$

thus simplifying the Bloch equations to

$$\frac{dM_z}{dt} = \gamma(\mathbf{M} \times \mathbf{B}_1)_z + \frac{M_0 - M_z}{T_1},$$

$$\frac{dM_x}{dt} = \gamma(\mathbf{M} \times \mathbf{B}_1)_x + \frac{M_x}{T_2}, \qquad [2.11]$$

$$\frac{dM_y}{dt} = \gamma(\mathbf{M} \times \mathbf{B}_1)_y + \frac{M_y}{T_2}.$$

In the equilibrium, $\mathbf{M}$ is oriented along the external magnetic field $\mathbf{B}_0$ and the angle θ between the spin magnetization and the geomagnetic field is equal to zero as shown in Figure 2.2a.

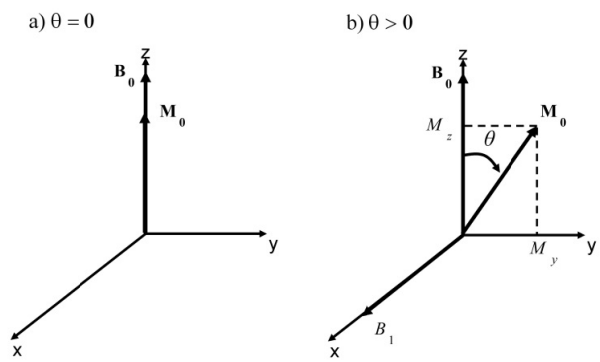

Figure 2.2. *Rotation of the spin magnetization under exact resonance ($\Delta\omega = 0$):*

a) equilibrium position; b) when a magnetic field $\mathbf{B}_1$ is applied

At the exact resonance, when we apply a magnetic field $\mathbf{B}_1$ along the x-axis with a carrier frequency equal to the Larmor frequency it causes the magnetization $\mathbf{M}$ to rotate about $\mathbf{B}_1$ in the z, y plane with the angular frequency $\omega_1 = \gamma B_1$. At time t, the three components of the spin magnetization are

$$M_x = 0,$$
$$M_y = \sin(\theta) M_0, \qquad [2.12]$$
$$M_z = \cos(\theta) M_0,$$

where the angle $\theta = \omega_1 t = \gamma B_1 t$ is called the flip angle. The rotation of the magnetization is sketched in Figure 2.2b.

When the resonance conditions are not respected ($\omega \neq \omega_0$), the motion of spins in the rotating frame follows a precession cone around the effective field (Figure 2.3). The angular frequency of the precession ($\omega_{eff}^2 = \omega_1^2 + \Delta\omega^2$) depends on the frequency offset ($\Delta\omega = \omega_0 - \omega$) between the Larmor frequency ($\omega_0 = \gamma B_0$), the rotating frame frequency (ω) and the applied magnetic field frequency ($\omega_1 = \gamma B_1$).

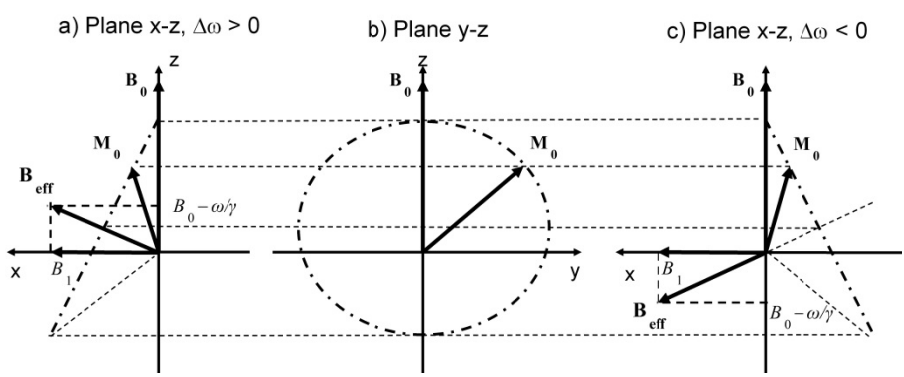

Figure 2.3. *Rotation of the spin magnetization under off-resonance conditions: a) case Δω> 0; b) common case for any sign of Δω; c) case Δω< 0*

The total precessional angle is given by $\theta(t) = \omega_{eff} t = \gamma B_{eff} t$. At time $t = \tau$, the spin magnetization will, in general, have three components, which are [MAN 79]

$$M_x = \frac{\omega_1 \Delta\omega}{\omega_{eff}^2}\left(1 - \cos(\omega_{eff}\tau)\right) M_0,$$

$$M_y = \frac{\omega_1}{\omega_{eff}} \sin(\omega_{eff}\tau) M_0, \qquad [2.13]$$

$$M_z = \frac{\Delta\omega^2 + \omega_1^2 \cos(\omega_{eff}\tau)}{\omega_{eff}^2} M_0.$$

The magnetic resonance signal depends on the component of the nuclear magnetization perpendicular to the static magnetic field (*x,y* plane). The $M_y = \mathrm{Re}(M_\perp)$ component corresponds to the real part of the NMR signal and $M_x = \mathrm{Im}(M_\perp)$ - to the imaginary part. The position of the magnetization vector $\mathbf{M_0}$ and its projection $M_\perp$ after a magnetic field $\mathbf{B}_1$ being applied during time τ $(\theta = \omega_{eff}\tau)$ is shown in Figure 2.4. When $\Delta\omega = 0$, the M_x component is equal to zero and hence the signal, which is thus proportional only to M_y has no phase shift (Figure 2.4b). If $\Delta\omega \neq 0$, then the signal will be a vector in the complex plane. The phase shift depends on the sign and magnitude of the frequency offset. It is illustrated in Figure 2.4a for a positive frequency offset and in Figure 2.4c for a negative one. Obviously, the magnitude of the total spin magnetization is constant $M_0^2 = M_x^2 + M_y^2 + M_z^2$.

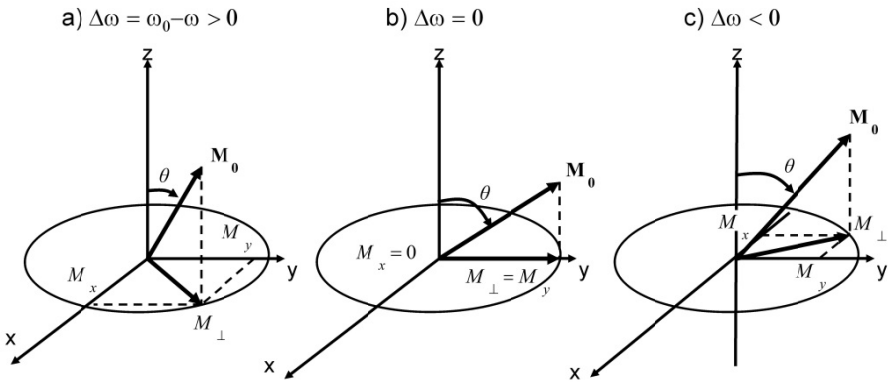

Figure 2.4. *Precession of the spin magnetization in the tilted rotating reference frame considering different frequency offsets Δω*

For demonstration purposes the proportionality between magnitudes of the magnetization under the resonance and off-resonance conditions is not respected. In fact, whilst spins, which are at the exact resonance, will respond strongly, those far from the resonance will be only slightly perturbed at their equilibrium position.

2.2. NMR relaxation

2.2.1. *Longitudinal relaxation*

At thermal equilibrium, nuclei are distributed among the energy levels according to a Boltzmann distribution. After this equilibrium distribution is disrupted (by changing the static magnetic field or irradiating samples by an oscillating magnetic field), the nuclear spin system returns to equilibrium with its surroundings by a relaxation process characterized by a time $\mathbf{T}_1$, called the spin-lattice or longitudinal relaxation time. In Bloch equations [2.7] the change of $\mathbf{M}_z$ with time is described as

$$\frac{dM_z}{dt} = \gamma(\mathbf{M}\times\mathbf{B}_1)_z + \frac{M_0 - M_z}{T_1}, \qquad [2.14]$$

$$M_z = M_0(1 - e^{-t/T_1}).$$

T_1 reflects efficiency of the exchange of the magnetic energy between the spin system and its surroundings. When the coupling between the spin system and the environment is weak T_1 will be large, but strong coupling will render T_1 small.

In order to illustrate the effect of the longitudinal relaxation T_1 on the spin magnetization $\mathbf{M}$ after application of a pulse of a magnetic field $\mathbf{B}_1$, let us assume that all the magnetic moments keep the same precessing frequency and phase coherence. Immediately after the pulse is terminated, $\mathbf{M}$, which was oriented along the static field $\mathbf{B}_0$, is turned away at the angle θ (Figure 2.5a). Then, the spin system approaches equilibrium with the time constant T_1 and the spin magnetization $\mathbf{M}$ is correspondingly decreasing. It would be erroneous to present the spin-lattice relaxation as a rotation of the vector $\mathbf{M}$, in the z, y plane, back to equilibrium along $\mathbf{B}_0$. The non-equilibrium magnetization $\mathbf{M}$ is simply disappearing without changing the angle θ.

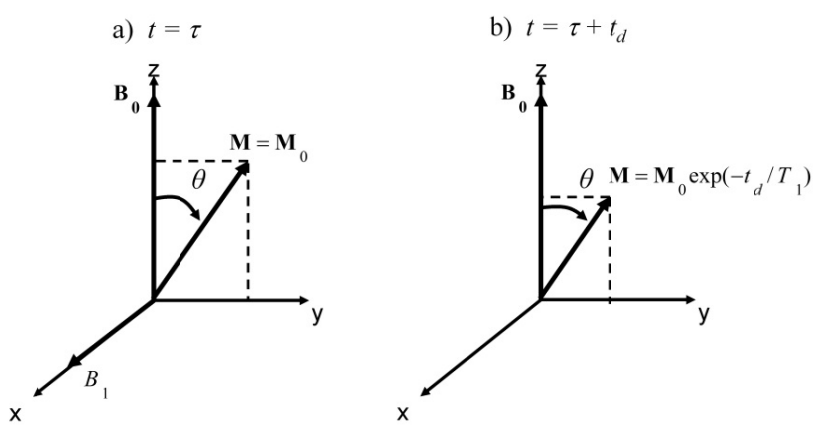

Figure 2.5. *The spin magnetization after application of a pulse of a magnetic field* B_1 *(duration* τ*): a) immediately after the pulse is terminated; b) effect of the longitudinal relaxation on the spin magnetization after a time interval* t_d

2.2.2. *Transverse relaxation*

The macroscopic spin magnetization $\mathbf{M}$ is a vector composed of the sum of magnetic moments of individual spins that also are vectors $\mathbf{M} = \sum_i \boldsymbol{\mu}_\mathbf{i}$. Since there is originally no phase coherence of the magnetic moments of spins, they are randomly oriented and consequently a projection of the macroscopic spin magnetization onto x, y plane is equal to zero ($M_\perp = 0$). However, after a magnetic field $\mathbf{B}_1$ is applied, the moments $\boldsymbol{\mu}_\mathbf{i}$ will have the same phase and lie in such an orientation that a non-zero component of $\mathbf{M}$ is generated in the x, y plane ($M_\perp > 0$) as shown in Figure 2.6a. Because of the natural processes that cause nuclei to exchange energy with each other and with the environment, the moments $\boldsymbol{\mu}_\mathbf{i}$ lose the phase coherence after each interaction and begin to spread across the x, y plane as shown in Figure 2.6b, which causes $M_\perp$ to diminish with the time constant T_2, called the spin-spin or transversal relaxation time.

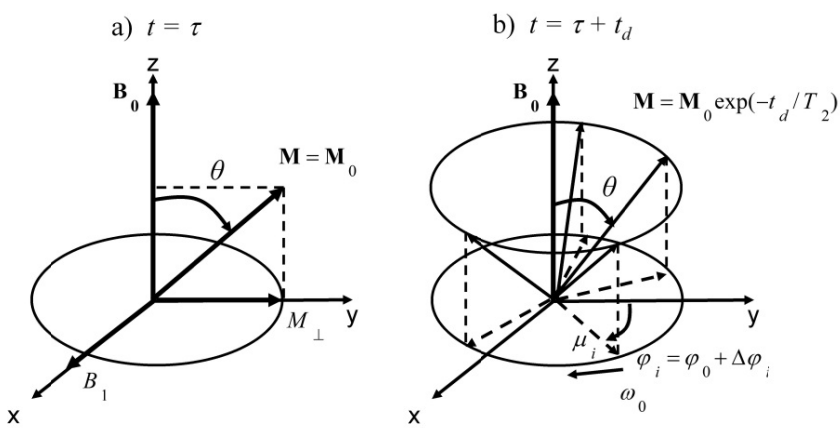

Figure 2.6. *The spin magnetization after application of a pulse of a magnetic field B_1 (duration τ): a) immediately after the pulse is terminated; b) effect of the transverse relaxation with the time constant T_2 on the spin magnetization after a time interval t_d*

In Bloch equations [2.7] the decay of $M_\perp$ is described as

$$\frac{dM_x}{dt} = -\frac{M_x}{T_2}, \qquad \frac{dM_y}{dt} = -\frac{M_y}{T_2},$$
$$M_\perp = M_0(1 - e^{-t/T_2}). \qquad [2.15]$$

Note that when the transverse component of the spin magnetization becomes zero ($M_\perp \to 0$) the NMR signal cannot be measured, but the spin system may still be at non-equilibrium with the environment so that the limitation $T_2 \le T_1$ is always respected. This is a fundamental difference between the transversal and longitudinal relaxations.

Since the static magnetic field may not be perfectly homogeneous, nuclei in different portions of the sample experience slightly different values $\mathbf{B}_0$. Hence they precess at slightly different frequencies, some faster than the rotating frame, some slower ($\omega_i = \omega_0 + \Delta\omega_i$). This process also causes the moments $\boldsymbol{\mu}_\mathbf{i}$ to lose the phase coherence (Figure 2.7) and consequently $M_\perp$ will diminish with the rate characterized by the time constant T_2^*.

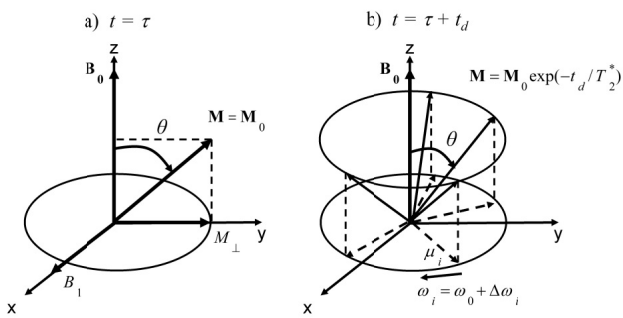

Figure 2.7. *The spin magnetization after application of a pulse of a magnetic field* B_1 *(duration* τ*): a) immediately after the pulse is terminated; b) effect of the transverse relaxation with the time constant* T_2^* *on the spin magnetization after a time interval* t_d

Considering both the longitudinal and transverse relaxations, T_2^* can be approximated as [FUK81]

$$\frac{1}{T_2^*} \cong \frac{1}{2T_1} + \frac{1}{T_2} + \gamma \Delta B_0, \qquad [2.16]$$

where ΔB_0 characterizes inhomogeneity of the static magnetic field B_0 and γ is the gyromagnetic ratio. T_2^* is the shortest relaxation time and $T_2^* \leq T_2 \leq T_1$. Often, the effect of the longitudinal relaxation on T_2^* may be neglected and T_2^* can be considered as

$$\frac{1}{T_2^*} \cong \frac{1}{T_2} + \gamma \Delta B_0 . \qquad [2.17]$$

During the NMR experiment (usually <2 s) distribution of the static magnetic field B_0 within the investigated sample does not change. Consequently, the magnetic moments $\boldsymbol{\mu_i}$ are located in the same magnetic field, they have a constant Larmor frequency $\omega_{0i} = \omega_0 + \Delta\omega_i = const$ and dephasing is regular $\varphi_i = \varphi_0 + \Delta\omega_i t$ (Figure 2.7). Note that T_2 characterizes dephasing caused by a random energy exchange between spins and their environment what cause random dephasing $\phi_i = \phi_0 + \Delta\phi_i = random$ (Figure 2.6). It is a notable difference between T_2^* and T_2 that is used for measuring T_2 with the spin echo (SE) method.

2.2.3. *Diffusion in non-homogeneous magnetic field*

In the previous sections we assumed that nuclear spins do not change their position within the investigated sample. However, in liquids, spins can move by

diffusive motion of the atoms. Hence, if the static magnetic field B_0 is not homogeneous or a field gradient is imposed then such a movement will cause the magnetic moments $\boldsymbol{\mu}_i$ to change their Larmor frequency during one measuring cycle, thus introducing additional dephasing. Such a dephasing will accelerate relaxation of the NMR signal with the enhanced relaxation rate T_{2D}. In an infinite fluid medium, T_{2D} is given by the following expression [CAR 54]

$$\frac{1}{T_{2D}} = \gamma^2 G^2 D t^2 / 12 , \qquad [2.18]$$

where G is the spatial magnetic field gradient, D is the diffusion coefficient and t is the time during which diffusion will occur. Thus, the transverse relaxation rate enhanced by the effect of spin diffusion is given by

$$M_\perp = M_0 \exp\left(-t/T_2 - t/T_{2D} \right). \qquad [2.19]$$

The diffusion coefficient depends on temperature and it can be calculated for water using empirical function based on results reported by Sengers and Watson [SEN 86] (Figure 2.8).

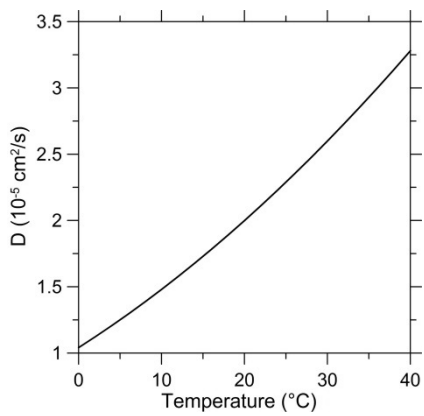

Figure 2.8. *Diffusion coefficient of water as a function of temperature*

Equation [2.18] is valid only for an infinite fluid medium and for water in rocks it is only approximately correct. However, assuming that most of the spins do not experience the presence of pore walls, we can use equation [2.18] to demonstrate the relationship between T_{2D} and a spatial magnetic field gradient G. In porous media, G may be imposed by magnetic particles that perturb the static magnetic field B_0. In this case, the distribution of the magnetic field gradient within the investigated sample may be non-uniform and T_{2D} can be calculated only approximately. Let us assume that G is a first order approximation of an equivalent inhomogeneity of the static magnetic field. Figure 2.9a shows estimated T_{2D} versus a magnetic field gradient considering three values of the diffusion time. Figure 2.9b presents dependence of the enhanced relaxation T_{2D} on the diffusion time for different values of the field gradient G.

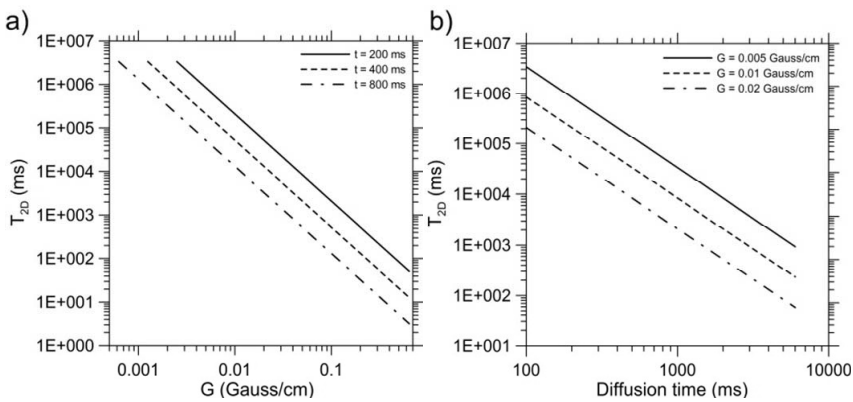

Figure 2.9. *The enhanced relaxation rate T_{2D} computed considering an inhomogeneous static magnetic field: a) T_{2D} versus the spatial magnetic field gradient G assuming the diffusion time t of 200, 400 and 800 ms; b) T_{2D} versus diffusion time and considering three values of the magnetic field gradient G*

When the distribution of the static magnetic field gradient G is unknown it can be roughly estimated assuming $T_2^* << T_2$ in equation [2.17] as

$$G \cong \Delta B_0 \cong \frac{1}{\gamma T_2^*}, \qquad [2.20]$$

where T_2^* is an experimental value and $\Delta B_0 \approx G$ is an estimate of a static magnetic field inhomogeneity. The relationship between G and T_2^* calculated using equation [2.20] is shown in Figure 2.10. Figures 2.9 and 2.10 allow qualitative estimation of the enhanced relaxation rate caused by diffusion of spins. For example, assuming $T_2^* = 7.5\ \text{ms}$, we obtain the corresponding value of the field gradient $G = 0.005$ Gauss/cm (Figure 2.10). Then, Figure 2.9b allows the estimation of T_{2D} for, e.g., the diffusion time of 2000 ms as $T_{2D} = 8500\ \text{ms}$.

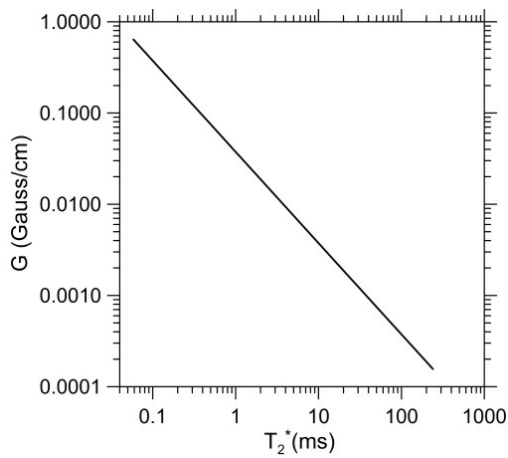

Figure 2.10. *Estimated dependence of the relaxation time constant T_2^* on the magnetic field gradient G*

Now, let us estimate the possible effect of T_{2D} on the transverse relaxation. In equation [2.19] the transverse relaxation term is given by

$$1/T_2 + 1/T_{2D} = 1/T_2(1 + 1/x), \qquad [2.21]$$

where $x = T_{2D}/T_2$. Figure 2.11 shows that for obtaining less than 10% error in the transverse relaxation term, T_{2D} must be ten times longer than T_2. This condition can be respected either for a short diffusion time or for small values of the field gradient (Figure 2.9b).

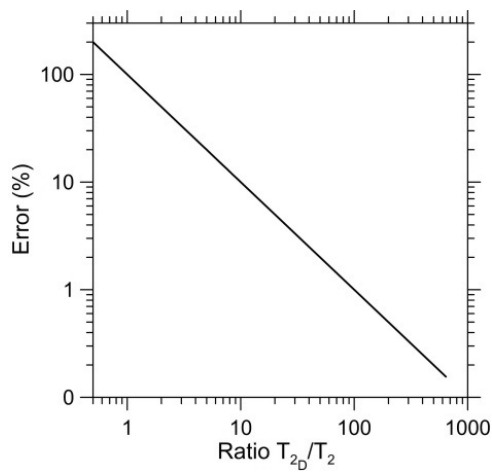

Figure 2.11. *The relative error in the transverse relaxation term caused by the enhanced relaxation versus T_{2D}/T_2 ratio*

The numerical example presented in Figure 2.12a shows relaxation of the nuclear magnetization (equation [2.19]) as a function of diffusion time. For computing, we assumed the following input: $D = 2\times10^{-5}$ cm^2/s, $T_2 = 400$ ms and $\gamma = 2.6752\times10^4$ rad×s^{-1}×Gauss^{-1}. The results demonstrate shortening of the relaxation caused by spin diffusion and when relaxation graphs were fitted by an exponential function we obtain estimates of the amplitude and time constant. Figure 2.12b shows the relative error of estimation in comparison with the known T_2 value. We can see that diffusion principally affects estimation of the relaxation time T_2 and the initial amplitude was estimated with a much smaller error.

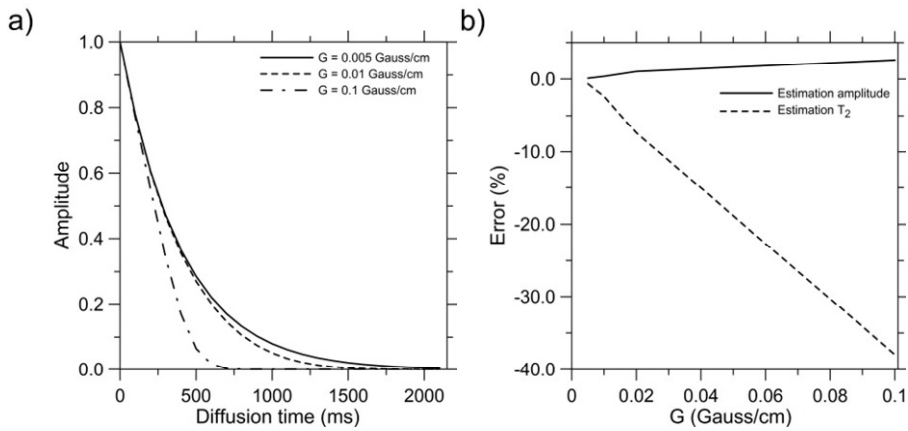

Figure 2.12. *Demonstration of the effect of a field gradient on the relaxation rate: a) transverse relaxation versus diffusion time in different field gradients; b) relative error of estimation of the amplitude and relaxation rate as a function of the field gradient*

Note that for rocks, the estimates presented above should be considered only as qualitative because the internal field gradients of porous media are induced by the magnetic susceptibility variations that depend not only on the magnitude of these variations, but also on the pore and grain geometries. Understanding of the effect of strong internal field gradients on NMR measurements is very important, but it is a very complex problem that is beyond the scope of this book. Numerous attempts of quantification of these effects have been reported [NEU 74; BEN 90; HÜR 98; ZHA 01; SUN 02; HÜR 02; FRE 06; POM 08; CHO 08; CHO 09; GRU 12], but it is recognized that quantification of the internal field gradients' distribution and analysis of experimental data remains very difficult.

2.3. NMR measurements

2.3.1. *Free induction decay (FID)*

For measuring the NMR signal, one or more coils are positioned around the investigated sample. A static magnetic field $\mathbf{B}_0$ is usually created by a special magnet but the Earth's magnetic field can also be used. The simplest NMR experiment consists of observing the free induction decay signal (FID). A pulse of alternating current energizes the induction coil thus creating a magnetic field $\mathbf{B}_1$ oscillating with the Larmor frequency $\omega_0 = \gamma B_0$ (Figure 2.13a). The pulse causes

rotation of the nuclear magnetization **M** around the x axis with the angular frequency $\omega_1 = \gamma B_1$. When the pulse is terminated **M** is turned at a flip angle $\theta = \omega_1 \tau_p$ and the transverse component of the nuclear magnetization $M_y = M_0 \sin(\theta)$ produces measurable NMR signal (FID). The shape of the signal envelope depends on the distribution of internal magnetic field gradients and may have exponential or Gaussian shape [SUK 01; GRU 11] as shown in Figure 2.13b. Oscillating with the Larmor frequency ω_0, the FID signal decays with the time constant T_2^*. For the exponential envelope

$$e(t) = e_0 \exp(-t/T_2^*) \cos(\omega_0 t + \varphi_0), \qquad [2.22]$$

where e_0 and φ_0 are the initial amplitude and initial phase respectively. For the Gaussian envelope it may be approximated as

$$e(t) = e_0 \exp\left(-0.5(t/T_2^*)^2\right) \cos(\omega_0 t + \varphi_0). \qquad [2.23]$$

In both cases the initial amplitude e_0 and relaxation time T_2^* can be obtained directly from the FID signal.

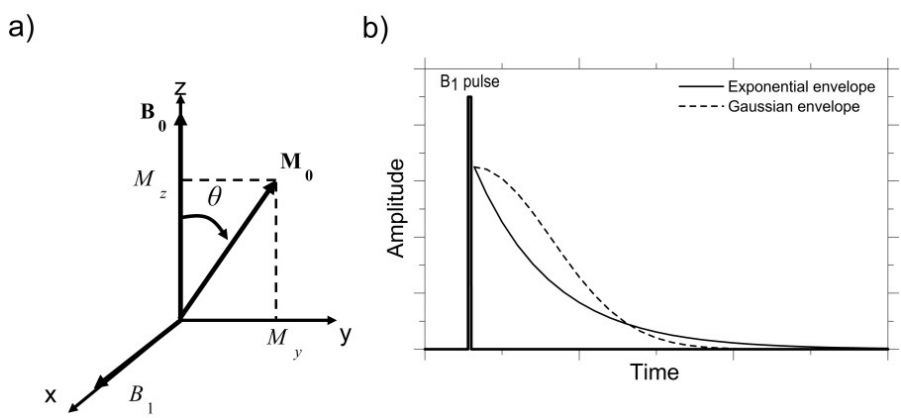

Figure 2.13. *Schematic presentation of the FID measuring procedure: a) nuclear magnetization excitation pulse being applied; b) corresponding FID signal proportional to the M_y component is drawn considering exponential and Gaussian envelopes*

The FID signal is also used for measuring the relaxation time T_1. The most popular methods are called the inversion recovery and the saturation recovery. Both methods are based on measuring the FID signal generated only by the equilibrium component of nuclear magnetization, separated from the excited component by applying different pulse sequences.

The inversion recovery measuring scheme is presented in Figure 2.14. In equilibrium, the nuclear magnetization $\mathbf{M}$ vector is oriented along the static magnetic field $\mathbf{B}_0$ (Figure 2.14a). The first pulse turns $\mathbf{M}$ at the flip angle $\theta = 180°$ (Figure 2.14b). The nuclear magnetization $\mathbf{M}$ is fully excited, but its transversal component $M_\perp$ is zero and hence no signal can be measured (FID1=0). Then, $\mathbf{M}$ starts decreasing with the time constant T_1 (Figure 2.14c) and an equilibrium component $|M_0 - M|$ increases. After a time delay τ_d the second pulse is applied.

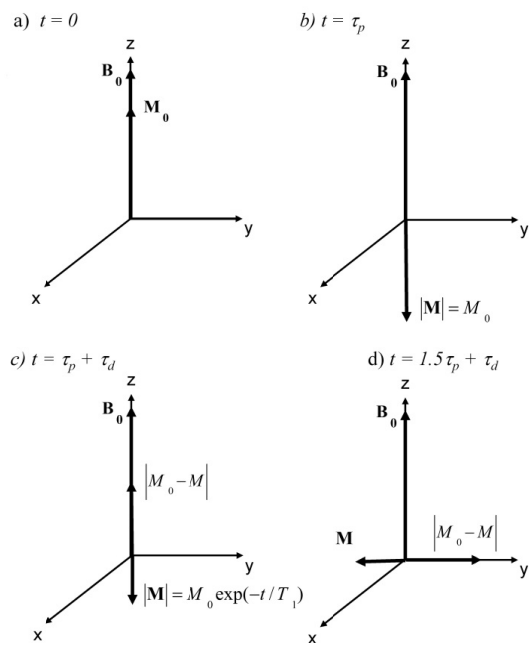

Figure 2.14. *Evolution of the nuclear magnetization* ***M*** *corresponding to the inversion recovery measuring scheme: a) equilibrium position; b) a 180° pulse of duration* τ_p *turns* ***M*** *in the –z direction; c) relaxation of* ***M*** *with the time constant* T_1 *during time interval* τ_d*; d) a 90° pulse (duration* τ_p */2) turns* ***M*** *in the –y direction and a relaxed component of the nuclear magnetization* $|M_0\text{-}M|$ *is turned along the +y axis*

The pulse has a value twice as small as the product $\omega_1 \tau_p$, and consequently it turns nuclear magnetization at the flip angle $\theta = 90°$. This pulse sequence is called 180°,90° sequence. After the second pulse is terminated, the non-relaxed (excited) component $\mathbf{M}$ is oriented in the $-y$ direction and the already-relaxed component (equilibrium) $\left|M_0 - M\right|$ turns in the $+y$ direction (Figure 2.14d). The measured NMR signal (FID2) is proportional to the difference between the excited and relaxed components of the nuclear magnetization. T_1 can be estimated by varying delay between the pulses τ_d and measuring the corresponding FID2 signal. A typical measuring procedure is shown in Figure 2.15.

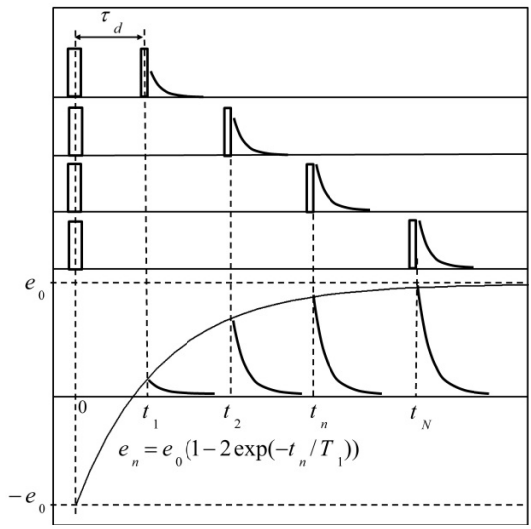

Figure 2.15. *A typical sequence of inversion recovery for measuring T_1*

For each value of τ_d position of the pulses, the signal is plotted against time. The FID2 amplitude plotted against delay τ_d (bottom graph) allow the estimation of T_1 using the following equation

$$e(\tau_d) = e_0\left(1 - 2\exp(-\tau_d / T_1)\right). \qquad [2.24]$$

The saturation recovery measuring scheme is illustrated in Figure 2.16. For this method the 90°,90° sequence is used. After the first pulse, **M** is turned in the +*y* direction and the FID1 signal corresponding to the initial amplitude e_0 can be measured (Figure 2.16b). The second pulse is applied after a delay τ_d. It turns the non-relaxed component **M** along the –*z* axis which allows us to measure the FID2 signal that is proportional only to the relaxed component $|M_0 - M|$ (Figure 2.16d).

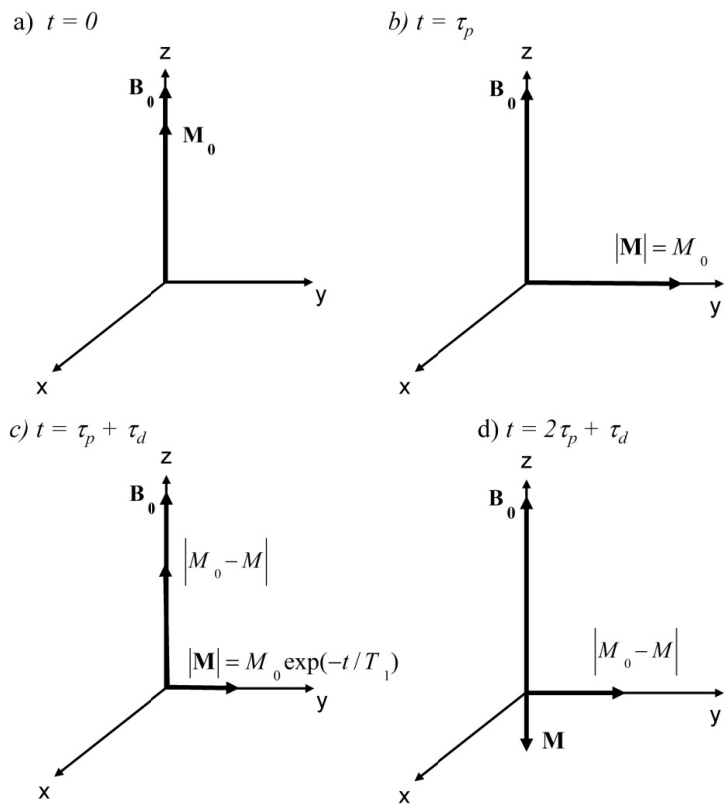

Figure 2.16. *Evolution of the nuclear magnetization **M** corresponding to the saturation recovery measuring scheme: a) equilibrium position; b) a 90° pulse of duration τ_p turns **M** in the +y direction; c) relaxation of **M** with the time constant T_1 during time interval τ_d; d) a 90° pulse (duration τ_p) turns **M** in the –z direction and a relaxed component of the nuclear magnetization $|M_0$-$M|$ is turned along the +y axis*

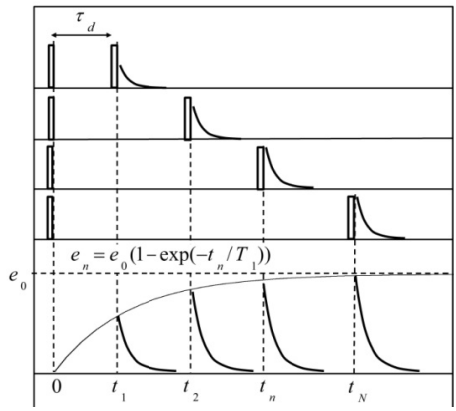

Figure 2.17. *A typical sequence of saturation recovery for measuring T_1*

T_1 can be estimated by measuring the FID2 signal for different values of the delay τ_d. A typical measuring procedure is shown in Figure 2.17. The FID2 amplitude plotted against a time delay τ_d (bottom graph) allows us to estimate T_1 as

$$e(\tau_d) = e_0\left(1-\exp(-\tau_d/T_1)\right). \qquad [2.25]$$

The saturation recovery method can be modified for applications when the magnetic field $\mathbf{B}_1$ within the investigated volume is non-uniform, which is the common case for the surface NMR. A non-uniform $\mathbf{B}_1$ renders it impossible to obtain the same flip angle for different portions of the sample and hence, measuring procedures based on the specific flip angles (90° or 180°) may produce errors in the results.

The modified saturation recovery scheme is presented in Figure 2.18. Measurements are carried out using a θ,-θ sequence. The flip angle θ may have any value, but it is preferred that both pulses be identical. The second pulse has to be inverted. The pulses produce the same flip angle and hence $\theta_1 = -\theta_2$ in any part of the sample. After the first pulse, $\mathbf{M}$ is turned through the angle θ, which can be different for different portions of the sample (Figure 2.18b). During a delay τ_d,

relaxation occurs and then the second pulse is applied. The pulse produces the flip angle $-\theta$ and thus, the non-relaxed component of the nuclear magnetizationin the entire sample is oriented along the $+z$ axis and does not produce an NMR signal. Only the relaxed component produces the FID2 signal that is measured for different values of the delay τ_d.

A typical measuring procedure is shown in Figure 2.19. The FID2 amplitude plotted against a time delay τ_d (bottom graph) allows the estimation of T_1 from the equation

$$e(\tau_d) = -e_0\left(1-(1-x_{\tau 0})\exp(-\tau_d/T_1)\right), \qquad [2.26]$$

where $x_{\tau 0} = e_{\tau 0}/e_0$ is due to possible differences between the pulses and $e_{\tau 0}$ is the FID2 signal measured when $\left(\tau_d/T_1\right) \to 0$.

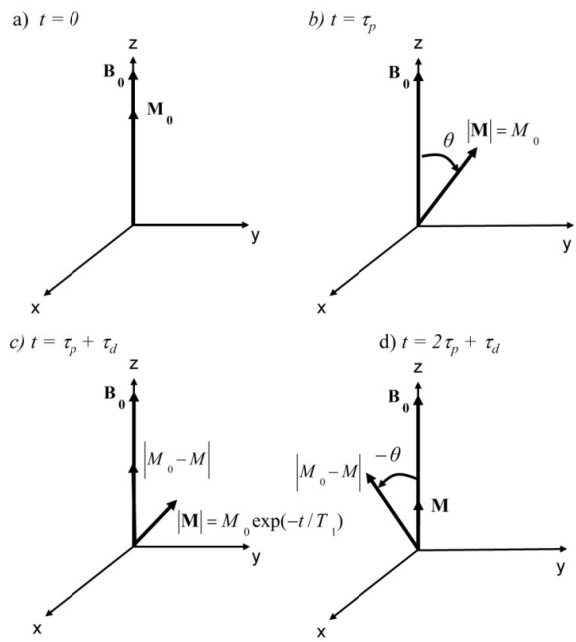

Figure 2.18. *Evolution of the nuclear magnetization **M** corresponding to the modified saturation recovery measuring scheme: a) equilibrium position; b) the first pulse of duration τ_p turns **M** in the z-y plane at a flip angle $+\theta$; c) relaxation of **M** with the time constant T_1 during a time interval τ_d; d) the second pulse (duration τ_p but of inverse polarity) turns **M** in the +z direction and a relaxed component of the nuclear magnetization $|M_0-M|$ is turned at a flip angle $-\theta$*

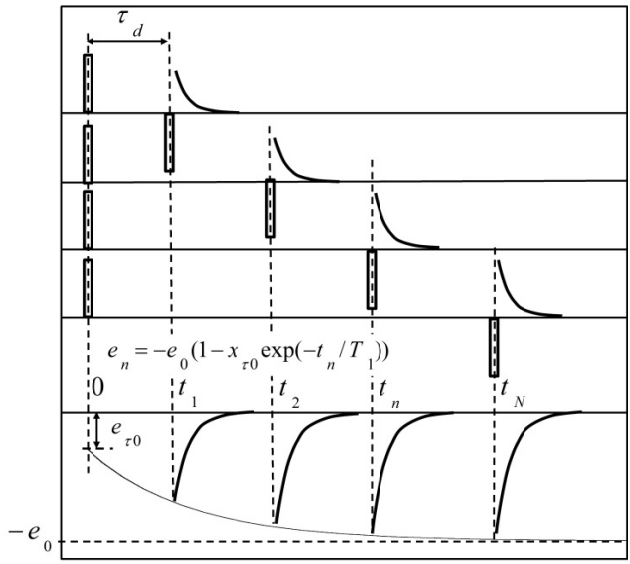

Figure 2.19. *A typical sequence of modified saturation recovery for measuring T_1*

2.3.2. *Spin echo (SE)*

The SE technique was developed by Hahn for NMR measurements in a heterogeneous static magnetic field $\mathbf{B}_0$ [HAH 50]. For observing an SE signal it is necessary to respect the following condition

$$T_2^* \ll T_2 < T_1 . \qquad [2.27]$$

An SE can be observed with different pulse sequences. For example, Hahn used a 90°,90° sequence. However, a 90°,180° sequence is often preferred because it allows us to obtain the maximum amplitude of the SE signal.

Figure 2.20 schematically shows the formation of an SE considering a 90°,180° sequence. The first 90° pulse sets the nuclear magnetization $\mathbf{M}$ in the $+y$ direction (Figures 2.20b, 2.16b) and the FID1 signal can be observed. In a reference frame rotating clockwise with the Larmor frequency ω_0 some magnetic moments $\boldsymbol{\mu}_\mathbf{i}$ are faster than the rotating frame and hence they rotate clockwise with a relative angular

frequency $+\Delta\omega_i$. Some other magnetic moments are slower and rotate counterclockwise with a relative angular frequency $-\Delta\omega_i$. The local difference in the Larmor frequency causes dephasing of the nuclear magnetization with the time constant T_2^*. Dephasing during the time τ_d (Figure 2.20c) causes the FID1 signal to decrease. As $T_2^* \ll T_1$, **M** remains excited even when FID1 becomes zero, but relaxation with the time constant T_1 also takes place and an equilibrium component $\left|M_0 - M\right|$ grows (Figure 2.16c). The second pulse performs two actions. It sets the non-relaxed component **M** along the –*y* axis as shown in Figure 2.20d and sets the relaxed component $\left|M_0 - M\right|$ at the –*z* direction. In both cases the FID2 signal is absent because **M** is oriented along the –*y* axis, remains dephased and the transversal component of $\left|M_0 - M\right|$ is zero. However, if a sequence other than 90°, 180° is used or the second pulse is not perfect and produces an angle other than the 180° flip angle, then the FID2 signal will appear. After the second pulse, magnetic moments $\boldsymbol{\mu}_\mathbf{i}$ that are faster ($+\Delta\omega_i$) are set behind the rotating frame but continue rotating clockwise, and those that are slower ($-\Delta\omega_i$) are set before the rotating frame and rotate counterclockwise. At time τ_d after the second pulse, the dephased components of **M** will meet again along the –*y* axis thus producing the refocusing effect (Figure 2.20e). The transverse relaxation with the time constant T_2 cause random dephasing and some $\boldsymbol{\mu}_\mathbf{i}$ will not refocus, which attenuates SE amplitude.

The SE measuring scheme (Figure 2.21) consists of transmitting two consecutive pulses separated by a time interval τ_d. The SE signal can be observed at time τ_d after the second pulse is terminated. The SE signal is composed of two FID signals corresponding to the refocusing and following dephasing of the nuclear magnetization as shown in Figure 2.21. The FID signal can also be observed.

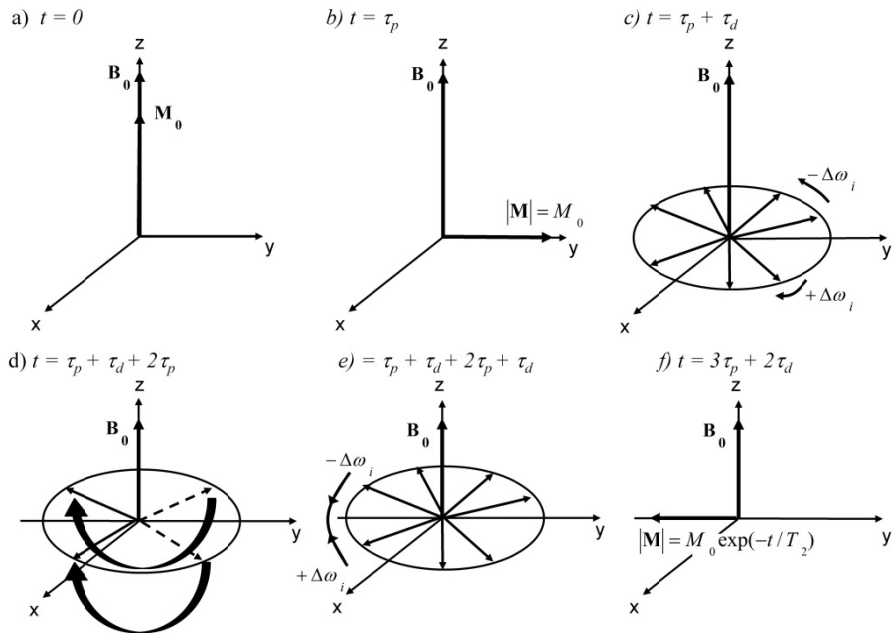

Figure 2.20. *Graphical illustration of the formation of an SE signal: a) equilibrium position; b) the macroscopic spin magnetization* ***M*** *is turned at the flip angle* θ*=90°, by a pulse of duration* τ_p *; c) dephasing of the macroscopic magnetization in the x-y plain; d)* ***M*** *is turned through the flip angle* θ*=180° by a refocusing pulse applied at time* τ_d *after the first pulse; e) refocusing of the macroscopic magnetization during a time interval* τ_d*; f) refocused macroscopic spin magnetization* ***M*** *attenuated by the transversal relaxation*

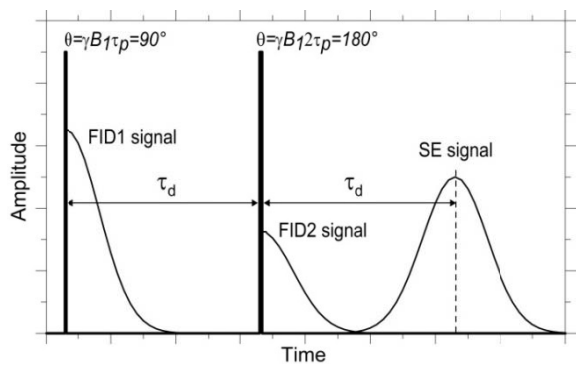

Figure 2.21. *A schematic presentation of the SE measuring procedure consisting of injection of two pulses separated by a time interval* τ_d*. The FID1 and FID2 signals can be observed immediately after the corresponding pulse. The SE signal can be measured at time* τ_d *after the refocusing pulse*

Formation of an SE is a phenomenon that depends on internal magnetic field gradients and the shape of the signal may be complex. In a simple case, an SE envelope can be considered as Gaussian as is given by [HAH 50]

$$e_{SE}(t) = e_{2\tau_d} \exp\left(-\frac{(t-2\tau_d)^2}{2(T_2^*)^2}\right). \qquad [2.28]$$

For practical use it is convenient to present it as

$$e_{SE}(t) = e_{2\tau_d} \exp\left(-\frac{(t-2\tau_d)^2}{0.36\Delta t_{0.5}^2}\right), \qquad [2.29]$$

where $\Delta t_{0.5}$ is the half-width of the echo signal (the width of the echo envelope at the level of one half of the maximum echo amplitude). Thus the relaxation time T_2^* can be easily estimated as $T_2^* \approx 0.424 \times \Delta t_{0.5}$.

For calculating the SE amplitude we assume the mathematical and geometrical interpretations presented in Hahn's paper [HAH 50]. Under near-resonance conditions, for pulses of equal intensity B_1 and neglecting the relaxation and molecular diffusion, $M_\perp$ can be calculated as [BLO 55]

$$M_\perp = -M_0 \sin\left(\theta_1\right) \times \sin^2\left(0.5\theta_2\right), \qquad [2.30]$$

where $\theta_1 = \gamma B_1 \tau_{p1}$ and $\theta_2 = \gamma B_1 \tau_{p2}$ are the flip angles for corresponding pulses. If a 90°,180° pulse sequence is used then $\theta_2 = 2\theta_1 = \theta$ and consequently the SE amplitude can be calculated as

$$M_\perp = -M_0 \sin^3(\theta). \qquad [2.31]$$

Note, that after equation [2.30], the SE signal calculated using equation [2.31] is insensitive to the polarity of the second pulse.

In practice, the SE signal can be measured after attenuation by relaxation and molecular diffusion. Thus, the SE signal at a time $2\tau_d$ is

$$e_{2\tau_d} = e_0 \exp\left(-2\tau_d\left(\frac{1}{T_2} + \frac{D\gamma^2 G^2 \tau_d^2}{3}\right)\right), \qquad [2.32]$$

where G is the spatial magnetic field gradient and D is the diffusion coefficient.

If $D\gamma^2 G^2 \tau_d^2 << T_2^{-1}$ then the diffusion effect can be neglected and SEs can be used for measuring the transverse relaxation time constant T_2. For that, SE amplitude is measured for different values of τ_d as shown in Figure 2.22a. Each run consists of two pulses and one SE signal. Plotting SE amplitudes versus time (bottom graph) one can estimate T_2 from

$$e_{2\tau_d} = e_0 \exp(-2\tau_d / T_2)\,. \qquad [2.33]$$

The Hahn's SE is sensitive to the diffusion effect but it is also a time consuming procedure. For that reason, more efficient methods for measuring T_2 have been developed. One of the most common is the CPMG method named after the authors: Carr and Purcell [CAR 54], and Meiboom and Gill [MEI 58]. The method supposes the application of a 90° pulse followed by a 180° pulse delayed at a time τ_d. The first echo measured at a time $2\tau_d$ is the Hahn's echo. Then, 180° pulses separated by time $2\tau_d$ are applied. Each pulse causes refocusing of the nuclear magnetization and the formation of SEs as shown in Figure 2.22b.

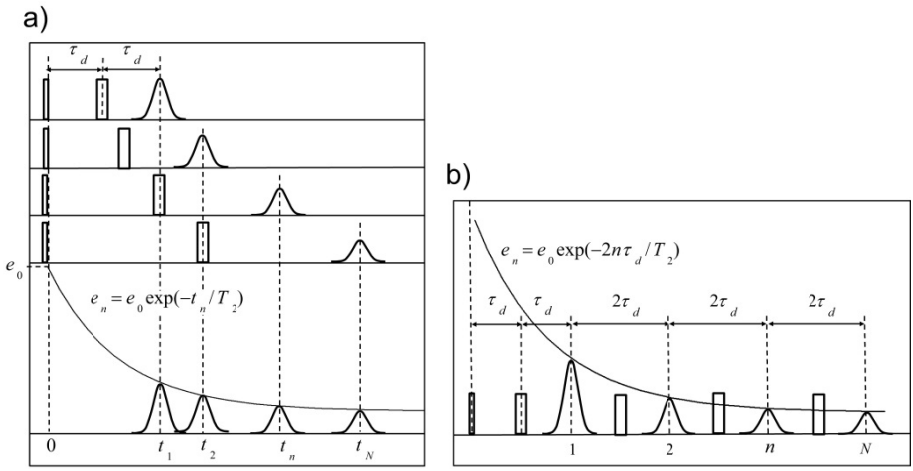

Figure 2.22. *A schematic drawing showing typical procedures for measuring T_2: a) Hahn's echoes with (90°, 180° sequence); b) CPMG method (90°, τ_d, 180°, $2\tau_d$, 180°, $2\tau_d$,..., 180° sequence) with a train of SE*

The envelope of a train of echo amplitudes allows the estimation of T_2 as

$$e_n = e_0 \exp\left(-2n\tau_d\left(\frac{1}{T_2} + \frac{D\gamma^2 G^2 \tau_d^2}{3}\right)\right), \qquad [2.34]$$

where $n=1,2,...,N$ is the number of echoes.

Note, that for measuring T_2 using the Hahn's SE (equations [2.32] and [2.33]), time, and hence τ_d, are progressively increased ($t = 2\tau_d$). However, when using the CPMG method (equations [2.34]) τ_d is constant ($t = 2n\tau_d$) and only the number of echoes in the train N is increased. Thus, rendering τ_d small, we can significantly attenuate the diffusion term. Another advantage of the CPMG method is the time efficiency since the method allows the obtainment of the entire envelope of the echo train in one measuring cycle. For the same number of echoes, the Hahn's method requires N cycles.

For practical realization of the CPMG method, we should wait for a full dephasing between the pulses. Thus,

$$\tau_d > 3T_2^* . \qquad [2.35]$$

At time $2T_2$ relaxation is completed at approximately 85% and we can assume the measuring cycle to be $N2\tau_d = N6T_2^* = 2T_2$. Hence the number of echoes N will be given by

$$N < \frac{T_2}{3T_2^*} . \qquad [2.36]$$

The CPMG method is also sensitive to homogeneity of the static magnetic field and to the imperfection of the excitation pulses. For example, if the pulses are slightly different from 180° then they will cause an error in the T_2 estimation. These items have been discussed in detail in the literature, for example by Majumdar [MAJ 86a; MAJ 86b].

3

Forward Modeling

3.1. The imaging equation

An SNMR field setup consists of transmitting and receiving loops set on the ground, usually in a square, with side lengths between 20 and 150 m. The loop is energized by a pulse of alternating current $i(t) = I_0 \cos(\omega t)$ with the frequency $\omega \approx \omega_0$ close to the Larmor frequency. Measurements of the magnetic resonance signal are made with the same loop after the pulse is terminated. Thus, calculating the SNMR signal consists of two steps: a) calculation of the electromagnetic field generated in the subsurface by the current in the surface loop using the Maxwell equations; b) calculation of the NMR response using the Bloch equations.

For calculating the electromagnetic field of a loop above electrically conductive layers, we approximate the transmitter loop by a vertical magnetic dipole of the moment $M = I_0 \pi a^2$. Its magnetic induction field is symmetrical relative to the dipole axis and considering a receiver located at the point $p(r,z)$, would be expressed as [KAU 83; WAI 82]

$$\mathbf{B}(p) = \mu\left[i\omega\mu\sigma(p)\mathbf{F}(p) - grad(div\mathbf{F}(p))\right] \qquad [3.1]$$

where the electrical properties of the medium are represented by the magnetic permeability μ and the electrical conductivity σ. $\mathbf{F}$ is a Hertz potential which has only a vertical non-zero component, expressed as a Hankel transform

$$F_z(r,z) = \frac{M}{4\pi}\int_0^{\infty} K_d(\lambda,z)\lambda \mathrm{J}_0(\lambda r)d\lambda \qquad [3.2]$$

where λ is the horizontal wave number, a kernel function

$$K_d(\lambda,z) = a_j(\lambda)e^{+m_j z} + b_j(\lambda)e^{-m_j z}, \qquad [3.3]$$

with $m_j = \sqrt{\lambda^2 + i\omega\mu\sigma_j}$ and σ_j being the conductivity of a layer j, the coefficients $a_j(\lambda)$ and $b_j(\lambda)$ are recursively determined and r, z are the radial and vertical distances from the dipole center.

Then the non-zero components of the magnetic induction field can be written as

$$B_r = \frac{\mu M}{4\pi}\int_0^{\infty} \frac{\partial K_d(\lambda,z)}{\partial z}\lambda^2 J_1(\lambda r)d\lambda$$
$$B_z = -\frac{\mu M}{4\pi}\int_0^{\infty} K_d(\lambda,z)\lambda^3 J_0(\lambda r)d\lambda \qquad [3.4]$$

where $J_0(\lambda r)$ and $J_1(\lambda r)$ are the Bessel functions.

Considering the loop with the finite radius a, the kernel can be written as [RYU 70; WAI 82]

$$K_l(\lambda,z) = \frac{J_1(\lambda a)}{\lambda(a/2)}K_d(\lambda,z), \qquad [3.5]$$

and the components of the loop magnetic field become

$$B_r = \frac{\mu I_0 \mathrm{a}}{2}\int_0^{\infty} \frac{\partial K_d(\lambda,z)}{\partial z}\lambda J_1(\lambda a)J_1(\lambda r)d\lambda$$
$$B_z = -\frac{\mu I_0 \mathrm{a}}{2}\int_0^{\infty} K_d(\lambda,z)\lambda^2 J_1(\lambda a)J_0(\lambda r)d\lambda \qquad [3.6]$$

The calculation of the Hankel transform, which is necessary for calculating the loop's magnetic field, requires specific numerical algorithms. The most widely used is the lagged convolution filtering technique [AND 79; AND 89]. Comparison of different numerical routines with a refined filter for the oscillatory kernels proposed by Anderson showed that for all practical needs the standard Anderson's filter will be quite adequate [VAL 02]. However, any other numerical routine can be also used for calculating magnetic fields. Calculation of EM fields was largely covered in the literature considering 1-D [SMY 50; GRO 62; KEL 66; LEE 74; CHA 83; WAR 88; XIO 89; JAC 99; SIN 05; WEI 05] and 3-D subsurface formations [WAN 84; WEI 75; WEI 05; ZHD 09; LEH 11a]. All this experience can help improve SNMR forward modeling, considering different conditions of measurement.

It is known that the magnetic field produced by an oscillating current in a surface loop is linearly polarized and in an arbitrary coordinate system *x,y* can be presented as a vector **A** changing with time along a straight line A`-A`` (Figure 3.1a). However, the driving force in the Bloch equations is a rotating magnetic field. Figure 3.1b shows that a linearly polarized vector **A** can be represented by two equal vectors $(\mathbf{A}/2)^+$ and $(\mathbf{A}/2)^-$ describing a circle, but rotating in opposite directions.

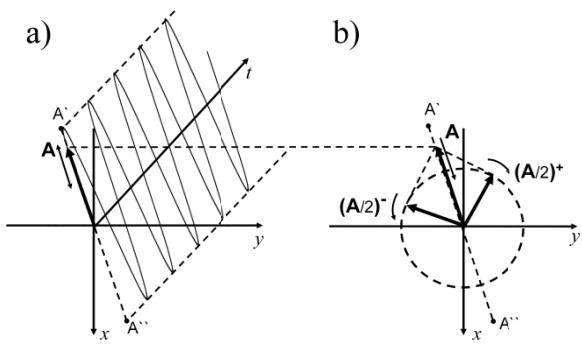

Figure 3.1. *a) Oscillating vector **A** (Acos($\omega t+\varphi_a$)) in an arbitrary coordinate system x,y; b) representation of the linearly polarized vector **A** by two vectors $(\mathbf{A}/2)^+$ and $(\mathbf{A}/2)^-$ rotating in opposite directions*

When conductors are present in the subsurface they produce a secondary magnetic field **B** that is linearly polarized and generally dephased relative to the primary field **A** produced by the loop. Their sum is a third vector **C** that is elliptically polarized as shown in Figure 3.2a. **C** never vanishes but rotates in space, changing continuously in magnitude and describes an ellipse of polarization. The ratio of the minor to the major axis of the polarization ellipse depends on the

magnitudes, directions and phases of the vectors **A** and **B** [GRA 65]. The elliptically polarized vector **C** can be presented as a sum of two vectors $\mathbf{C}^+$ and $\mathbf{C}^-$ rotating in opposite directions (Figure 3.2b).

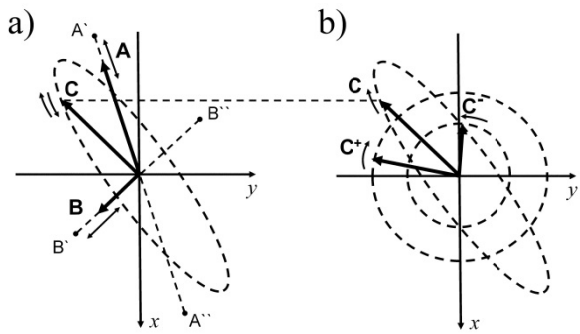

Figure 3.2. *a) Elliptically polarized vector **C** is a sum of two linearly polarized vectors **A** and **B**; b) representation of the elliptically polarized vector **C** by two vectors $\mathbf{C}^+$ and $\mathbf{C}^-$ rotating in opposite directions*

Now we are in a position to combine the Bloch equations and experimental setup typical of SNMR experiments.The loop's magnetic field in the subsurface can be calculated in the coordinate system x^l, y^l, z^l linked to the ground surface and the loop's, axis as shown in Figure 3.3a, for an arbitrary point $\mathbf{r}(x^l, y^l, z^l)$. The reference frame *x, y, z* of the Bloch model (Figure 2.2) is linked to the magnetic fields $\mathbf{B}_0$ and $\mathbf{B}_1$. When the NMR phenomenon is applied to groundwater investigation, the geomagnetic field is the static magnetic field $\mathbf{B}_0$ and the projection of the loop's magnetic field $\mathbf{B}_{loop}$ onto the plane, transverse to the Earth's magnetic field is referred to as $\mathbf{B}_\perp$ and it acts as $\mathbf{B}_1$ (Figure 3.3b). Let us select an arbitrary volume $dV(\mathbf{r})$ that is sufficiently small for assuming that within this volume, the magnetic fields $\mathbf{B}_0, \mathbf{B}_\perp$ are uniform and the local macroscopic spin magnetization $\mathbf{M}$ is constant. Thus, we orient the *z* axis along the geomagnetic field

$\mathbf{B}_0$ which may be inclined at the angle α relative to the ground surface. The x axis is oriented along the magnetic field $\mathbf{B}_\perp$ and then the y axis is automatically set.

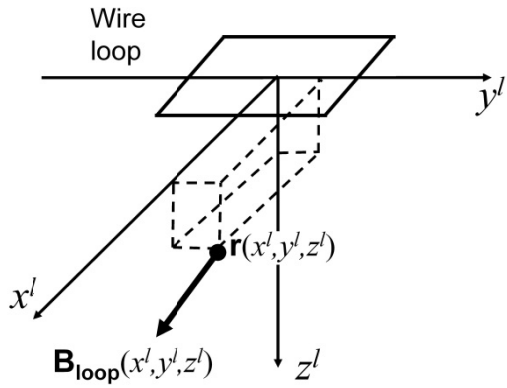

Figure 3.3. *The volume dV being investigated below a surface loop and magnetic fields used for SNMR measurements: a) transmitted by the loop's oscillating magnetic field in the coordinate system x^l,y^l,z^l linked to the ground surface and the loop axis; b) transversal component of the loop magnetic field in the rotating frame of the Bloch model*

For calculating a magnetic resonance signal we first need to calculate it considering a small volume $dV(\mathbf{r})$ and then to integrate this over the entire volume being investigated within the surface loop. For the first step we assume a coincident transmitting and receiving loop (Tx/Rx loop) and that the subsurface is electrically non-conductive.

After the Bloch model, a magnetic moment of volume $dV(\mathbf{r})$ is $M_\perp dV$. A precessing magnetic moment $e^{-j\omega_0 t} M_\perp dV$ can be presented as a small coil of an area ΔS. A magnetic field $B_\perp$ generated by the surface loop is considered uniform over the coil area and a magnetic flux through the coil will be $\Phi_{dV,l} = B_\perp \Delta S$. The flux $\Phi_{dV,l}$ creates a current I_{dV} and a corresponding magnetic moment $I_{dV}\Delta S$.

Hence we can write $M_{\perp} dV = I_{dV} \Delta S$. We can also present a magnetic flux through the coil created by a current in the loop I_0 using $L_{l,dV}$ called the coefficient of mutual inductance between the loop ΔS and the coil. Thus, we obtain $\Phi_{dV,l} = L_{l,dV} I_0$. Also, a magnetic flux through the loop created by the current in the coil I_{dV} is $d\Phi_{l,dV} = L_{dV,l} I_{dV}$. Using the reciprocity theorem we obtain $L_{l,dV} = L_{dV,l}$ and consequently, $d\Phi_{l,dV} I_0 = \Phi_{dV,l} I_{dV}$. Substituting $\Phi_{dV,l} = B_{\perp} \Delta S$ and $I_{dV} \Delta S = M_{\perp} dV$, we obtain $d\Phi_{l,dV} I_0 = B_{\perp} I_{dV} \Delta S = B_{\perp} M_{\perp} dV$. Thus, a voltage induced in the loop by volume dV is $de = -\frac{\partial}{\partial t} d\Phi_{l,dV} = -\frac{\partial}{\partial t}\left(\frac{B_{\perp}}{I_0} e^{-j\omega_0 t} M_{\perp} dV \right)$. In this equation we took into account that the subsurface is non-conductive and there is no phase shift between the signal de and the current I_0. The signal induced in the receiver loop is proportional to the sum of the flux of all the volumes $dV(\mathbf{r})$ and, if we assume the rotating frame and the near resonance conditions, we obtain

$$e_0 = \frac{\omega_0}{I_0} \int_V B_{\perp}(\mathbf{r}) M_{\perp}(\mathbf{r}) w(\mathbf{r}) dV , \qquad [3.7]$$

where $0 \le w(\mathbf{r}) \le 1$ is the water content, and $\mathbf{r} = r(x, y, z)$ is the coordinate vector.

In a non-conductive subsurface the loop's magnetic field $\mathbf{B}_{\perp}$ is linearly polarized and hence it can be presented as clockwise and counterclockwise rotating magnetic fields. The clockwise component which is co-rotating with the Larmor frequency is the driving force in the Bloch equations and thus $B_1 = 0.5 B_{\perp}$. In the case of the FID signal and the exact resonance conditions, equations [2.12] yield

$$M_{\perp} = M_0 \sin(0.5\gamma B_{\perp}\tau_p)\,, \qquad [3.8]$$

where τ_p is a duration of the current pulse in the loop. If we present $B_{\perp}\tau_p = I_0^{-1}B_{\perp}I_0\tau_p = I_0^{-1}B_{\perp}q$ then $\beta_{\perp} = I_0^{-1}B_{\perp}$ is the loop's magnetic field normalized by the current in the loop and $q = I_0\tau_p$ is the pulse moment. Performing measurements with different pulse moments, we can manage the flip angle and thus gain access to the imaging equation for the Tx/Rx configuration

$$\begin{aligned} e_0(q) &= M_0\omega_0 \int_V \beta_{\perp}(\mathbf{r})\sin\left(0.5\gamma\beta_{\perp}(\mathbf{r})q\right)w(\mathbf{r})dV \\ &= \omega_0 \int_V \beta_{\perp}(\mathbf{r})M_{\perp}(\mathbf{r},q)w(\mathbf{r})dV, \end{aligned} \qquad [3.9]$$

where $M_{\perp}(\mathrm{r},q) = M_0\sin(0.5\gamma\beta_{\perp}(\mathrm{r})q)$.

In the case when the transmitting and receiving loops are separated, equation [3.9] could be written as

$$\begin{aligned} e_0(q) &= M_0\omega_0 \int_V (\hat{\mathbf{b}}_{\perp}^{\mathbf{Rx}} \bullet \hat{\mathbf{b}}_{\perp}^{\mathbf{Tx}})\beta_{\perp}^{Rx}(\mathbf{r})\sin\left(0.5\gamma\beta_{\perp}^{Tx}(\mathbf{r})q\right)w(\mathbf{r})dV \\ &= \omega_0 \int_V (\hat{\mathbf{b}}_{\perp}^{\mathbf{Rx}} \bullet \hat{\mathbf{b}}_{\perp}^{\mathbf{Tx}})\beta_{\perp}^{Rx}(\mathbf{r})M_{\perp}(\mathbf{r},q)w(\mathbf{r})dV \end{aligned}, \qquad [3.10]$$

where $M_{\perp}(\mathbf{r},q) = M_0\sin\left(0.5\gamma\beta_{\perp}^{Tx}(\mathbf{r})q\right)$, $\hat{\mathbf{b}}_{\perp}^{\mathbf{Rx}}$ and $\hat{\mathbf{b}}_{\perp}^{\mathbf{Tx}}$ are the unit direction vectors for the receiving $B_{\perp}^{Rx}$ and transmitting $B_{\perp}^{Tx}$ magnetic fields respectively.

An electrically conductive subsurface causes a phase shift φ_0^{Tx} of the transmitted magnetic field $\mathbf{B}_\perp^{\mathbf{Tx}}$ relative to the current in the loop and the voltage induced in the receiving loop is dephased relative to an oscillating magnetic moment $\mathbf{M}_\perp$ at an angle φ_0^{Rx}. Consequently, the voltage becomes complex and the imaging equation can be written as

$$e_0(q) = \omega_0 \int_V e^{j(\varphi_0^{Tx}+\varphi_0^{Rx})} (\hat{\mathbf{b}}_\perp^{\mathbf{Rx}} \bullet \hat{\mathbf{b}}_\perp^{\mathbf{Tx}}) \beta_\perp^{Rx}(\mathbf{r}) M_\perp(\mathbf{r},q) w(\mathbf{r}) dV \ . \qquad [3.11]$$

In the case of the coincident Tx/Rx loop configuration $\varphi_0^{Rx} = \varphi_0^{Tx}$, the imaging equation is

$$e_0(q) = \omega_0 \int_V e^{j2\varphi_0^{Tx}} \beta_\perp(\mathbf{r}) M_\perp(\mathbf{r},q) w(\mathbf{r}) dV \ . \qquad [3.12]$$

In highly conductive subsurfaces, a magnetic field transmitted by the loop becomes elliptically polarized. The imaging equation for the coincident Tx/Rx loop configuration thus becomes [WEI 00]

$$e_0(q) = 2\omega_0 \int_V e^{j2\varphi_0^{Tx}} \beta_\perp^-(\mathbf{r}) M_\perp(\mathbf{r},q) w(\mathbf{r}) dV \ , \qquad [3.13]$$

where $M_\perp(\mathbf{r},q) = M_0 \sin\left(\gamma\beta_\perp^+(\mathbf{r})q\right)$, $\beta_\perp^+(\mathbf{r})$ and $\beta_\perp^-(\mathbf{r})$ are the co-rotating (clockwise) and counter-rotating (counterclockwise) components of the normalized loop magnetic field.

When using separated Tx and Rx loops, the magnetic resonance response can be calculated as

$$e_0(q) = 2\omega_0 \int_V e^{j(\varphi_0^{Tx}+\varphi_0^{Rx})} (\hat{\mathbf{b}}_\perp^{\mathbf{Rx}} \bullet \hat{\mathbf{b}}_\perp^{\mathbf{Tx}}) \beta_\perp^{-Rx}(\mathbf{r}) M_\perp(\mathbf{r},q) w(\mathbf{r}) dV \,, \qquad [3.14]$$

where $M_\perp(\mathbf{r},q) = M_0 \sin(\gamma\beta_\perp^{+Tx}(\mathbf{r})q)$, $\beta_\perp^{+Tx}(\mathbf{r})$ is the normalized co-rotating magnetic field of the transmitting loop and $\beta_\perp^{-Rx}(\mathbf{r})$ is the normalized counter-rotating magnetic field of the receiving loop.

The influence of the elliptical polarization on the SNMR response has been studied numerically [WEI 00; VAL 02; HER 08]. Results show that this effect is small and can generally be neglected. Only when working in areas where the Earth's magnetic field is close to horizontal, the subsurface is very conductive and when investigating heterogeneous 3-D water saturated formations should this effect be taken into account.

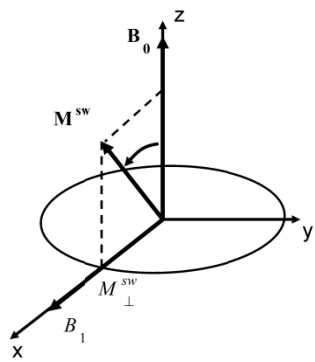

Figure 3.4. *Evolution of the nuclear magnetization **M** in the rotating frame ofthe Bloch model caused by a strong oscillating magnetic field*

It has been experimentally observed that a large oscillating magnetic field causes the nuclear magnetization to rotate in the *x,z* plane (Figure 3.4) thus creating a non-zero transversal projection $M_x = M_\perp^{sw}$. This component generates an additional

voltage in the surface loop that depends on the magnitude of the magnetic field B_1 and the relaxation time T_1. In practice, this additional signal is generated by the water in shallow water-saturated formations, irradiated by a strong magnetic field B_1 and composed of coarse material (gravel, sand) characterized by long T_1 values. The phenomenon has been reported in the literature [WEI 02; LEG 04a], but until now, no acceptable theoretical explanation has been proposed. Thus, for the interpretation of SNMR measurements we use an empirical estimate of this additional signal as

$$e_0^{sw}(q) = \omega_0 \int_V e^{j(\pi/2)} \beta_\perp(\mathbf{r}) M_\perp^{sw}(\mathbf{r}, q) w(\mathbf{r}) dV \,. \qquad [3.15]$$

where $M_\perp^{sw}(\mathbf{r}, q) = \alpha_{sw} M_0 \beta_\perp^{Tx}(\mathbf{r}) q T_1^2$ and α_{sw} is an empirical constant developed for measurements with a pulse of fixed duration. In equation [3.15] we neglect a phase shift caused by the electrically conductive subsurface because the shallow-water signal can be observed only in the first 10-15 m of the subsurface and the phase shift is usually small.

Thus, the signal amplitude measured with SNMR method becomes

$$e_{SNMR}(q) = e_0(q) + e_0^{sw}(q) \,. \qquad [3.16]$$

3.2. The Earth's magnetic field

For performing SNMR measurements, the Earth's magnetic field is employed as the static field $\mathbf{B_0}$. However, the Earth's magnetic field is not constant around the world. Depending on the geographical location of the area being investigated with SNMR, the geomagnetic field changes its intensity and inclination (Figure 3.5).

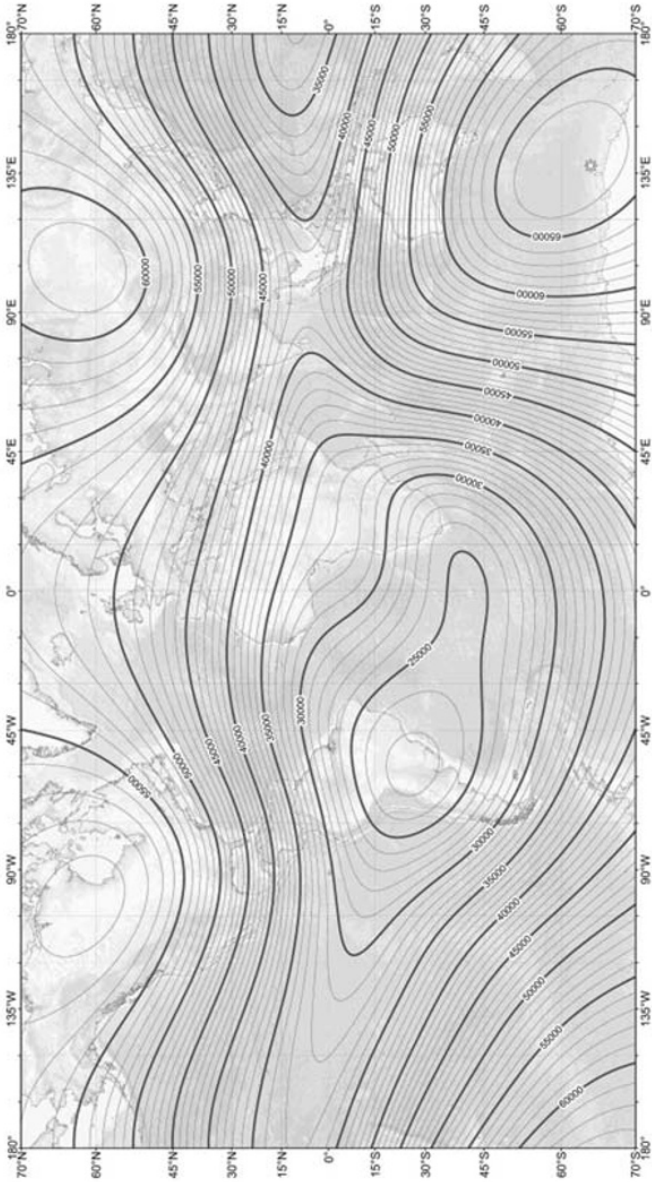

Figure 3.5. *Global maps showing the worldwide distribution of the intensity B_0 in nT (top) and the inclination in degrees of the Earth's magnetic field (bottom). (WMM-2010 magnetic data, US-National Oceanic and Atmospheric Administration (NOAA), http://www.ngdc.noaa.gov/seg/geomag)*

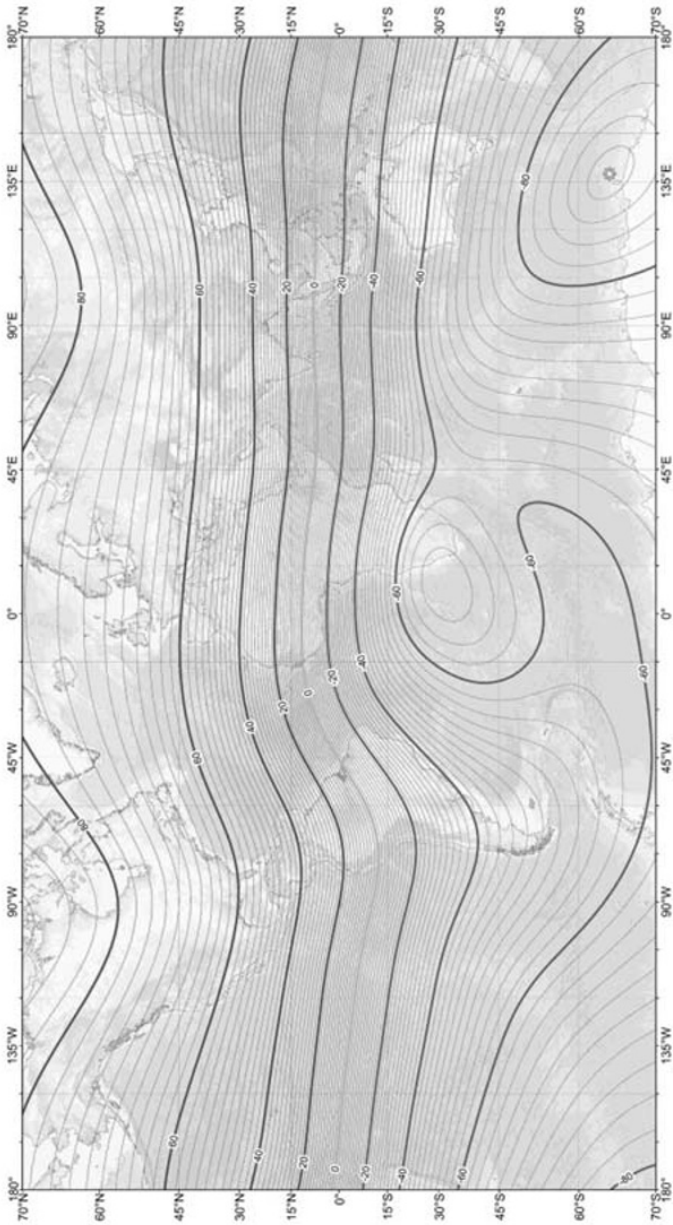

Figure 3.5. *(Continued)*

These variations have an impact on SNMR results [LEG 97]. Primarily, the amplitude of the NMR signal is proportional to the square of the geomagnetic field $e_0 \sim B_0^2$. Indeed, it follows from equation [3.9] that $e_0 \sim M_0 \times \omega_0$, but $M_0 \sim B_0$ (equation [2.5]) and $\omega_0 \sim B_0$ (equation [2.4]). Consequently, in northern Siberia and Canada where B_0 is about 60,000 nT, the same water saturation formation would generate a magnetic resonance signal four times higher than in South America where B_0 is about 30,000 nT. Additionally, only the transverse component of the loop magnetic field $B_\perp$ is the driving force in the Bloch equations and the inclination of the geomagnetic field should be taken into account.

We know that for observing an NMR signal, the static magnetic field $\mathbf{B_0}$ has to be homogeneous. In the laboratory, special measures allow us to obtain homogeneous magnetic fields within a small volume where the samples being investigated are located. However, the SNMR method operates within a great volume, using the Earth's magnetic field, and it is obvious that the geomagnetic field cannot be managed. Fortunately, the Earth's magnetic field is sufficiently homogeneous for performing NMR measurements and it is usually considered as a constant parameter. However, the Earth's magnetic field can vary over time and it can be locally perturbed by rocks. Rocks may cause lateral or vertical perturbations (or both) of the geomagnetic field as shown in Figure 3.6.

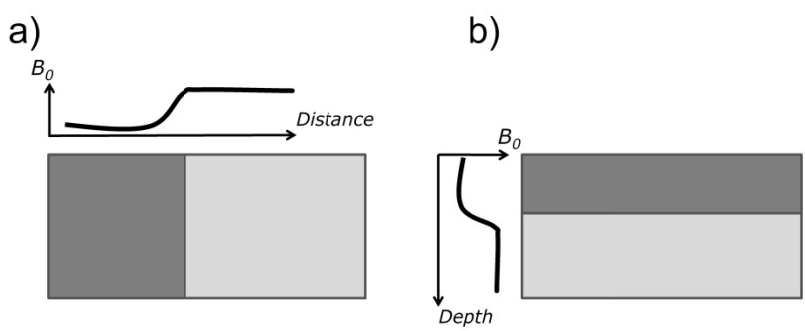

Figure 3.6. *Possible perturbations of the Earth's magnetic field caused by magnetic rocks: a) the lateral perturbation; b) the vertical perturbation*

The lateral perturbation can be often detected from the surface using a proton magnetometer, but the vertical perturbation is more difficult to detect. Note, that even when measurements with a magnetometer do not reveal variations in the geomagnetic field, the NMR signal may be perturbed by local variations of the geomagnetic field. The aquifer formation may be composed of magnetic or non-magnetic material, but in both cases NMR measurements can be perturbed. Figure 3.7 shows possible locations of the magnetic rock relative to the aquifer being investigated. In the case where magnetic rocks are deep, this formation can be considered as a flat magnet and the magnetic basement creates a homogeneous field gradient (Figure 3.7a). In this case, when the basement is close to the aquifer, its shape may be non-regular and perturbations of the geomagnetic field in the aquifer will also be complex (Figure 3.7b). In some cases, small magnetic particles, such as magnetite grains, may be mixed up with the aquifer material thus perturbing the geomagnetic field on the grain-size scale (Figure 3.7c).

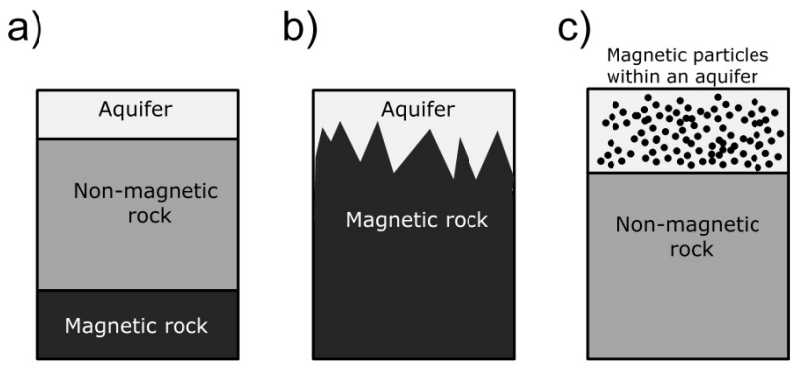

Figure 3.7. *Possible location of the magnetic rock that causes local perturbations of the geomagnetic field: a) a deep magnetic basement; b) a shallow magnetic basement; c) distributed magnetic particles within an aquifer*

Depending on the heterogeneity of the geomagnetic field, SNMR can be used either in the FID or SE modes. In both cases, SNMR allows us to estimate the water content and T_2^* relaxation time. T_1 or T_2 relaxation times can be accessed in FID mode or SE mode respectively. Often, both FID and SE can be observed [LEG 10; VOU 11]. In the case when the perturbation is large, the SNMR method cannot be used (Figure 3.8).

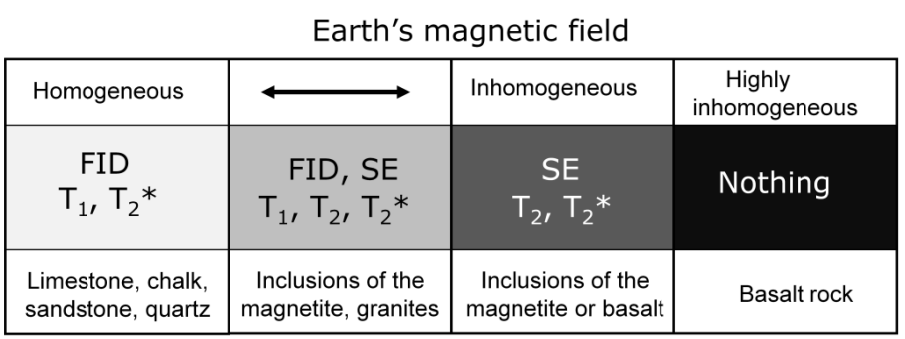

Figure 3.8. *Qualitative correspondence between the homogeneity of the Earth's magnetic field and measuring techniques to use for SNMR survey. The bottom row indicates what rock may cause the perturbation*

3.3. Modeling typical SNMR signals

In the previous sections we have seen that the SNMR signal is strongly dependent on the measuring conditions: the measuring setup, the Earth's magnetic field, the location of the water-saturated formations being investigated, and the electrical and magnetic properties of the subsurface. To learn more about SNMR signals we will use a forward modeling routine based on equation [3.12] and considering a 1-D sounding setup with the coincident Tx/Rx loop. We assume that the measurements are in FID mode (measuring the free induction decay signals) with the maximum pulse moment of 12,000 A-ms and dead-time of the equipment of 40 ms. Parameters that we used for the 1-D modeling are presented in Table 3.1.

Model parameters	***Models***						
Model number	**1**	**2**	**3**	**4**	**5**	**6**	**7**
Figure	3.9	3.10	3.11	3.12	3.13	3.14	3.15
Inclination of the Earth's magnetic field (°)	**var**	45	45	90	90	**var**	90

Table 3.1. *The parameters used for the 1-D forward modeling*

Larmor frequency f_0 (Hz)	**var**	2000	2000	2600	2600	2000	2600
Resistivity of the subsurface (Ωm)	100	100	100	100	**var**	100	100
Square loop (m^2)	80×80	80×80	80×80	80×80	80×80	80×80	80×80
Depth to water (m)	0	**var**	10	5	**var**	**var**	**var**
Thickness of water saturated formation (m)	100	2	**var**	5	10	**var**	10
T_1 (ms)	200	200	200	**var**	200	200	200
Modeling goal	Maximum possible signal	Depth to water	Aquifer thickness	Shallow water effect	Resistivity effect	Inclination of the Earth's magnetic field	Off resonance condit-ions

Table 3.1. *(Continued)*

Model 1

SNMR signals that have been calculated considering the half-space of bulk water are shown in Figure 3.9. These results may be considered as an estimate of the maximum possible amplitude of the magnetic resonance signal as a function of the Earth's magnetic field: a) a horizontal and weak geomagnetic field typical of equatorial areas, b) an average-magnitude geomagnetic field with the inclination of 45° corresponding to Europe location and c) a strong vertical geomagnetic field in polar areas. Note that depending on the geographical location of the area being investigated with SNMR, the same volume of water produces different signals (remember that $e_0 \sim B_0^2$) and hence the efficiency of the method should be higher in areas with a large geomagnetic field.

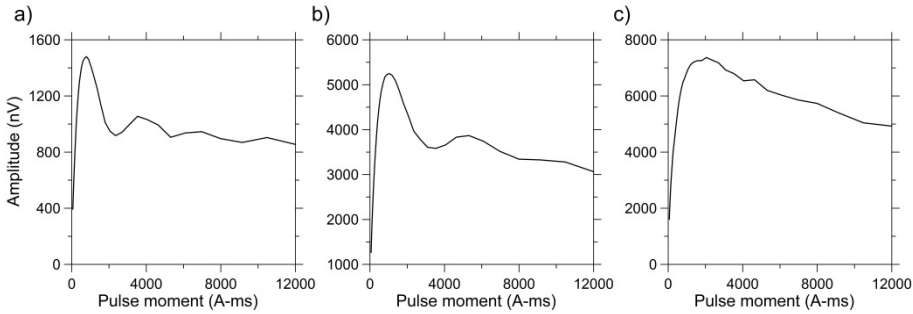

Figure 3.9. *Amplitude of the SNMR signal versus pulse moment calculated, considering the half-space of bulk water (w=100%, T_2^*=1000 ms) and the Earth's magnetic field of the following magnitude and inclination respectively: a) 23,474 nT (f_0=1000 Hz) and 0°; b) 46,948 nT (f_0=2000 Hz) and 45°; c) 61,033 nT (f_0=2600 Hz) and 90°*

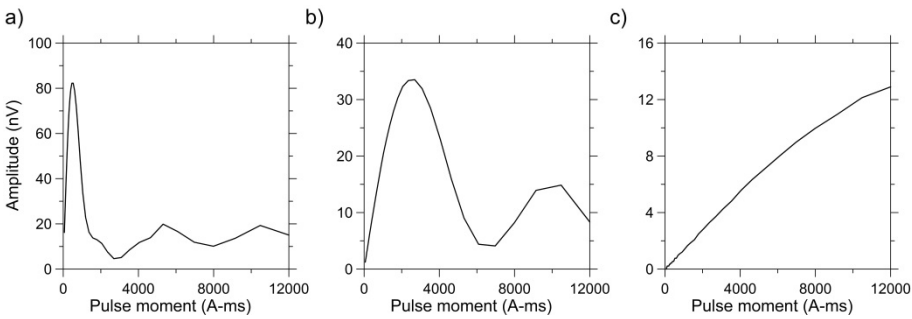

Figure 3.10. *Amplitude of the SNMR signal versus pulse moment calculated, considering a two-m-thick water saturated formation (w=20%, T_2^*=150 ms): a) depth to water 5 m; b) depth to water 30 m; c) depth to water 80 m*

Model 2

The SNMR response from a thin (two-m-thick) water-saturated formation (*w=20%,* T_2^**=150 ms*), located at different depths (5, 30 and 80 m) is shown in Figure 3.10. One can see that shallow water, produces a sharp SNMR signal and an SNMR response from a deep layer is almost a straight line (the initial part of the sine function). Note the relationship between the signal's maximum amplitude and the layer depth: a larger pulse moment corresponds to a greater depth.

Model 3

Figure 3.11 shows how an SNMR response depends on the thickness of the water-saturated formation being investigated. In this example two water-saturated layers (*w=20%*) are located at depths of 10 and 40 m. The thickness of these layers varies from 10 to 30 m. One can see that a greater thickness of the formation causes the maximum amplitude of the SNMR's response to shift towards large pulse moments and the *e (q)* plot becomes wider.

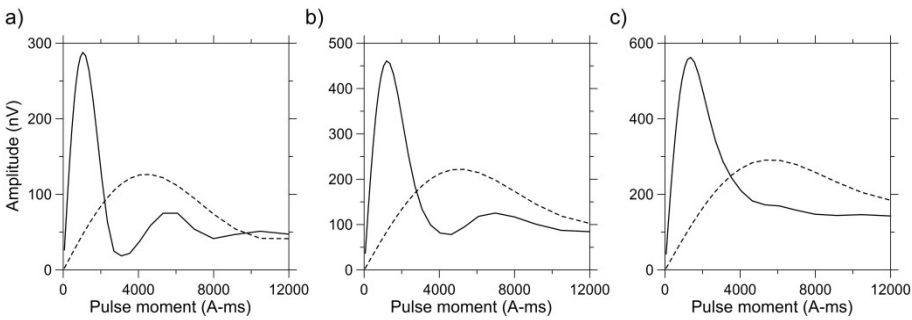

Figure 3.11. *Amplitude of the SNMR signal versus pulse moment computed considering two water saturated formations (depth to water 10 m (solid line) and 40 m (dashed line), w=20%, T_2^*=150 ms) of various thickness: a) 10 m; b) 20 m; c) 30 m*

Model 4

This model demonstrates the effect of the presence of shallow water-saturated formations on the SNMR response, and the influence of the T_1 relaxation time on the amplitude and phase of the SNMR signal in this case (Figure 3.12). We can see that in the presence of shallow water the amplitude is linearly increasing for larger pulse moments. This signal is similar to the signal generated by deep water and the phase should be used for discriminating between the shallow and deep water signals: the shallow water signal has a negative phase shift and the deep water signal has no phase shift.

Note that with the pulse moment limited by 12,000 A-ms, water at 30 m deep does not produce the shallow water signal.

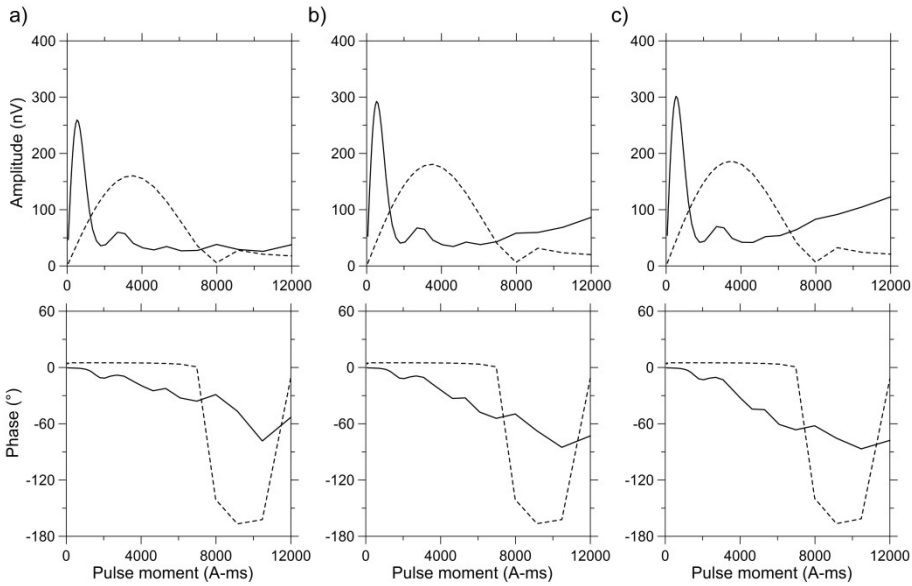

Figure 3.12. *Amplitude (top) and phase (bottom) of the SNMR signal versus pulse moment, calculated considering a 5-m-thick water-saturated formation (depth to water 5 m (solid line) and 30 m (dashed line), w=20%, $T_2^*=T_1$) and assuming different T_1: a) 200 ms; b) 500 ms; c) 800 ms*

Model 5

SNMR signals that are calculated considering an increasing electrical conductivity of the subsurface (Figure 3.13) show that the effect of the electrical conductivity on the signal is different for shallow and deep water. The amplitude of the signal from the shallow formation increases slightly when the subsurface is electrically conductive, which can be explained by the deformation of the loop's magnetic field. The phase shift is relatively small because it depends on the product of the subsurface's conductivity and the thickness of the conductive rock between the loop and the water-saturated formation. The signal calculated from the deep formation is attenuated by the subsurface and the phase shift is also significant. Note that in this example the effect of the shallow water signal is small because of the short T_1 and the effect of the electrically conductive subsurface is dominant.

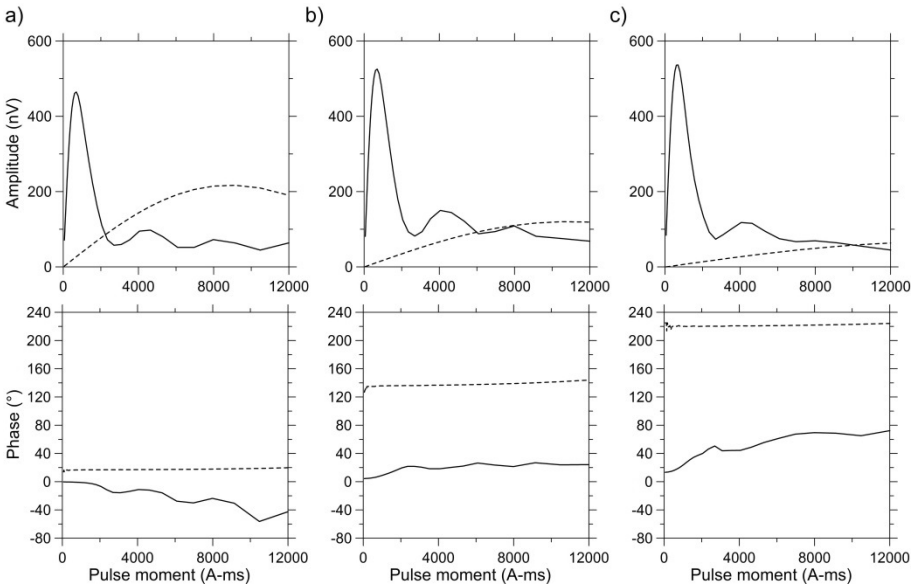

Figure 3.13. *Amplitude (top) and phase (bottom) of the SNMR signal versus pulse moment calculated considering a 10-m-thick water-saturated formation (depth to water 5 m (solid line) and 50 m (dashed line), w=20%, T_2^*=150 ms) and assuming the half-space of different resistivity: a) 100 ohm-m; b) 10 ohm-m; c) 5 ohm-m*

Model 6

Modeling was performed assuming a fixed geomagnetic field (Larmor frequency of 2,000 Hz) and varying only the inclination of the Earth's magnetic field. This approach allows the separation of the effects of the magnitude and of the inclination on the SNMR response. Modeling results (Figure 3.14) show that the amplitude of the SNMR signal is largest when the Earth's magnetic field is horizontal. We also observe that the maximum of the signal generated by the same water-saturated formation is achieved with smaller pulse moments. Thus, the use of incorrect values of the inclination for interpretation may cause additional errors in interpretation.

However, the effect of the inclination of the Earth's magnetic field is less important than the effect of its magnitude. Indeed, the signal amplitude changes by about 65% when the inclination of the geomagnetic field varies from 0° to 90°, but considering the threefold variation in the magnitude of the geomagnetic field (from 20,000 to 60,000 nT), one can see that the amplitude will change approximately ninefold.

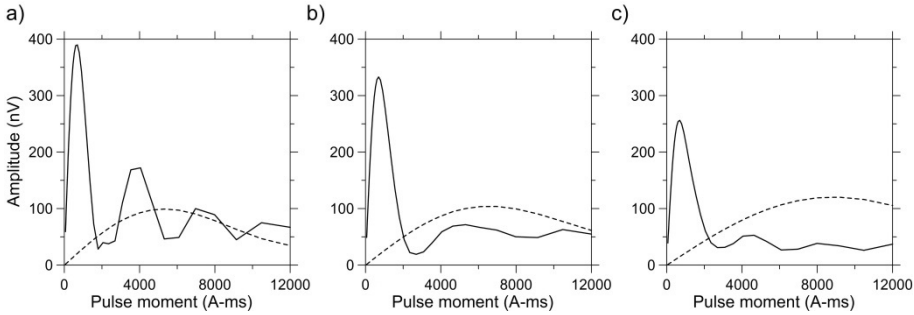

Figure 3.14. *Amplitude of the SNMR signal versus pulse moment calculated considering two 10-m-thick water-saturated formations (depth to water 5 m (solid line) and 50 m (dashed line), w=20%, T_2^*=150 ms). The Larmor frequency was set to 2,000 Hz and the inclination of the Earth's magnetic field was varying: a) 0°; b) 45°; c) 90°*

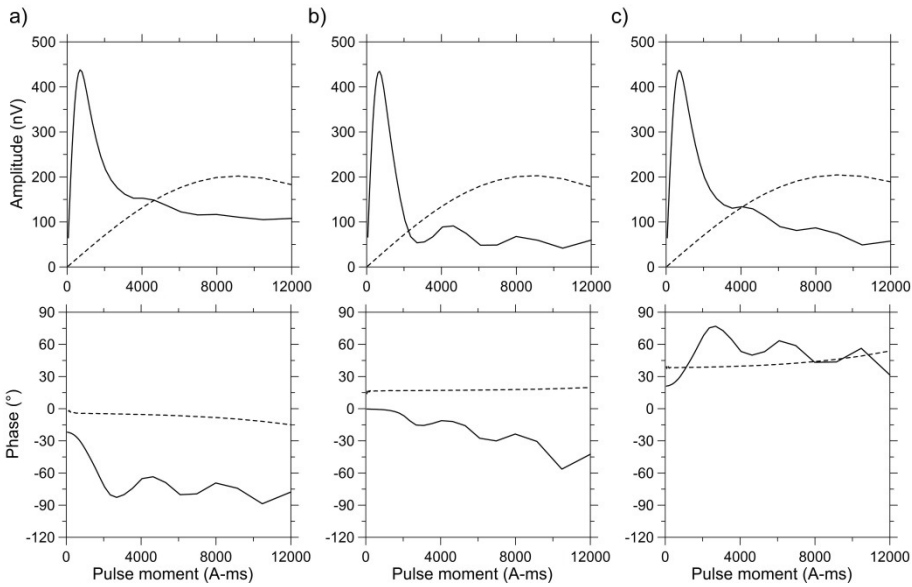

Figure 3.15. *Amplitude of the SNMR signal versus pulse moment calculated considering two 10-m-thick water-saturated formations (depth to water 5 m (solid line) and 50 m (dashed line), w=20%, T_2^*=150 ms). The frequency offset $\Delta\omega$ ($\Delta\omega=\omega_0-\omega$, where ω_0 is the Larmor frequency and ω is the pulse frequency) was varying: a) -3 Hz; b) 0 Hz; c) +3Hz*

Model 7

This model demonstrates the behavior of the SNMR signal under off-resonance conditions (Figure 3.15). The signal was calculated considering a 10-m-thick water-saturated layer located at 5 and 50 m. A 3 Hz frequency offset was assumed for both positive and negative frequency shifts. Modeling results show that shallow water is more sensitive to the frequency offset than water at 50 m deep. In both cases the amplitude changes only for shallow formations, but the phase varies for both deep and shallow water. Depending on the frequency offset, the phase can have positive or negative shifts.

It is known that the amplitude of the SNMR signal decreases with increasing depth. For example, Figure 3.16 shows the amplitude calculated considering a 1-m-thick layer of bulk water (w=100%, T_2^*=1,000 ms) plotted against the depth of this layer.

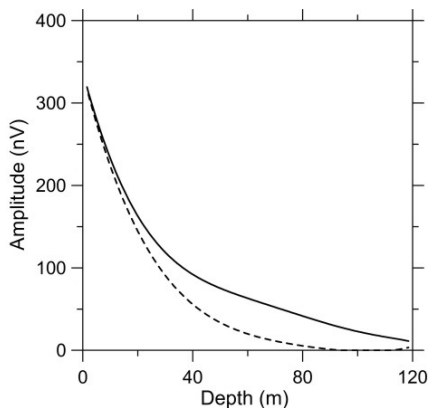

Figure 3.16. *Amplitude of the SNMR signal versus depth calculated considering a 1-m-thick layer of bulk water (w=100%, T_2^*=1,000 ms), a square loop with 80-m-sides, a Larmor frequency of 2,000 Hz and an inclination of the Earth's magnetic field of 45°. The half-space resistivity was assumed to be 100 ohm-m (solid line) and 5 ohm-m (dashed line)*

Such a graph can be considered as an estimate that gives us an idea about the depth of investigation with the SNMR method. However, the amplitude of the signal depends on the loop size, measuring conditions and the amount of water in the subsurface. For example, when the subsurface is more conductive, the SNMR signal will be attenuated as shown in Figure 3.16 (dashed line). Consequently, the depth of investigation should be estimated for each particular case.

The figure-eight loop is composed of two circles or two squares and generally exhibits similar features as a circular or square loop. It has been shown [TRU 95] that in the 1-D case, orientation of the figure-eight loop relative to the north-south direction has a small effect on the SNMR signal and, in the majority of cases, can be neglected.

In the SE mode, the SNMR signal has similar features to those of the FID mode, but it has smaller amplitude. For example, Figure 3.17 shows the initial amplitude of the FID and SE signals, calculated without taking into account the transverse relaxation. The SE amplitude was calculated assuming the second pulse to be twice as large as the first pulse. One can see that the SE signal from a shallow water-saturated formation has the amplitude of about 75% of the FID amplitude. For a deep formation, the SE amplitude is only about 50% of the FID amplitude. Note that for measuring SE, the pulse duration should be two to three times shorter than when measuring FID signals (15 ms instead of 40 ms). Shorter pulses are necessary due to a large band of the SE signal. Consequently, the maximum pulse moment available for SE measurements is more than twice as small, and the depth of investigation with the SE is also smaller than in FID mode.

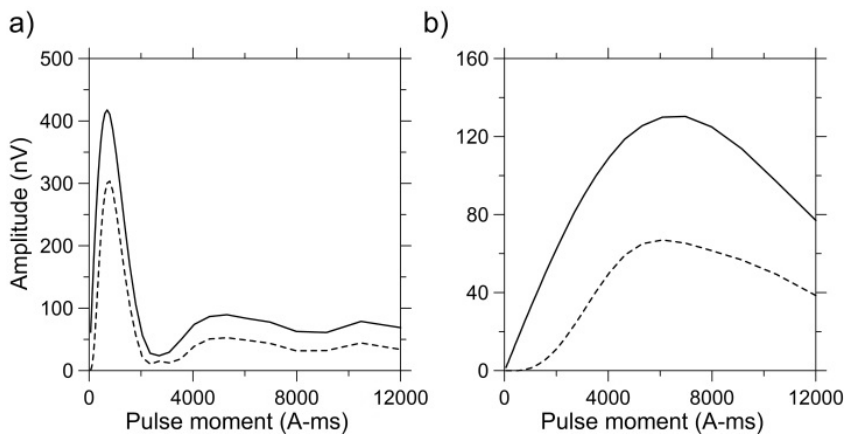

Figure 3.17. *Amplitude of the SNMR signal versus pulse moment calculated for two 10-m-thick water saturated formations (w=20%) neglecting transverse relaxation effects and considering FID (solid line) and SE (dashed line) signals. The Larmor frequency was set to 2,000 Hz, the inclination of the Earth's magnetic field was 45° and the resistivity of the subsurface was 100 ohm-m. Depth to water was set: a) 5 m; b) 50 m*

It has been shown that the SE signal is strongly attenuated by the transverse relaxation and diffusion [LEG 10] and the practical performance of the SNMR method in SE mode is not as good as in FID mode. However, in the presence of magnetic material in the subsurface, the FID signal may be strongly affected or could even be undetectable and the use of the SE allows for considerably improved SNMR results [VOU 11].

3.4. 3-D sensitivity of the SNMR loop

When investigating 1-D water-saturated formations, we assume that the subsurface is horizontally stratified and thus the SNMR signal is attributed to the total volume affected by the measuring loop, without paying attention to the contribution of different parts of the subsurface. However, SNMR can also be applied to the 1-D configuration (just one loop) in the areas that are not perfectly homogeneous. For example, this may be the case when investigating hard rock areas and the measuring loop is laid over a fractured zone. If the SNMR results indicate a good aquifer, then hydrogeologists ask where within the loop area a well should be drilled. The loop has a size of a few hundred square meters and often it is recommended to set a borehole in the center of the loop. Let us see whether such a recommendation would be always the best location for drilling.

It was shown in the previous sections that the driving force necessary for generating the SNMR signal is the transversal to the Earth's magnetic field component of the oscillating magnetic field transmitted by the surface loop. Consequently, the inclination of the Earth's magnetic field is an important parameter that defines the sensibility map within the one loop area being investigated. For calculating the contribution of the different parts of the subsurface to the SNMR signal we assume a square loop with an 80 m side, a Larmor frequency of 2,000 Hz and a resistivity of the subsurface of 100 ohm-m. We performed numerical modeling assuming the inclination of the Earth's magnetic field to be 0°, 45° and 90°.

Modeling results are shown in Figures 3.18–3.26. The area affected by the SNMR loop is presented by the isosurface at the level arbitrarily set at 8 nV (Figures 3.18, 3.21 and 3.24). Two horizontal slices at the depth of 10 and 20 m show the contribution of different areas (Figures 3.19, 3.22 and 3.25). Two cross-sections corresponding to two W-E profiles, north and south of the loop's axis, show the vertical distribution of the sensitivity along the profiles (Figures 3.20, 3.23 and 3.26).

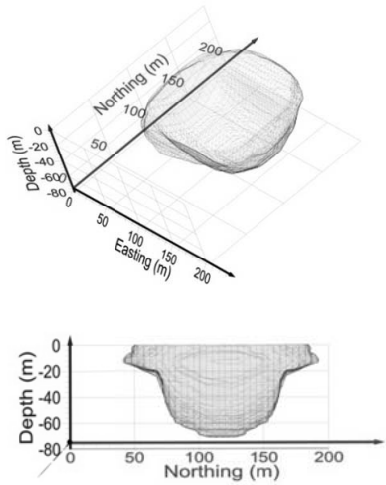

Figure 3.18. *Isosurface of the amplitude of the SNMR signal plotted at the level of 8 nV and calculated assuming the inclination of the Earth's magnetic field to be 0°. The area within this isosurface could be considered as the area investigated with one loop*

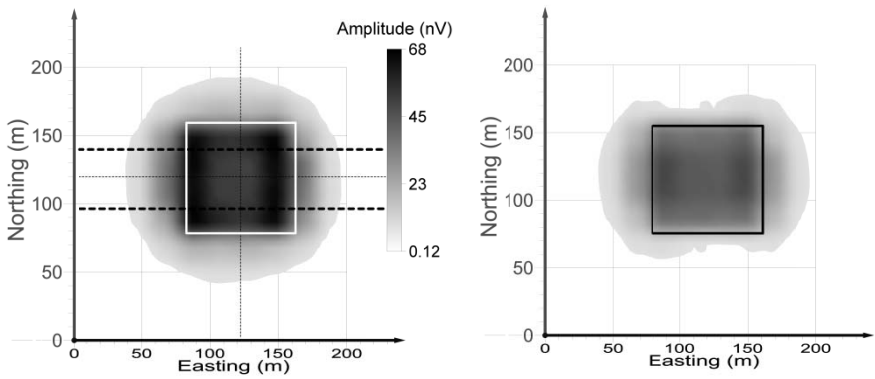

Figure 3.19. *Horizontal slices at the depth of 10 m (left) and 20 m (right) below the loop showing the amplitude of the SNMR signal calculated considering the inclination of the Earth's magnetic field of 0°. The position of the square loop is shown by a square in the center of the image (on the left) and two horizontal dashed lines show southern and northern (relative to the loop axis) profiles*

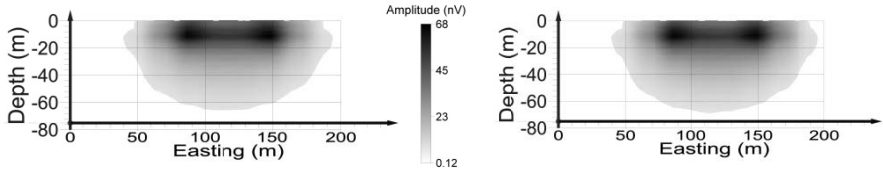

Figure 3.20. *Northern (left) and southern (right) cross-sections corresponding to the northern and southern profiles shown in the previous figure present the amplitude of the SNMR signal calculated considering the inclination of the Earth's magnetic field of 0°*

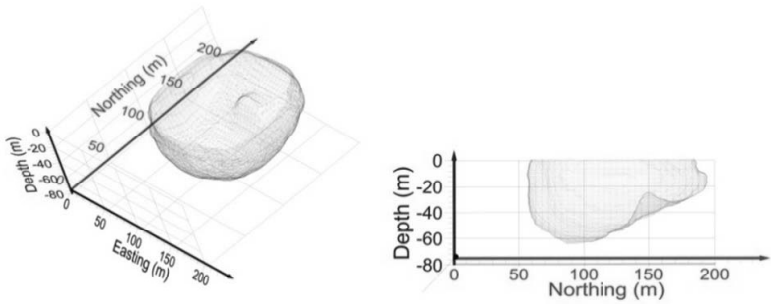

Figure 3.21. *Isosurface of the amplitude of SNMR signal plotted at the level of 8 nV calculated assuming the inclination of the Earth's magnetic field to be 45°. The area within this isosurface could be considered as the area investigated with one loop*

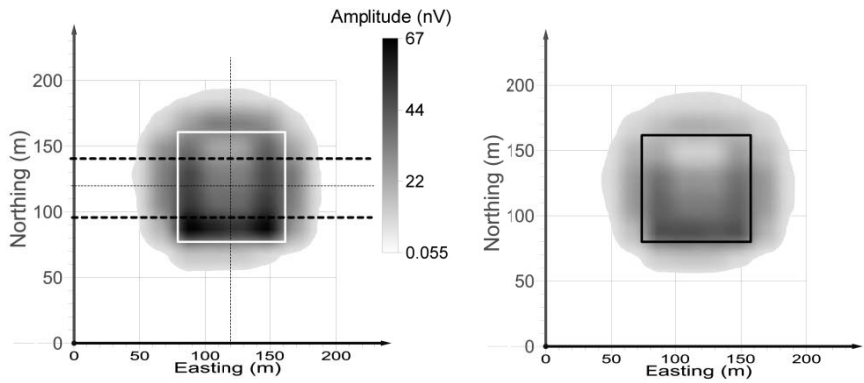

Figure 3.22. *Horizontal slices at the depth of 10 m (left) and 20 m (right) below the loop showing the amplitude of the SNMR signal calculated considering the inclination of the Earth's magnetic field of 45°. The position of the square loop is shown by a square in the center of the image (on the left) and two horizontal dashed lines show southern and northern (relative to the loop axis) profiles*

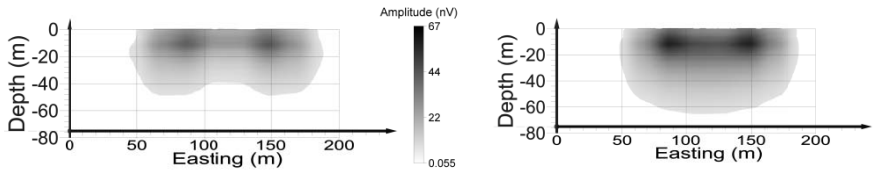

Figure 3.23. *Northern (left) and southern (right) cross-sections corresponding to the northern and southern profiles shown in the previous figure present the amplitude of the SNMR signal calculated considering the inclination of the Earth's magnetic field of 45°*

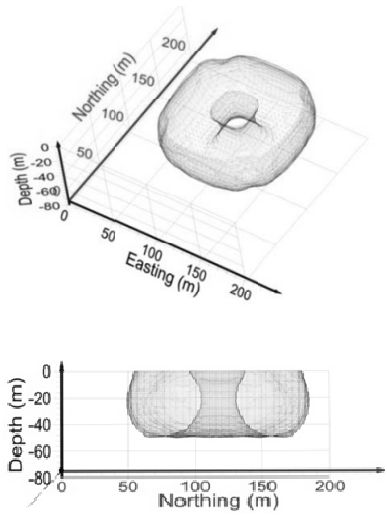

Figure 3.24. *Isosurface of the amplitude of SNMR signal plotted at the level of 8 nV calculated assuming the inclination of the Earth's magnetic field to be 90°. The area within this isosurface could be considered as the area investigated with one loop*

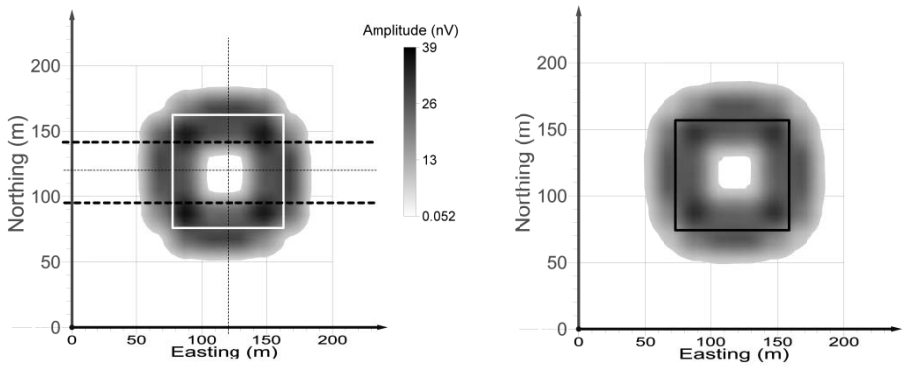

Figure 3.25. *Horizontal slices at the depth of 10 m (left) and 20 m (right) below the loop showing the amplitude of the SNMR signal calculated considering the inclination of the Earth's magnetic field of 90°. The position of the square loop is shown by a square in the center of the image (on the left) and two horizontal dashed lines show southern and northern (relative to the loop axis) profiles*

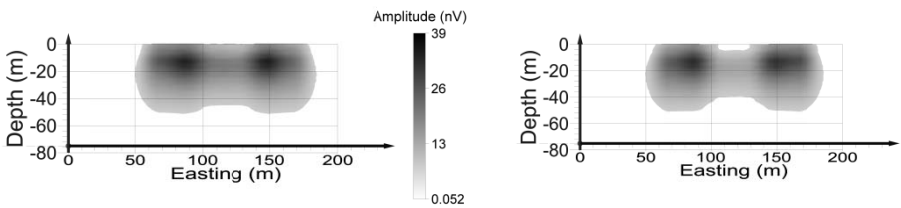

Figure 3.26. *Northern (left) and southern (right) cross-sections corresponding to the northern and southern profiles shown in the previous figure present the amplitude of SNMR signal calculated considering the inclination of the Earth's magnetic field of 90°*

Modeling results presented above show that the sensitivity of the loop progressively diminishes when the depth increases and, at the same depth, the sensitivity varies laterally as a function of the inclination of the Earth's magnetic field. Depending on its location within the loop-affected area, the same volume of water may produce an SNMR signal that varies fourfold. When the Earth's magnetic field is close to the horizontal, the central area has the maximal sensitivity. However, when the Earth's field is close to vertical, the central area around the loop's axis does not produce any signal. It is obvious that in such a case a recommendation to locate a well in the center of the SNMR loop may be unjustified.

When the inclination of the geomagnetic field changes from horizontal to vertical, the most sensitive area is displaced towards the southern part of the loop in the northern hemisphere and towards the northern part of the loop in the southern hemisphere.

It would be instructive to demonstrate the effect of the electrically conductive subsurface on the sensitivity distribution of the SNMR loop. Figures 3.27–3.29 show the sensitivity of the loop considering the inclination of the geomagnetic field of 0°. These figures can be compared with the sensitivity distribution calculated for the same loop but considering a low conductive subsurface (Figures 3.18–3.20). One can see that the electrically conductive rocks attenuate the SNMR signal thus diminishing the depth of investigation, but also that the sensitivity distribution changes.

Note that the sensitivity map becomes non-symmetric because the effect of the elliptical polarization on the SNMR signal becomes significant.

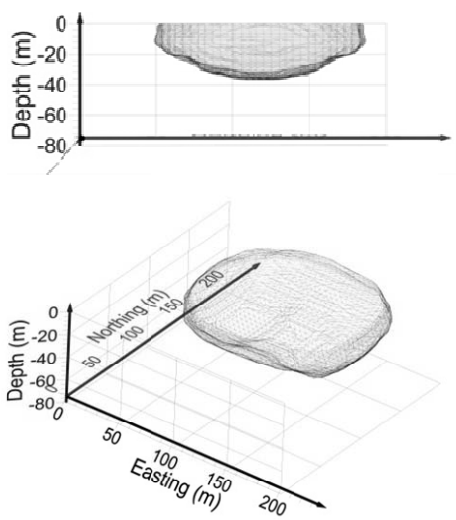

Figure 3.27. *Isosurface of the amplitude of SNMR signal plotted at the level of 8 nV calculated assuming the inclination of the Earth's magnetic field to be 0° and the resistivity of the half-space to be 2 ohm-m. Area within this isosurface could be considered as the area investigated with one loop*

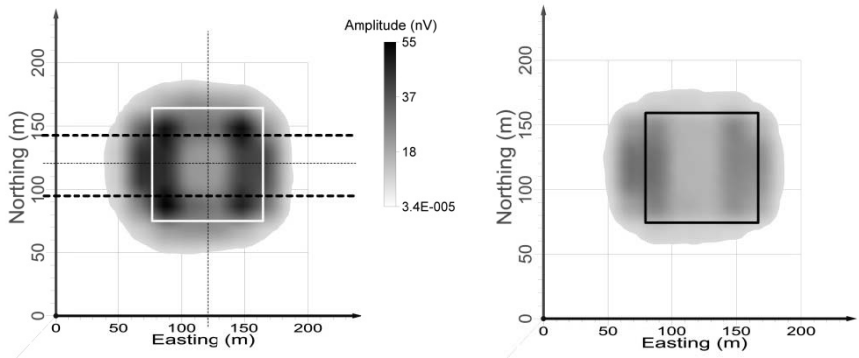

Figure 3.28. *Horizontal slices at the depth of 10 m (left) and 20 m (right) below the loop showing the amplitude of the SNMR signal calculated considering the inclination of the Earth's magnetic field of 0° and the resistivity of the half space of 2 ohm-m. The position of the square loop is shown by a square in the center of the image (on the left) and two horizontal dashed lines show the southern and northern (relative to the loop axis) profiles*

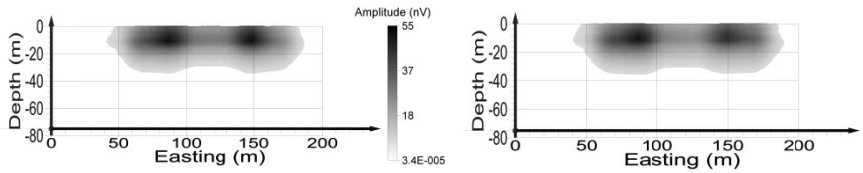

Figure 3.29. *Northern (left) and southern (right) cross-sections corresponding to the northern and southern profiles shown in the previous figure present the amplitude of the SNMR signal calculated considering the inclination of the Earth's magnetic field of 0° and the resistivity of the half space of 2 ohm-m*

Figures 3.30–3.32 show the effect of the electrically conductive subsurface on the sensitivity distribution of the SNMR loop considering the vertical geomagnetic field. One can compare these results with the case of a low electrical conductivity (Figures 3.24–3.26). Note, that in the case of the vertical geomagnetic field, the effect of the elliptical polarization is small and can be neglected. Only an attenuation of the signal amplitude takes place.

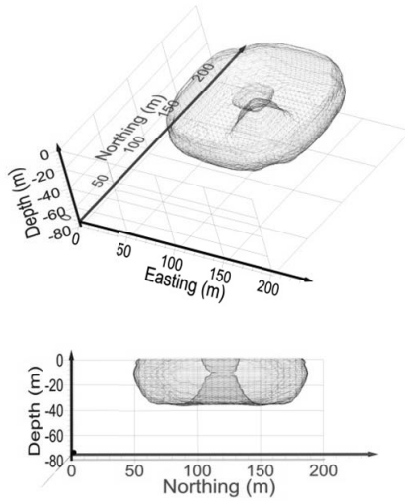

Figure 3.30. *Isosurface of the amplitude of the SNMR signal plotted at the level of 8 nV calculated assuming the inclination of the Earth's magnetic field to be 90° and the resistivity of the half-space to be 2 ohm-m. The area within this isosurface could be considered as the area investigated with one loop*

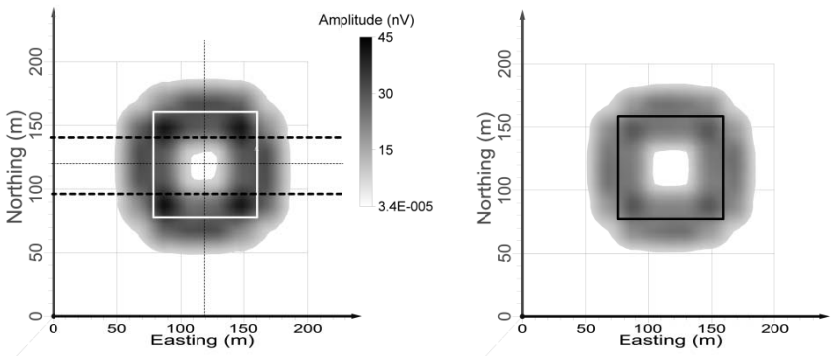

Figure 3.31. *Horizontal slices at the depth of 10 m (left) and 20 m (right) below the loop showing the amplitude of the SNMR signal calculated considering the inclination of the Earth's magnetic field of 90° and the resistivity of the half space of 2 ohm-m. The position of the square loop is shown by a square in the center of the image (on the left) and two horizontal dashed lines show southern and northern (relative to the loop axis) profiles*

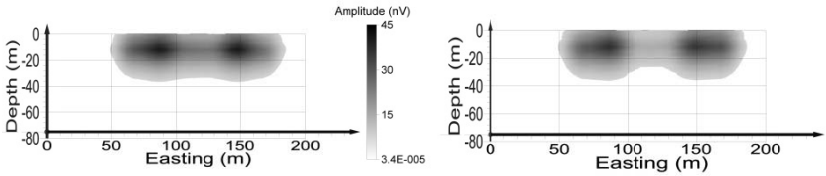

Figure 3.32. *Northern (left) and southern (right) cross-sections corresponding to the northern and southern profiles shown in the previous figure present the amplitude of the SNMR signal calculated considering the inclination of the Earth's magnetic field of 90° and the resistivity of the half space of 2 ohm-m*

Thus, we have shown using numerical modeling examples that the contribution of the different areas below the SNMR loop to the total signal is not equal and that the distribution of the sensitivity of the loop depends on the inclination of the geomagnetic field and on the electrical conductivity of the subsurface.

3.5. Experimental verification

Since the 1980s, the SNMR method has been tested in different geological conditions. However, in porous media the NMR phenomenon becomes more complex and for direct verification of the imaging equation we use a physical model consisting of bulk water in an open reservoir (usually frozen lakes) [SCH 91; LEG 04b; MÜL 11]. A fresh water reservoir represents the simplest physical model. However, modeling conditions can be rendered more difficult and hence the verification will be more comprehensive when water is electrically conductive (saline water), the Earth's magnetic field is not constantand the reservoir has limited size (3-D geometry). For experimental verification of the modeling routine we used two different water reservoirs.

The 1-D measurements were performed in Sweden using a 100×100 m^2 square loop. The Baltic Sea at the test site had a depth of 17 m covered by about a 1-m-thick ice sheet. The test site was located close to a river and thus sea water had variable salinity. The electrical resistivity measured in water samples varied from 36 ohm-m at shallow depths to about 3 ohm-m closer to the bottom (Figure 3.33). Measurements of the water temperature revealed a vertical gradient from 0.1 to 0.9°C. The sea bed was composed of magnetic rocks creating a significant vertical gradient of the geomagnetic field. Under these conditions it was possible to measure both the FID and SE signals. However, the geomagnetic field mapped with a proton magnetometer revealed only very small lateral variations with an average of 52,512 nT and a corresponding Larmor frequency of 2,237 Hz. The vertical gradient

of the Larmor frequency was derived from the inversion of SNMR measurements (Figure 3.33). The inhomogeneous geomagnetic field caused the off-resonance conditions that rendered the FID envelope non-exponential.

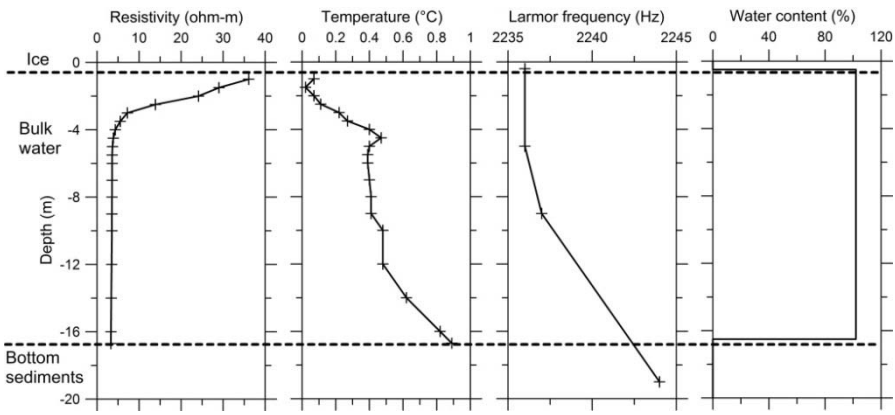

Figure 3.33. *Thickness and physical parameters of water corresponding to the investigated site in Sweden (Baltic Sea)*

1-D SNMR complex signals for the FID and SE experiments were calculated, taking into account the thickness and physical parameters of the water layer (Figure 3.33).

Figure 3.34 shows that the calculated 1-D amplitude fits the experimental data well for both the FID and SE measurements. The theoretical phase also follows the general trend of the observed signals, but a good fit was achieved only for the FID signal.

In the SE mode the phase modeling requires a more sophisticated modeling routine, but also a more accurate phase measuring. For calculating the SE signal, attenuation caused by the transverse relaxation has been taken into account (delay between the pulses τ_d = 482 ms and measured T_2 = 1,340 ms).

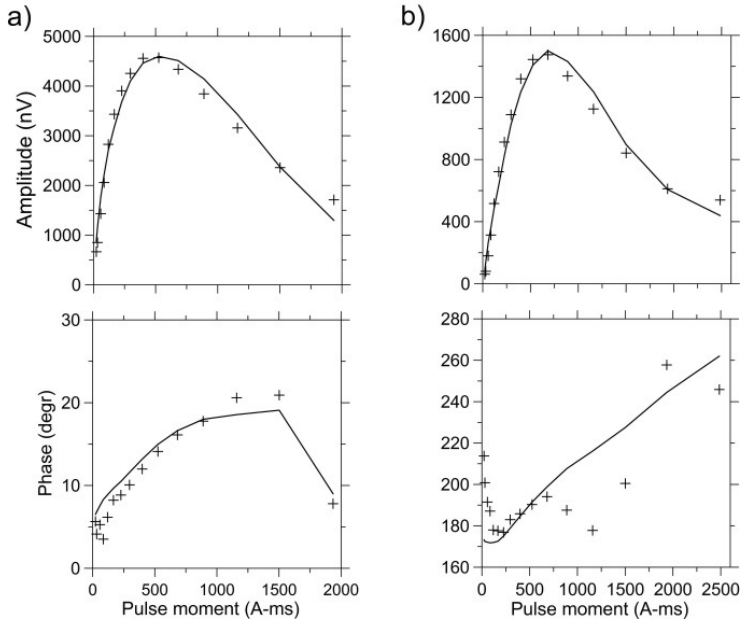

Figure 3.34. *Verification of the 1-D modeling in the Baltic Sea. Experimental (crosses) and modeled (solid line) amplitude (top graphs) and phase (bottom graphs) of the SNMR signal plotted against the pulse moment considering two measuring modes: a) FID; b) SE*

The 3-D modeling was verified using an artificial water reservoir located in the southern part of the island of New Caledonia. In this pool, approximately 80×30 m^2 large, the bottom varied from approximately 1.5 to 4 m (Figure 3.35a). A rectangular loop of 100×50 m^2 was put around the pool. Rocks in this area are characterized by a magnetic susceptibility between 5e-4 and 5e-3 SIU and perturb the geomagnetic field.

However, these perturbations are relatively small in the pool and we were able to measure both the FID and SE signals. The geomagnetic field was 47,246 nT and the Larmor frequency was about 2,013 Hz. The water body in the pool was approximated by a four-box model of bulk water (w=100%) as shown in Figure 3.35b.

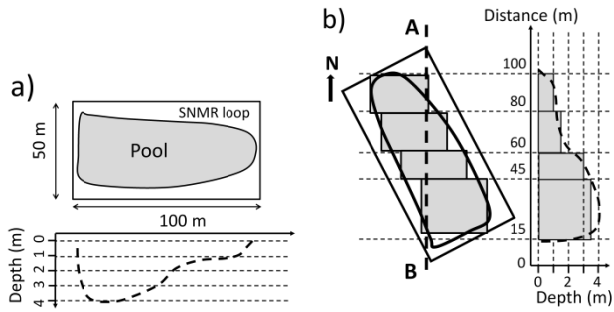

Figure 3.35. *3-D SNMR modeling with an artificial pool on New Caledonia as a physical model: a) geometry of the pool; b) four-box model of the water body with a cross-section corresponding to the profile A-B*

Figure 3.36 shows that calculated amplitudes fit experimental data well for both FID and SE measurements. We should keep in mind that the pool geometry was known with limited accuracy. Calculated phases also follow the general trend of the observed signals. Similar to the 1-D case presented in the previous example, the correspondence between measured and calculated phases is better for FID signals.

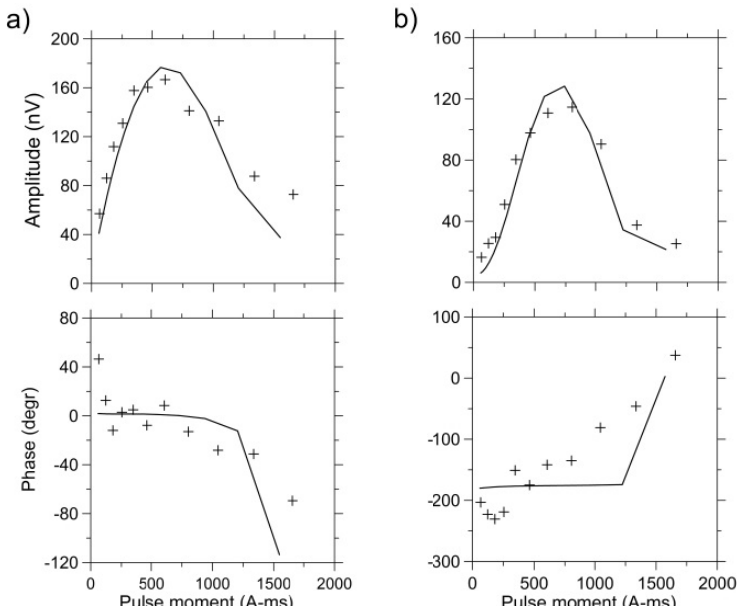

Figure 3.36. *Verification of the 3-D modeling using SNMR measurements on New Caledonia. Experimental (crosses) and modeled (solid line) amplitude (top graphs) and phase (bottom graphs) of the SNMR signal plotted against pulse moments considering two measuring modes: a) FID; b) SE*

Our verification of the mathematical model (equations [3.15] and [3.16]) would be incomplete if we did not look at SNMR measurements in the presence of water-saturated formations at shallow depths. For that, we will just reinterpret data that has already been published.

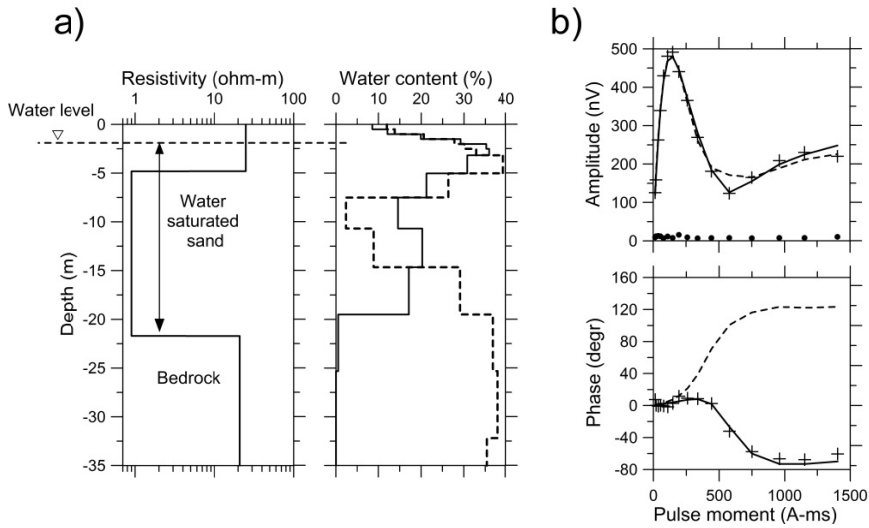

Figure 3.37. *Example of SNMR results from the test site in India: a) the resistivity log given by TDEM measurements (left) and the water content against depth (right) derived from FID inversion shown for two cases: when correction for shallow water was applied (solid line) and without such a correction (dashed line); b) measured FID amplitude (top) and phase (bottom) versus pulse moment are shown by crosses; the theoretical signal corresponding to inversion with applied correction for shallow water is shown by a solid line and without correction by a dashed line. Black dots show noise magnitudes*

The first survey area is located in India and more information about this site can be found in the literature [LEG 10] and [VOU 12]. SNMR measurements have been performed with a 50×50 m^2 square loop composed of two turns of wire. This site is located at a distance of about 500 meters from a strong magnetic anomaly, which perturbs the geomagnetic field thus creating a small heterogeneity, but which is sufficient for rendering the FID signal envelope Gaussian rather than exponential. *In situ* measurements of the T_1 relaxation time revealed 1,400 ms thus suggesting an aquifer composed of coarse sand. The vertical distribution of the SNMR water content derived from the inversion of SNMR measurements (Figure 3.37a, solid line) shows that the water level was about 2 m deep, which was in good agreement with the ground truth. The inversion shows the water content between 20 and 30% with more water close to the surface. Laboratory measurements of the porosity of

the sand samples extracted from the depth between 0 and 5 m ranged from 26 to 36%. Moreover, the SNMR results are in good agreement with TDEM. The resistivity log distinguishes three layers: the shallow low-conductivity layer corresponds to a fresh water aquifer, the high conductivity layer shows a saline water aquifer, and a deep, low conductivity layer represents the basement. The maximum depth of detection for a 1-m-thick layer of bulk water estimated for this site was about 35 m for FID measurements. We can consider this estimate as the maximum depth of investigation. Figure 3.37b shows the measured amplitude and phase of the FID signal versus the pulse moment and the theoretical signal reconstructed after inversion results. When using, for inversion, the correction for shallow water, which is given by equation [3.15], the inversion shows a good fit with experimental data (solid line). When this correction was not applied the measured amplitude can still fit reasonably well, but the measured phase cannot (dashed line). Note that the water distribution model that allows the amplitude to fit is incompatible with the geology of the test site (Figure 3.37a, dashed line). Such a deep aquifer is called the phantom aquifer and it is an artifact of the inversion.

The second test site is located near Luitel Lake at an altitude of 1250 m in the Belledonne *massif* in the French Alps. The subsurface in this area is composed of three geological formations: water saturated peat, porous material (weathered rock, glacial till and compacted peat) and basement rock. Water distribution in this peat bog has been studied with 2-D SNMR, ground penetrating radar (GPR) and electrical resistivity tomography (ERT) [LEG 11b]. Investigated with SNMR, part of the peat bog is an ancient lake which was only recently covered with peat. SNMR measurements were performed using the 18×18 m^2 square Tx/Rx loop (two turns) connected to a reference loop of the same size. The noise reducing setup was necessary because a big power line passes near the study area and the noise measured by the square loop without using the compensation loop was too high (between 3000 and 8000 nV). The use of the reference loop and of the stacking procedure (100 stacks) reduced the noise to the level of 15 to 20 nV and thus the signal-to-noise ratio was much improved. In the area below the loop the peat body represented a non-consolidated mud and GPR measurements showed the water content estimate between 64 and 70%. This estimate is consistent with what one would expect in water-saturated peat. The results of the 1-D inversion of the SNMR signals measured at the center of the bog where the subsurface could be considered homogeneous are presented in Figure 3.38. Figure 3.38a shows that the principal water storage zone is approximately 7–8 m thick with the water content estimated at being between 60 and 70% which is in good agreement with ERT and GPR results. Because of a high water content, we may expect a long relaxation time in the peat, but the measured relaxation time of the SNMR signal ranged from 90 to 130 ms for T_2^* and about 210 ms for T_1. Such a low relaxation time was caused by the surface

relaxivity rate in peat, which is higher than in rocks. The maximum depth of detection for a 1-m-thick layer of bulk water is estimated to be about 15 m which can be considered as the maximum depth of investigation for this sounding setup and noise magnitude.

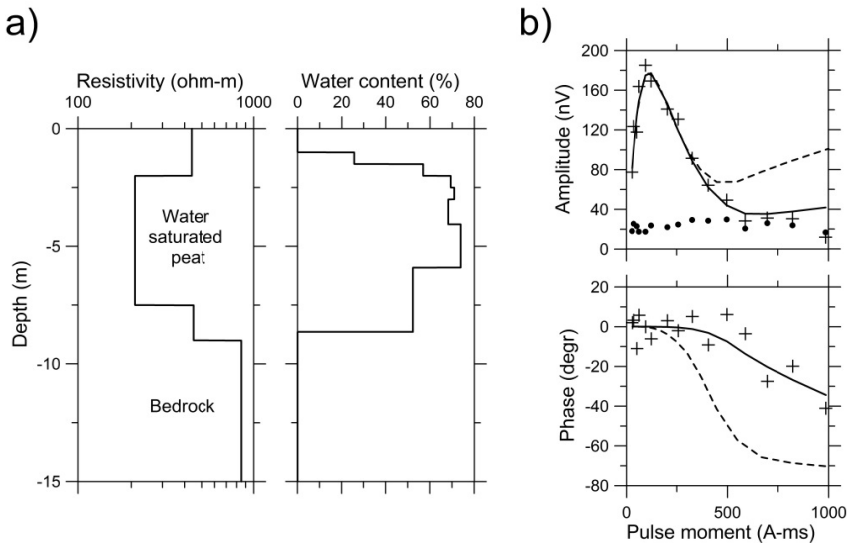

Figure 3.38. *Example of SNMR results from the peat bog at Luitel Lake: a) the resistivity log given by ERT measurements (left) and the water content (right) derived from FID inversion against depth; b) measured FID amplitude (top) and phase (bottom) against the pulse moment. The theoretical signal was calculated using results of the inversion carried out with applied correction for shallow water considering two cases: measured T_1=210 ms (solid line) and assuming that T_1=1,400 ms could be expected for bulk water (dashed line). Black dots show the noise magnitude*

We can see that both the measured amplitude and phase of the SNMR signal (Figure 3.38b) are well fitted by the theoretical signal calculated after the inversion result (solid line) carried out by applying the correction for shallow water and taking into account the measurement of T_1's value. For demonstration purposes we calculated a complex SNMR signal, assuming the geometry of the reservoir to be the same but with a longer relaxation time T_1 (dashed line) than the previous example, and corresponding to water-saturated coarse sand (1,400 ms). One can see that we cannot reproduce experimental data in this case. This example clearly demonstrates that the shallow water effect could be observed only when the relaxation time T_1 is long.

Thus, experimental verification of the imaging equation used for interpretation of SNMR measurements confirmed that this equation can be used for calculating the magnetic resonance signal from water-saturated geological formations. However, it should be understood that the NMR phenomenon is sensitive to the lithological composition of the rocks being investigated and to the distribution of internal magnetic field gradients on the pore-size scale. Consequently, for accurately calculating an SNMR response, we should know the parameters of these rocks with the pore-size resolution. It is obvious that knowledge of geological formations with such accuracy is not possible and hence SNMR results can only be an approximation.

4

Inversion

4.1. The SNMR inverse problem

Inversion in geophysics can be defined as the process of transforming experimental data into a quantitative rock-property description. Inversion may be deterministic, random or geostatistical, and may include other geophysical or geological information, such as well logs and cores. Detailed analysis of existing inversion algorithms is beyond the scope of this book, but readers can find a comprehensive presentation of inverse problem theory in different textbooks, for example [AST 05] and [TAR 05].

SNMR inversion enables the transformation of SNMR measurements into hydraulic properties of water-saturated rock. As for the majority of geophysical inverse problems, the inversion of SNMR data is ill-posed. This means that the solution is not unique and many different solutions may fit experimental data equally well. Reported developments in different domains of SNMR inversion can be found in the literature: [LEG 98a; GUI 02a; GUI 02b; HER 02; MOH 02; WEI 02; BRA 05; HER 05; MOH 05; BRA 07; HER 07; MÜL 08; BEH 12a; BEH 12b; GÜN 12]. In this chapter, the presentation of SNMR inversion will focus on the practical aspects of data interpretation, taking into account particular properties of the SNMR integral equation.

Any inverse problem is composed of three principal components: a set of data represented by a vector d, a mathematical model represented by a function G and a model of the subsurface represented by a vector m. G relates d and m as

$$G(m) = d \,. \qquad [4.1]$$

In practice, the experimental data set is composed of a finite number of measurements **d**. We can also express the model as a finite-element vector **m**. Such

problems are called discrete inverse problems that can be written as an equation system

$$G(\mathbf{m}) = \mathbf{d}\,. \qquad [4.2]$$

In order to build an SNMR inversion procedure let us consider the principal components as follows.

*1) The SNMR model of the subsurface (**m**)*

To represent the continuous physical properties of the subsurface, we can approximate the subsurface using a model composed of homogeneous cells, so that each of these cells has just one value for each physical property. Examples of the discretization of the subsurface for 1-D, 2-D and 3-D inversions are shown in Figure 1.11. In the 1-D case, the subsurface can be approximated by infinite horizontal layers, in the 2-D case by the parallelepipeds infinite in the transversal to the profile direction, and in the 3-D case by finite-size boxes. Note that the size of the cells may be unequal, depending on the complexity of the subsurface and on the resolution of the inversion.

The physical properties of the subsurface that can be derived from SNMR measurements are the following: 1) the water content (w); 2) the relaxation time constants (T_1, T_2 and T_2^*); 3) the electrical resistivity (ρ); 4) the Larmor frequency ($f_0 = \omega_0 \times (2\pi)^{-1}$) directly linked to the magnitude of the Earth's magnetic field ($\omega_0 = \gamma \times B_0$, equation [2.4]).

*2) The SNMR data set (**d**)*

An experimental data set for an SNMR inversion depends on the measuring procedure. In general, SNMR response is measured by time records of the voltage induced in the receiver loops following one or more excitation pulses generated in the transmitting loop. The intensity and duration of each current pulse, the phase shift between the current in each pulse and the time intervals between the pulses compose a set of imaging parameters which allows for an exploration of the subsurface. The number, location and size of SNMR measuring loops constitute additional imaging parameters. Whatever the signal processing scheme, an SNMR data set for inversion, measured with each loop, consists of one or more measured parameters: 1) the initial amplitude of the FID or SE signals versus the pulse moment $e_0(q)$, the pulse moment being a product of the current amplitude and its

duration $q = I_0 \times \tau$); 2) the relaxation times versus the pulse moment ($T_1(q)$, $T_2(q)$ and $T_2^*(q)$); 3) the phase versus the pulse moment ($\varphi_0(q)$); 4) the frequency offset between the Larmor frequency and the current frequency ($\Delta\omega(q) = \omega_0(q) - \omega$).

3) SNMR mathematical model (G)

A general equation for the SNMR inverse problem can be formulated as

$$e(q_p, t) = G\left(w(\mathbf{r}), T_1(\mathbf{r}), T_2(\mathbf{r}), T_2^*(\mathbf{r}), \rho(\mathbf{r}), \Delta\omega(\mathbf{r}) \right), \qquad [4.3]$$

where $e(q_p, t)$ is a set of the time records of voltage induced in the receiving loops, following excitation pulses in the transmitting loops. The excitation pulses are characterized by the pulse moment q_p, which depends on the measuring procedure. Thus, when the position of the measuring loops is fixed, q_p is the imaging parameter. The SNMR inverse problem allows for a transformation of the time series $e(q_p, t)$ measured by varying q_p into a spatial distribution of the water content, the relaxation times, and the resistivity and magnitude of the Earth's magnetic field: $w(\mathbf{r})$, $T_1(\mathbf{r})$, $T_2(\mathbf{r})$, $T_2^*(\mathbf{r})$, $\rho(\mathbf{r})$, $\Delta\omega(\mathbf{r})$.

SNMR measuring procedures and corresponding imaging equations have been discussed in Chapters 2 and 3. To start with, let us consider just one coincident Tx/Rx loop and FID1 measurements with one current pulse (equation [3.12]) that allows us to also measure the relaxation time T_2^*. In this case the imaging equation can be written as

$$e_1(q,t) = \int_V \omega_0(\mathbf{r}) \beta_\perp(\rho(\mathbf{r}), \mathbf{r}) M_\perp(\Delta\omega(\mathbf{r}), \rho(\mathbf{r}), q, \mathbf{r}) w(\mathbf{r}) \times$$
$$\exp\left(-t / T_2^*(\mathbf{r}) \right) \cos\left(\omega_0(\mathbf{r}) t + 2\varphi_0^{Tx}(\rho(\mathbf{r}), \mathbf{r}) \right) dV \qquad [4.4]$$

For measuring T_1 one can apply the saturation recovery method (section 2.3.1) with two equal pulses separated by a time delay τ_d. However, taking into account real field conditions, $T_1(\mathbf{r})$ measurements with the SNMR will be more accurate when using the modified saturation recovery scheme presented in Figure 2.18. Consequently the imaging equation is

$$\begin{aligned} e_2(q,\tau_d,t) = -\int_V & \omega_0(\mathbf{r})\beta_\perp(\rho(\mathbf{r}),\mathbf{r})M_\perp(\Delta\omega(\mathbf{r}),\rho(\mathbf{r}),q,\mathbf{r})w(\mathbf{r})\times \\ & \left(1-\left(1-x_{\tau 0}(q)\right)\exp\left(-\tau_d/T_1(\Delta\omega(\mathbf{r}),\mathbf{r})\right)\right)\times \\ & \exp\left(-t/T_2^*(\mathbf{r})\right)\cos\left(\omega_0(\mathbf{r})t+2\varphi_0^{Tx}(\rho(\mathbf{r}),\mathbf{r})\right)dV \end{aligned} \quad , \qquad [4.5]$$

where $x_{\tau 0}(q)$ is a shift caused by non-ideal measuring conditions.

Note that $T_1(\Delta\omega(\mathbf{r}),\mathbf{r})$ is an estimate of $T_1(\mathbf{r})$ which depends on measuring conditions and, in particular, on the frequency offset $\Delta\omega(\mathbf{r})$. Indeed, when the second pulse $\Delta\omega \neq 0$ is applied, not along the *x* axis, as it should be (Figure 2.18), but in the direction that depends on the component $\Delta\omega\times\tau_d$, rotations of the nuclear magnetization may not correspond to the specified measuring scheme. In this case the measurements and processing scheme will require a more sophisticated mathematical model based on a large number of delays τ_d, as discussed in [WAL 11]. The influence of the frequency offset on the accuracy of the T_1 estimate is more pronounced when measuring long relaxation times.

In order to measure the relaxation time T_2 it is necessary to use the SE measuring sequence (section 2.3.2). Assuming that two pulses are separated by a

time delay τ_d and that the second pulse has a pulse moment twice as large ($q_2 = 2q_1 = 2q$), the imaging equation can be written as

$$e_{2\tau_d}(q,\tau_d,t) = \int_V \omega_0(\mathbf{r})\beta_\perp(\rho(\mathbf{r}),\mathbf{r})M_\perp^{SE}(\Delta\omega(\mathbf{r}),\rho(\mathbf{r}),q,\mathbf{r})w(\mathbf{r})\times$$
$$\exp\left(-2\tau_d\left(\frac{1}{T_2(\mathbf{r})}+\frac{D(\mathbf{r})\gamma^2 G^2(\mathbf{r})\tau_d^2}{3}\right)\right)\times \quad , \qquad [4.6]$$
$$\exp\left(-\frac{(t-2\tau_d)^2}{2\times\left(T_2^*(\mathbf{r})\right)^2}\right)\cos\left(\omega_0(\mathbf{r})t+2\varphi_0^{Tx}(\rho(\mathbf{r}),\mathbf{r})\right)dV$$

where $M_\perp^{SE}$ is calculated using equation [2.31].

When using SE measurements or field setup with separated Tx and Rx loops, the only difference is that the integral equation corresponding to the data set must be used.

Thus, one can see that even when using the simplest measuring procedures the SNMR inverse problem is nonlinear. Resolving a nonlinear inverse problem is always more complicated than resolving a linear inverse problem and, as such, it is necessary to explore how the SNMR inverse problem can be linearized.

4.2. Linearization

A straightforward approach for linearizing the SNMR inverse problem (equations [4.4] – [4.6]) consists of fixing $\Delta\omega(\mathbf{r})$ and $\rho(\mathbf{r})$. For that, we must prescribe for the entire volume $\Delta\omega = 0$, meaning that measurements are conducted under close-to-resonance conditions. This assumption is often justified when rocks are non-magnetic. Small variations of the frequency offset within +/- 0.5 Hz have only a small effect on the SNMR signal and can usually be ignored (especially for short relaxation times). The Larmor frequency can be derived from measurements of the Earth's magnetic field using a proton magnetometer. We also assume that the resistivity of the subsurface $\rho(\mathbf{r})$ is known. It can be measured using one of the

electrical or electromagnetic methods. The most convenient will be the Time Domain EM method (TDEM) because the same transmitting loop could be used for SNMR and TDEM.

Historically, SNMR was developed for signals measured and processed in a time domain mode – we also will use signals presented in a time domain. The use of a synchronous detector allows us to consider the envelope of the SNMR signal individually [LEG 98b], thus simplifying equations [4.4] – [4.6]. For example, equation [4.4] will be simplified to

$$e(q,t) = \omega_0 \int_V \beta_\perp(\mathbf{r}) e^{j2\varphi_0^{Tx}(\mathbf{r})} M_\perp(q,\mathbf{r}) w(\mathbf{r}) \exp\left(-t/T_2^*(\mathbf{r})\right) dV \,, \qquad [4.7]$$

where $e(q,t)$ is an experimental data set and $w(\mathbf{r})$, $T_2^*(\mathbf{r})$ represent a model of the subsurface.

In equation [4.7] both parameters of interest, $w(\mathbf{r})$ and $T_2^*(\mathbf{r})$, are independent of time and, hence, for each moment of time t_i, equation [4.7] can be written as

$$e(q,t_i) = \omega_0 \int_V \beta_\perp(\mathbf{r}) e^{j2\varphi_0^{Tx}(\mathbf{r})} M_\perp(q,\mathbf{r}) w_T(\mathbf{r},t_i) dV \,, \qquad [4.8]$$

where $w_T(\mathbf{r},t_i) = w(\mathbf{r}) \exp\left(-t_i/T_2^*(\mathbf{r})\right)$.

Inversion of the data set composed of measurements of the signal at moments of time t_i, provides a function $w_T(\mathbf{r},t)$, exponentially decaying with the time constant $T_2^*(\mathbf{r})$. Note that $T_2^*(\mathbf{r})$ may be composed of more than one value of the relaxation time $T_2^*(\mathbf{r}) = \sum_K T_{2k}^*$, thus enabling us to obtain T_2^* distribution corresponding to point $\mathbf{r}$ of the subsurface.

A similar procedure can be applied to equations [4.5] and [4.6] corresponding to measurements of T_1 and T_2 relaxation times and the SNMR inverse problem becomes linear. Inversion of equation [4.7] can be built using two different approaches.

The first way proposed in [LEG 02a; MOH 02; MOH 05] (Time Step Inversion, TSI) consists of making independent inversions of the data sets corresponding to the time steps t_i, but assuming the smoothness of the solution $w_T(\mathbf{r},t)$ in the time domain by adding a penalty $\alpha_T \sum \left((w_{t_{i-1}} - w_{t_i})^2 + (w_{t_{1+i}} - w_{t_i})^2 \right)$ to the minimization function. The smoothness assumption makes a link between inversions corresponding to different moments of time. The solution $w_T(\mathbf{r},t)$ is fitted by a multi-exponential function $w_T(\mathbf{r},t) = \sum_K w_k(\mathbf{r}) \exp\left(-t / T^*_{2k}(\mathbf{r})\right)$ thus providing T^*_2 distribution.

The second procedure called QT inversion was proposed in [MÜL 10]. This algorithm allows for a global optimization of measured time series. In order to achieve this, equation [4.7] is discretized in space ($\mathbf{r}$) and in relaxation time T^*_2 domains, and is represented by one matrix for inversion. The full data set is represented by the time records of the SNMR signal. Inversion of this matrix provides T^*_2 distribution.

Both of these inversion approaches are used in practice and provide comparable results. The main difference between them lies in the inversion design. The QT algorithm supposes one inversion of a large matrix and the TSI inversion is accomplished by many inversions of a much smaller matrix. For example, let us suppose that the data set is composed of 10 pulse moments with 50 time readings for each pulse moment. If the subsurface is represented by 10 model layers and T^*_2 is decomposed into 10 different exponents then the dimension of matrix **A** (*M* rows and *N* columns) for QT inversion will be (*M*=10×50 and *N*=10×10) *M*×*N*=500×100. The same data set could be inverted using the TSI approach performing 50 inversions of matrix **A***M*×*N*=*10*×*10* and 10 additional inversions of a matrix

$M \times N = 50 \times 10$ for T_2^* decomposition. The difference between the size of the matrix increases for large data sets (2-D and 3-D inversion) and when using complex signals.

4.3. Discretization

The TSI approach involves the inversion of time-separated measurements using the same matrix – thus, analysis of such a matrix is of particular importance for the SNMR inverse problem.

4.3.1. *The 1-D inverse problem*

Let us first consider the 1-D linear inverse problem. Assuming $t = 0$ in equation [4.8] we obtain a linear integral equation

$$e_0(q) = \omega_0 \int_V \beta_\perp(\mathbf{r}) e^{j2\varphi_0^{Tx}(\mathbf{r})} M_\perp(q,\mathbf{r}) w(\mathbf{r}) dV \,. \qquad [4.9]$$

If $\varphi_0 = 0$ then the SNMR signal is real and inversion can be performed using amplitudes alone, otherwise inversion should be carried out considering complex SNMR signals. Assuming that the stratification is horizontal, equation [4.9] can be written as a Fredholm integral equation of the first kind

$$e_0(q) = \int_0^{z_{\max}} K_{1D}(q,z) w(z) dz \,, \qquad [4.10]$$

where $K_{1D}(q,z)$ is a one-dimensional kernel

$$K_{1D}(q,z) = \omega_0 \int_{x,y} \beta_\perp(\mathbf{r}) e^{j2\varphi_0^{Tx}(\mathbf{r})} M_\perp(q,\mathbf{r}) dx dy \,. \qquad [4.11]$$

Numerical results show that distant protons produce a negligibly small signal and, hence, integration can be limited by the area of approximately $x^2 + y^2 < (3a)^2$, and $z_{\max} \approx 1.5a$ can be considered as an estimate of the maximum possible depth of water detection, where a is the side for a square loop.

Let I_q be the number of pulse moments and I the number of data readings. When using only amplitudes we will have $I = I_q$, and when using complex signals we will have $I = 2I_q$. Let J be the number model layers representing the subsurface. In this case the integral equation [4.10] can be approximated by a system of algebraic equations. In a matrix notation the approximating equation can be written as

$$\mathbf{Aw} = \mathbf{e_0}, \qquad [4.12]$$

where $\mathbf{A} = \left[a_{i,j} \right]$ is a rectangular matrix of $I \times J$ with the elements

$$a_{i,j} = \begin{cases} \mathrm{Re}\left(\int_{z_j}^{z_{j+1}} K_{1D}(q_i, z)dz \right), & for \quad i <= I_q \\ \mathrm{Im}\left(\int_{z_j}^{z_{j+1}} K_{1D}(q_{i-I_q}, z)dz \right), & for \quad i > I_q \end{cases}, \qquad [4.13]$$

$\mathbf{e_0} = (e_{01}, e_{02}, .., e_{0i}, .., e_{0I})^T$, $e_{0i} = e_0(q_i)$ being the set of experimental data, $\mathbf{w} = (w_1, w_2, .., w_j, .., w_J)^T$, $w_j = w(\Delta z_j)$ being the vertical distribution of water content and the symbol T denoting transposition.

For discretizing equation [4.10], we define a set of pulse moments q_i for measuring SNMR signal $e_{0i} = e_0(q_i)$ with $i = 1,2,..,I$ (data set **d**), and a set of cells Δz_j that approximate the subsurface with $j = 1,2,..,J$ (model of the subsurface **m**). In the 1-D case, each cell is a horizontal layer of the thickness $\Delta z_j = z_{j+1} - z_j$ (Figure 1.11a) selected so that $z_j < z_{j+1}$ and $z_{\max} = \sum_{j=1}^{J} \Delta z_j$. For the selection process we can use the results from forward modeling presented in Chapter 3. For example, Figure 3.10 shows that a water saturated layer located at depth z_j has the maximum of the signal $e_{\max j}$ for the particular value of the pulse moment $q_{z_j}^{\max}$. Thus, when the set of layers Δz_j is defined we may assume that number of measuring points is equal to the number of layers ($I = J$) and a set of pulse moments for measuring could be defined as $q_i = q_{z_j}^{\max}$. Thus, the discretization of the data set (selection of the pulse moments for measuring and inversion) depends on the discretization of the model (selection of the model layers).

The numerical solution to equation [4.12] is highly dependent on the discretization of the integral equation. For a unique and stable solution, the columns of matrix **A** must be linearly independent. To establish a rule for discretization we can use the estimate of the linear dependence between the columns given by the covariance between the columns of matrix **A**

$$Cov(col(j), col(k)) = \sum_{i=1}^{I} (a_{i,j} \times a_{i,k}) . \qquad [4.14]$$

In matrix notation, the covariance matrix of matrix **A** can be calculated as $\mathbf{A}^{\mathbf{T}}\mathbf{A}$, where the symbol T denotes transposition. However, it may be more convenient to use Pearson's correlation coefficient, which is the covariance between two vectors normalized by their variances

$$r_{j,k} = \frac{Cov(col(j), col(k))}{\sqrt{Var(col(j))Var(col(k))}} , \qquad [4.15]$$

where $Var(col(j)) = \sum_{i=1}^{I} a_{i,j}^2$ and $Var(col(k)) = \sum_{i=1}^{I} a_{i,k}^2$. Thus, the correlation coefficient between columns j and k of matrix $\mathbf{A}$ can be calculated as

$$r_{j,k} = \frac{\sum_{i=1}^{I} (a_{i,j} \times a_{i,k})}{\sqrt{\sum_{i=1}^{I} a_{i,j}^2 \times \sum_{i=1}^{I} a_{i,k}^2}}. \qquad [4.16]$$

The Pearson correlation varies between 1 and −1 and for linearly independent columns it will be equal to zero. The correlation matrix **R** is composed of Pearson's correlation coefficients between columns of matrix **A** and can be calculated as

$$\mathbf{R} = \mathbf{D}\mathbf{A}^{\mathbf{T}}\mathbf{A}\mathbf{D}, \qquad [4.17]$$

where **R** is a matrix of $J \times J$ and **D** is the diagonal matrix with the elements

$$d_{j,j} = \frac{1}{\sqrt{\sum_{i=1}^{I} a_{i,j}^2}}. \qquad [4.18]$$

It has been shown that the correlation matrix can be used for the discretization of the SNMR integral equation [LEG 98a]. For that, one can prescribe the thickness of the model layers representing the subsurface to increase with depth $\Delta z_j \leq \Delta z_{j+1}$ (Figure 1.11a). In this case, layers located at the neighboring depths are more linearly dependent than layers located at distinctly different depths. Thus, we can discretize the SNMR integral equation using a discretization rule based on the correlation coefficient between the neighboring layers $r = r_{j,j+1} = r_{j+1,j+2} = ... = r_{J-1,J}$. A selection of the number of layers J and of the thickness of the model layers Δz_j (discretization of the model) allows us to select the values of the pulse moment for measuring by assuming $I = J$ and $q_i = q_{z_j}^{\max}$ (discretization of the data).

Figure 4.1 shows an example of the discretization made for a 80×80 m^2 square loop. We consider the maximum pulse moment of 12,000 A-ms and 40 model layers (I=J=40). Instead of calculating correlation coefficients one can use Δz_j increasing according to a logarithmical law and assuming the minimal thickness Δz_1 and the maximal depth z_{max}.

The following examples show the correlation matrix **R** calculated for different sounding configurations.

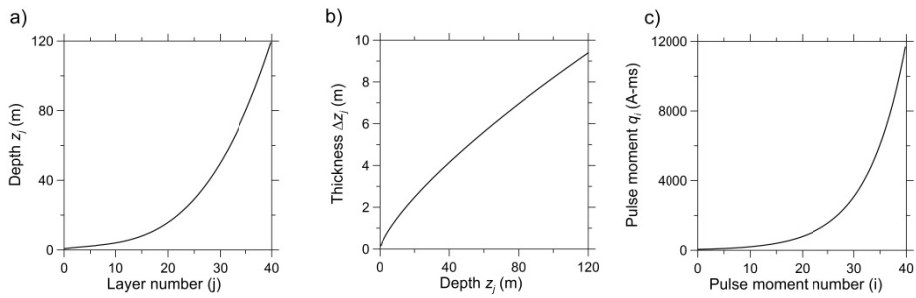

Figure 4.1. *Example of discretization of matrix **A** made for a sounding with 80-m-side square loop and the maximum pulse moment of 12,000 A-ms (I=J=40): a) correspondence between the depth and the number of model layers; b) thickness of the model layer versus its depth; c) corresponding pulse moments*

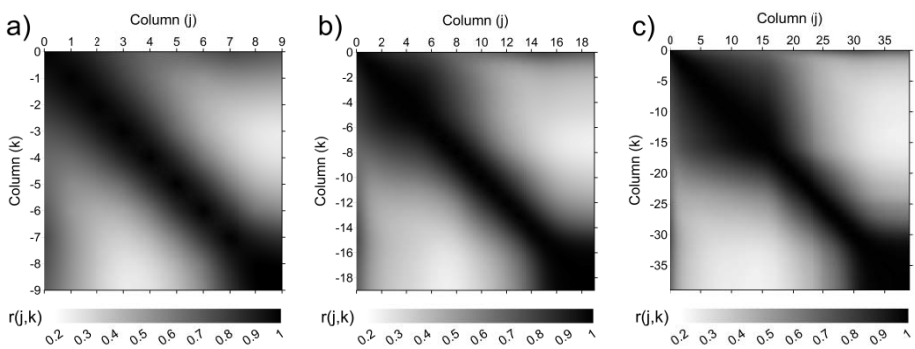

Figure 4.2. *Correlation matrix **R** calculated for matrix **A** (amplitudes) assuming a 100 ohm-m half space and the number of columns of matrix **A**: a) J=10; b) J=20; c) J=40*

Figure 4.2 shows the correlation coefficients between the columns of matrix **A** calculated considering the amplitudes of the SNMR signal. It is clear that the correlation between neighboring layers is the strongest and that the correlation between layers located at different depths decreases. This general tendency is independent of the number of layers and demonstrates the capacity of the method to resolve water at depth.

The correlation of matrix **R** calculated considering the half space of different resistivity is presented in Figure 4.3.

For all three examples we assumed 40 model layers (I=J=40). For calculating we use only amplitudes of the SNMR signal. Results show that when the subsurface is electrically conductive, the linear dependence between the model layers is slightly diminished, thus suggesting that we could expect a slightly better resolution for inversion.

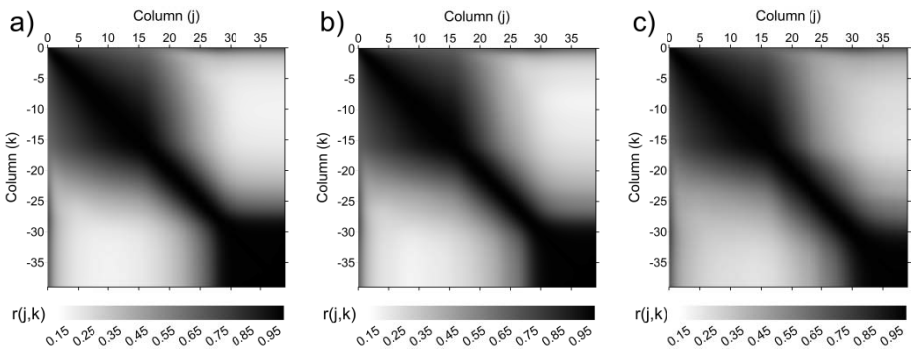

Figure 4.3. *Correlation matrix **R** calculated for matrix **A** (amplitudes, J=40) assuming the half space of: a) 5 ohm-m; b) 10 ohm-m; c) 100 ohm-m*

Figure 4.4 shows correlations calculated considering complex signals (amplitude and phase). The smaller correlation between neighboring layers can be easily explained by a pronounced phase shift of the SNMR signal caused by the electrically conductive subsurface.

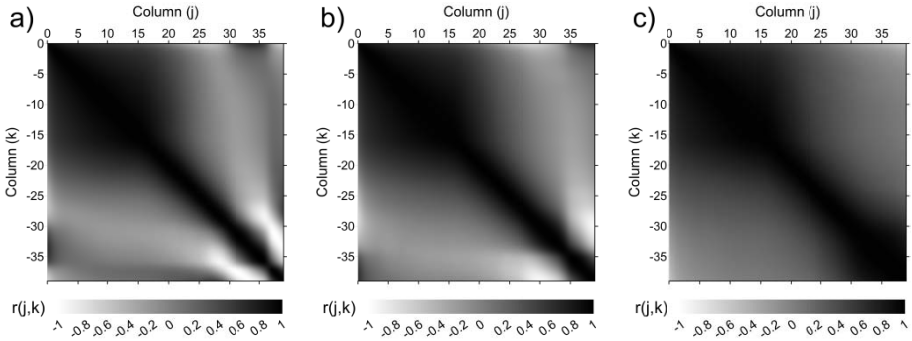

Figure 4.4. *Correlation matrix **R** calculated for matrix **A** (complex signals, J=40) assuming a half space of: a) 5 ohm-m; b) 10 ohm-m; c) 100 ohm-m*

Matrix **R** is calculated using the amplitudes and the complex signals for the five ohm-m half space was plotted on the same gray scale and these examples are shown in Figure 4.5.

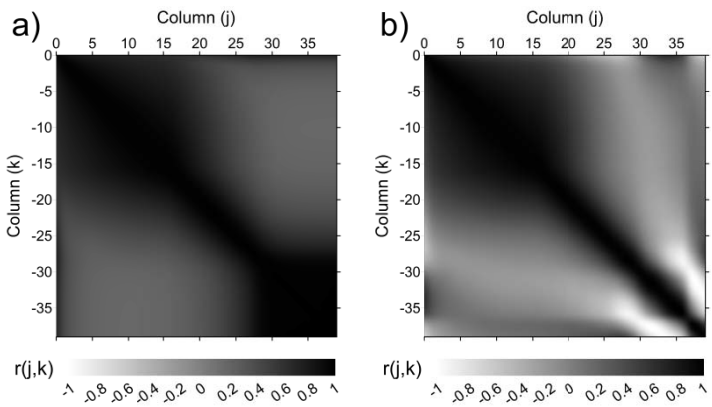

Figure 4.5. *Correlation matrix **R** calculated for matrix **A** (5 ohm-m, J=40): a) using amplitudes; b) using complex signals*

However, even though the correlation matrix is a useful tool for representing linear dependencies between columns of matrix **A**, it does not allow for a quantitative estimate of the resolution of the inverse problem. The method of particular interest when analyzing the least squares problems is the singular value decomposition, or SVD [AST 05]. In the SVD matrix I by J **A** is factored into

$$\mathbf{A} = \mathbf{USV}^T, \qquad [4.19]$$

where $\mathbf{U}$ is an $I \times I$ orthogonal matrix with columns that are unit basis vectors spanning the data space, $\mathbf{V}$ is a $J \times J$ orthogonal matrix with columns that are unit basis vectors spanning the model space and $\mathbf{S}$ is an $I \times J$ diagonal matrix with non-negative diagonal elements called singular values.

The singular values of $\mathbf{S}$ are customarily arranged in decreasing magnitude $s_1 \geq s_2, .., s_{\min(I,J)} \geq 0$. The first p values are non-zero and others may be zero or close to zero. Small singular values can be considered insignificant because they represent numerical instabilities and do not correspond to the physical meaning of the inverse problem. So, we can consider only significant singular values and partition $\mathbf{S}$ as

$$\mathbf{S} = \begin{bmatrix} \mathbf{S}_p & \mathbf{0} \\ \mathbf{0} & \mathbf{0} \end{bmatrix}, \qquad [4.20]$$

where $\mathbf{S}_p$ is a $p \times p$ diagonal matrix composed of the positive singular values. Thus, we can write a reduced rank approximation (or truncated SVD) as

$$\mathbf{A} = \mathbf{U}_p \mathbf{S}_p \mathbf{V}_p^T. \qquad [4.21]$$

The columns of matrix $\mathbf{U}_p$ are linearly independent and they form an orthonormal basis for the data space. The columns of matrix $\mathbf{V}_p$ form an orthonormal basis for the model space.

The SVD can be used to calculate a generalized inverse called the Moore-Penrose pseudoinverse [MOO 20] and [PEN 55]. The generalized inverse of matrix $\mathbf{A}$ is

$$\mathbf{G}^g = \mathbf{V}_p \mathbf{S}_p^{-1} \mathbf{U}_p^T. \qquad [4.22]$$

Thus we define the pseudoinverse solution of equation [4.12] to be

$$\mathbf{w} = \mathbf{G}^g \mathbf{e}_{\mathbf{0}} = \mathbf{V}_p \mathbf{S}_p^{-1} \mathbf{U}_p^T \mathbf{e}_{\mathbf{0}}. \qquad [4.23]$$

The generalized inverse provides an inverse solution that always exists and that it is both a least squares and a minimum length solution. For estimating the uncertainty of the pseudoinverse solution caused by experimental noise, we assume independent and identically distributed normal data errors σ^2. In this case the data covariance matrix is simply σ^2, and the covariance for the model becomes

$$Cov(\mathbf{w}_{L_2}) = \sigma^2 \mathbf{V}_p \mathbf{S}_p^{-2} \mathbf{V}_p^T. \qquad [4.24]$$

We can calculate intervals $\mathbf{w}_{L_2}$ with 95% confidence, taking into account that each model parameter has a normal distribution with a mean given by the solution

$$\mathbf{w} = \mathbf{w}_{L_2} \pm \mathbf{w}_{0.95}, \qquad [4.25]$$

where

$$\mathbf{w}_{0.95} = 1.96 \times \sqrt{diag\left(Cov(\mathbf{w}_{L_2})\right)}, \qquad [4.26]$$

and the 1.96 factor arises from the assumption of the 95% confidence intervals

$$\frac{1}{\sigma\sqrt{2\pi}} \int_{-1.96\sigma}^{1.96\sigma} \exp(-\frac{x^2}{2\sigma^2}) dx \approx 0.95. \qquad [4.27]$$

Note that even if the data are known to be without error, inversion may not have the perfect resolution. The resolution can be estimated using the model resolution matrix $\mathbf{R}_m$ given by the generalized inverse. $\mathbf{R}_m$ is a symmetric matrix describing how the solution smears out the original model into a recovered model. It can be calculated as

$$\mathbf{R}_m = \mathbf{V}_p \mathbf{V}_p^T. \qquad [4.28]$$

Let $\mathbf{I}$ be a diagonal matrix with non-diagonal elements as zeros and the diagonal elements being 1 (the identity matrix). If $rank\,(\mathrm{A}) = p = J$ then $\mathbf{R}_m = \mathbf{I}$ and the model will be perfectly recovered by the inversion. If $p < J$ then $\mathbf{R}_m$ is not the identity matrix and the resolution is not perfect. A simple estimate of the resolution can be made by calculating the trace of the model resolution matrix $Tr(\mathbf{R}_m)$. If $Tr(\mathbf{R}_m) \to J$ then $\mathbf{R}_m \to \mathbf{I}$. Otherwise the idea of how much bias has been introduced by the inverse solution can be estimated by calculating

$$\left\| \mathbf{R}_m - \mathbf{I} \right\|. \qquad [4.29]$$

The data space resolution matrix allows estimating how good data can be fitted by the generalized inverse

$$\mathbf{R}_d = \mathbf{U}_p \mathbf{U}_p^T. \qquad [4.30]$$

If $\mathbf{R}_d = \mathbf{I}$ then the data fit perfectly after inversion results. It is important to underline that the model and data space resolution matrices do not depend on specific data or models, but they are exclusively properties of matrix **A**.

The generalized inverse given by equation [4.22] may become unstable due to the possibility of very small singular values. The instability created by very small singular values can be estimated using the condition number defined as

$$cond(\mathbf{A}) = s_1 / s_p, \qquad [4.31]$$

where s_1 and s_p are the largest and the smallest singular values respectively. Assuming $\left\| \boldsymbol{\varepsilon}_m \right\|_2$ to be the relative error for model and $\left\| \boldsymbol{\varepsilon}_d \right\|_2$ for data we can estimate the error amplification as

$$\left\| \boldsymbol{\varepsilon}_m \right\|_{L2} \le cond(\mathbf{A}) \times \left\| \boldsymbol{\varepsilon}_d \right\|_{L2}. \qquad [4.32]$$

Thus, decreasing p one can render the solution more stable. However this stability reduces the model space and as a result, the model resolution matrix becomes less like the identity matrix.

Now, let us apply the SVD analysis to the discretization of the SNMR integral equation. We use the calculated parameters presented by matrix **A**, as presented in Table 4.1 (model 2). As the criterion for truncating (selecting p) we use the diagonal elements of the model resolution matrix $\mathbf{R}_m$ (equation [4.28]). We fix the minimal thickness $\Delta z_1 = 0.5$ m and the maximal depth $z_{\max} = 120$ m, but assume the fixed number of the pulse moment for measuring (I=40). The number of model layers was defined from SVD decomposition so that the diagonal elements of matrix $\mathbf{R}_m$ rest close to 1. For analysis we used both amplitudes and complex signals for the 100 ohm-m half space and only complex signals for the 5 ohm-m half space. The use of the amplitudes for inversion in the presence of electrically conductive rocks may lead to additional errors because of a strong phase shift in the SNMR signal. The summary of the parameters of matrix **A** are presented in Table 4.1.

Matrix A	***Number of rows I***	***Number of columns J***	***Rank p***	***Cond(A)***	***Zmax (m)***
100 ohm-m (amplitudes)	16	14	11	116	58
100 ohm-m (complex)	16	17	15	389	82
5 ohm-m (complex)	16	19	15	135	59

Table 4.1. *Parameters of matrix **A** used for SVD analysis of the 1-DSNMR inverse problem*

Figure 4.6a shows the diagonal elements of the model resolution matrix $\mathbf{R}_m$. Selection of a larger number of model layers (J) and/or of a larger rank of matrix **A** (p) cause increased instability of SVD decomposition.

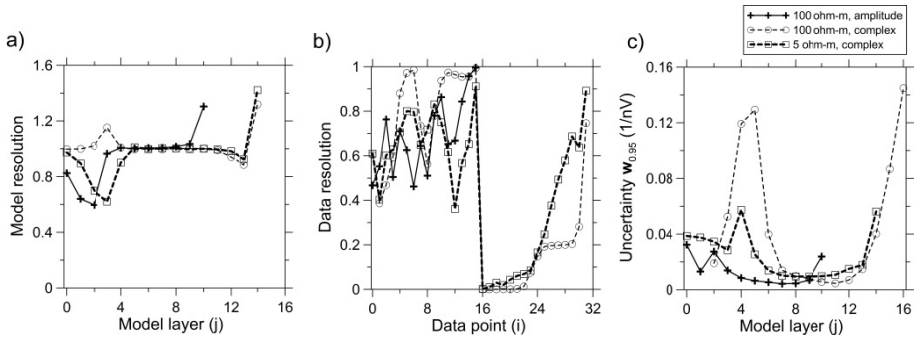

Figure 4.6. *SVD optimized inversion parameters for matrix **A** calculated considering the half space of 5 and 100 ohm-m: a) model resolution estimate for each model layer; b) data resolution estimate for each data point; c) the 95% confidence intervals*

The diagonal elements of data resolution matrix $\mathbf{R}_d$ (equation 4.30) are presented in Figure 4.6b. Data points (*i*) from 0 to 15 represent the real part of the SNMR signal and from 16 to 31 the imaginary part. The phase shift for shallow depths is not significant and consequently the imaginary part of the signal is small. It explains the low resolution of these data points observed in Figure 4.6b. The 95% confidence interval is shown in Figure 4.6c. One can see that even with very low noise (1 nV) we can expect up to +/-14% uncertainty in the inversion results. We explain this large uncertainty by the effect of error amplification (equation [4.32]). Figures 4.7–4.9 show that in these cases the model and the data resolution matrices exhibit domination of the diagonal elements thus confirming a good resolution.

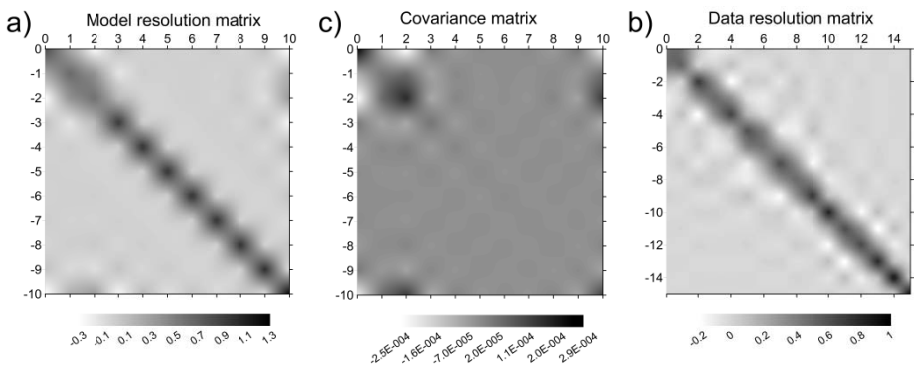

Figure 4.7. *SVD estimates of matrix **A** for inversion of amplitudes considering the 100 ohm-m half space: a) model resolution matrix; b) data resolution matrix; c) covariance matrix for estimated model parameters*

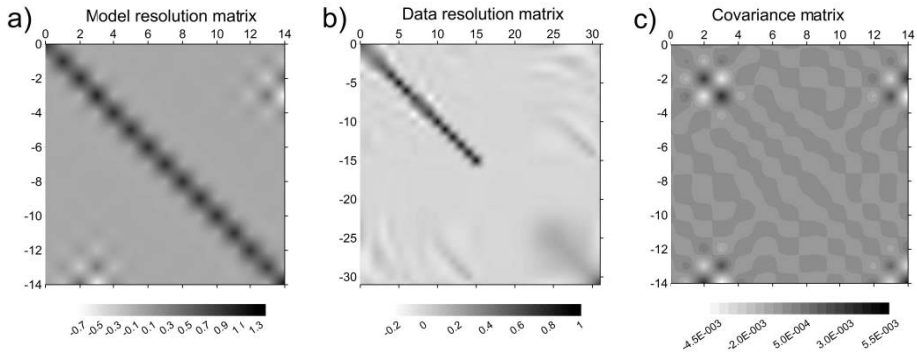

Figure 4.8. *SVD estimates of matrix **A** for inversion of complex signals considering the 100 ohm-m half space: a) model resolution matrix; b) data resolution matrix; c) covariance matrix for estimated model parameters*

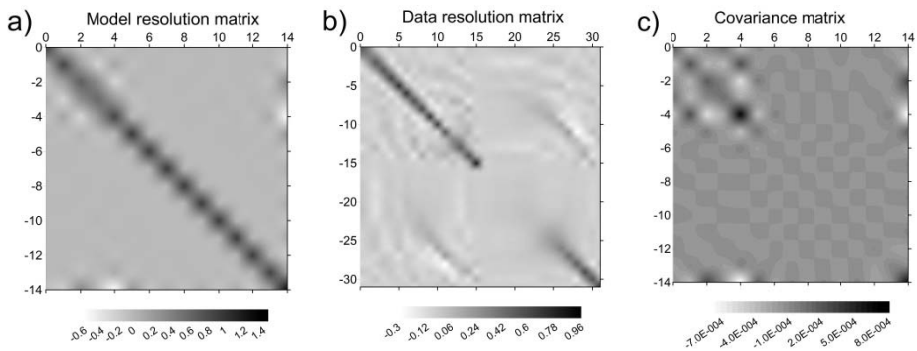

Figure 4.9. *SVD estimates of matrix **A** for inversion of complex signals considering the 5 ohm-m half space: a) model resolution matrix; b) data resolution matrix; c) covariance matrix for estimated model parameters*

The covariance matrix shows small linear dependencies between the columns of matrix **A** which indicates a small smearing of the solution between the model layers. Note, that a larger number of model layers can be resolved by complex inversion thus confirming a better resolution of matrix **A** when complex signals are used.

We performed the spike test (100 ohm-m half space, complex data) which consisted of calculating a synthetic data set, assuming only one model layer to be equal to 1 and all the others to be equal to zero, and performing an inversion of these data. For this test we selected a layer with a very narrow confidence interval (j=7, see Figure 4.6) and a layer with higher uncertainty (j=15). As expected, the first layer (j=7) was well resolved with the root mean square error *RMSE*=1.5 nV. The second layer (j=15) was resolved, but with higher uncertainty and with a not so good

data fit (*RMSE*=11.2 nV). The results of the spike test for the second case are shown in Figure 4.10a. The data set and the inversion fit are shown in Figure 4.10b.

Finally, Figure 4.10c shows the thickness of the model layers versus their depth. These results confirm that the resolution of the SNMR inversion is better when complex signals are used. An electrically conductive subsurface also enables us to attain a better resolution. However, the screening effect in this case attenuates the signal, thus reducing the depth of investigation.

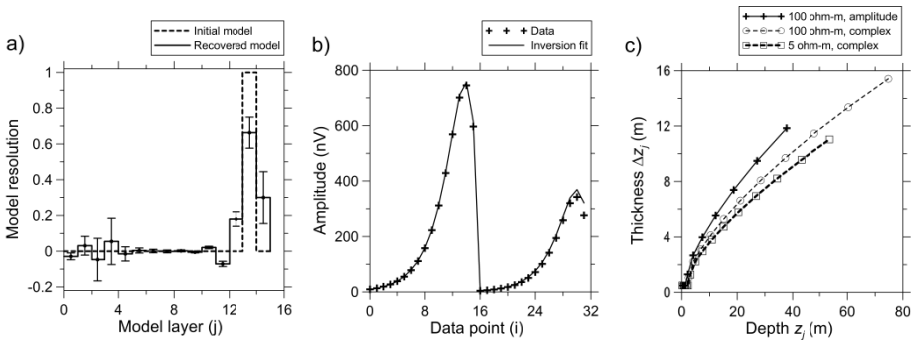

Figure 4.10. *Results of the spike test carried out for the 100 ohm-m half space and using the complex signal: a) initial model (dashed line) and the model recovered by inversion (95% confidence intervals have been calculated assuming a 1-nV-noise level); b) synthetic data set (crosses) and data calculated after inversion results (solid line), the misfit RMSE=11.2 nV. Thickness of the model layers versus its depth could be considered as an indicator of the vertical resolution of the inversion (c)*

4.3.2. *The 3-D inverse problem*

3-D inversion of SNMR data is a new development and we expect different improvements to be made in the future. Measuring procedure, field setup and discretization can be optimized taking into account target sizes and location. In this book we limit our analysis by the simplest realization of 3-D SNMR inversion aiming to provide a general idea about the resolution of the method.

Let us assume a 3-D SNMR measuring setup composed of L transmitting loops (*Tx*) and K receiving loops (*Rx*). Let I_l be a number of pulse moments for the corresponding *Tx* loop. In this case a number of data readings will be $I = 2 \times K \times L \times \sum_{l=1}^{L} I_l$, where the factor two appears when the complex signal is used. For discretizing the integral equation [4.10] we divide the subsurface in J cells as

shown in Figure 1.11c. So $J = J_x \times J_y \times J_z$, with J_x, J_y, J_z being the number of cells in each direction. Similar to the 1-D case, 3-D SNMR inversion requires the resolution of a matrix equation $\mathbf{Aw} = \mathbf{e_0}$. One of the possible ways to build matrix $\mathbf{A}$ and corresponding solution vector $\mathbf{w}$ and data set vector $\mathbf{e_0}$ is shown in Figure 4.11.

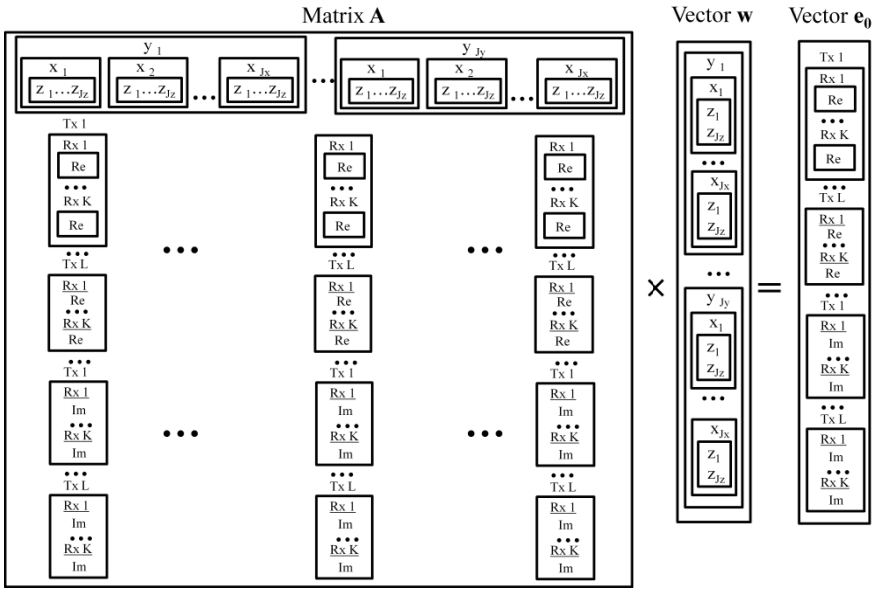

Figure 4.11. *Possible construction of matrix **A** for 3-D SNMR inversion*

Matrix $\mathbf{A} = \left[a_{i,j} \right]$ is with the elements f $I \times J$ with the elements

$$a_{i,j} = \begin{cases} \mathrm{Re}\left(\omega_0 \int_{V_j} \beta_\perp(\mathbf{r}) e^{j2\varphi_0^{Tx}(\mathbf{r})} M_\perp\left(q_i, \mathbf{r}\right) dV \right), & for \quad i <= \sum_{l=1}^{L} I_l \\ \mathrm{Im}\left(\omega_0 \int_{V_j} \beta_\perp(\mathbf{r}) e^{j2\varphi_0^{Tx}(\mathbf{r})} M_\perp\left(q_{i-\sum_{l=1}^{L} I_l}, \mathbf{r}\right) dV \right), & for \quad i > \sum_{l=1}^{L} I_l \end{cases} \qquad [4.33]$$

Thus, the subsurface is represented by cells of a volume V_j and each element $a_{i,j}$ contains an SNMR signal calculated for the corresponding cell using equation [4.33]. Depending on the selected inversion scheme cells may contain only amplitudes or real and imaginary parts of the complex signal.

Discretization can be carried out using the same principle as for 1-D inversion based on the correlation coefficient between signals generated by neighboring cells. In a general case, an SNMR measuring setup may be composed of many separated *Tx* and *Rx* loops. It has been reported that using many *Rx* loops allows for improvements to the resolution of inversion for shallow parts of the subsurface [HER 07; LEH 11b]. The use of the coincident loops may be justified when transportation expenses are significant and when there is no possibility of keeping the loops in the field for a few days. For simplifying our presentation we presume a 3-D setup composed of nine coincident *Tx/Rx* loops of 80×80 m^2 (Figure 4.12).

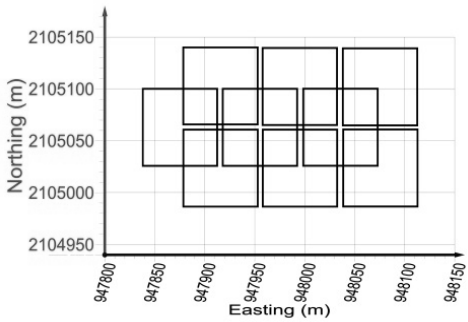

Figure 4.12. *3-D SNMR setup composed of nine overlapped square loops of 80-m-side*

For investigating possible 3-D SNMR inversion resolution we only use complex signals and assume 40 pulse moments per loop. We discretize the subsurface by cells of equal size (40×40×10 m^3 and 20×20×5 m^3) and we use the same SVD based approach as we used for the 1-D inverse problem.

First, we will estimate the minimum cell size that could be resolved. For that we calculate the amplitude of the SNMR signal generated by the cells (Figure 4.13). The maximum amplitude was calculated assuming 100% of water in each cell. One can see that 20×20×5 m^3 cells generate signals about five times smaller than 40×40×10 m^3 cells and hence selecting smaller than 20×20×5 m^3 cells may not be reasonable because of the impossibility to accurately measure such small signals.

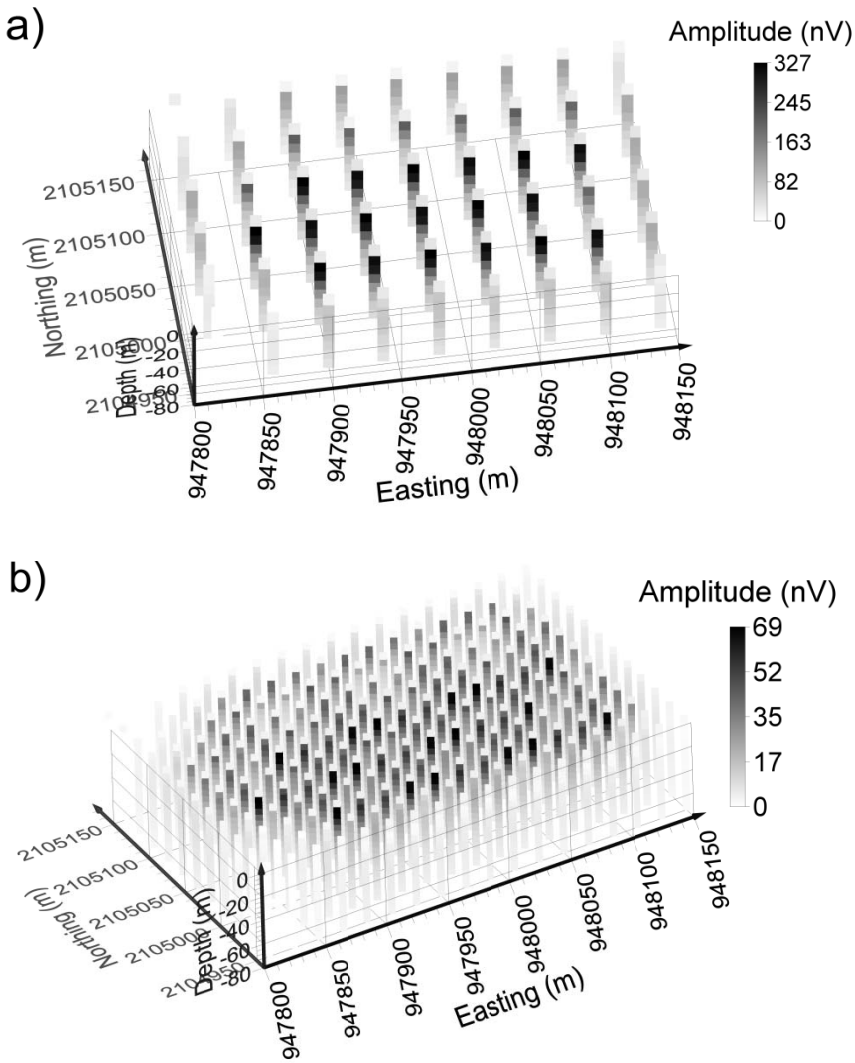

Figure 4.13. *The maximum amplitude of the magnetic resonance signal generated by each cell considering the 3-D SNMR setup composed of nine loops assuming 100% water content in each cell: a) cells of 40×40×10 m^3; b) cells of 20×20×5 m^3*

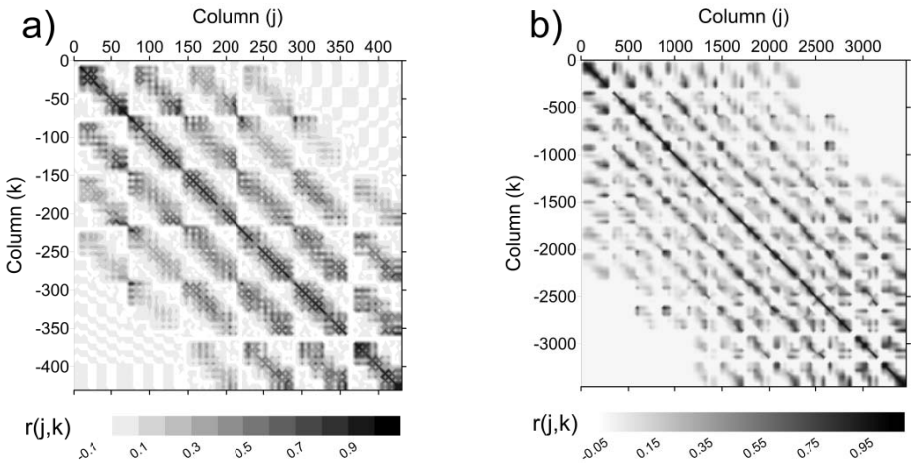

Figure 4.14. *Correlation matrix **R** calculated for matrix **A** composed of complex signals: a) cells of 40×40×10 m^3; b) cells of 20×20×5 m^3*

The correlation matrix **R** was calculated using equation [4.17] and considering 20×20×5 m^3 and 40×40×10 m^3 cells (Figure 4.14). The correlation coefficients show that only neighboring cells are linearly dependent, but the linear dependence between distant cells is smaller, thus suggesting that the properties of the 3-D SNMR inversion could be expected to be similar to the 1-D inversion.

In order to select the rank of SVD (p) we use the diagonal elements of the model resolution matrix $\mathbf{R}_m$ keeping them close to one. Setting larger rank p causes an increase in the diagonal elements corresponding to larger p and renders inversion unstable. Selected parameters of matrix **A** are summarized in Table 4.2.

Cells size (m^3)	***Number of rows I***	***Number of columns J***	***Rank p***	***Cond (A)***	***Resolved volume (m^3)***
20×20×5	720	3456	290	2611	580,000
40×40×10	720	432	167	4832	2,672,000

Table 4.2. *Parameters of matrix **A** used for SVD analysis of the 3-D SNMR inverse problem*

SVD estimated parameters of matrix **A** are presented in Figures 4.15 and 4.16. For both sizes of the model cell, the model resolution and the data resolution matrices show that the diagonal elements dominate and that their values are close to one. The covariance matrices show relatively small linear dependence between the signals generated by the model cells.

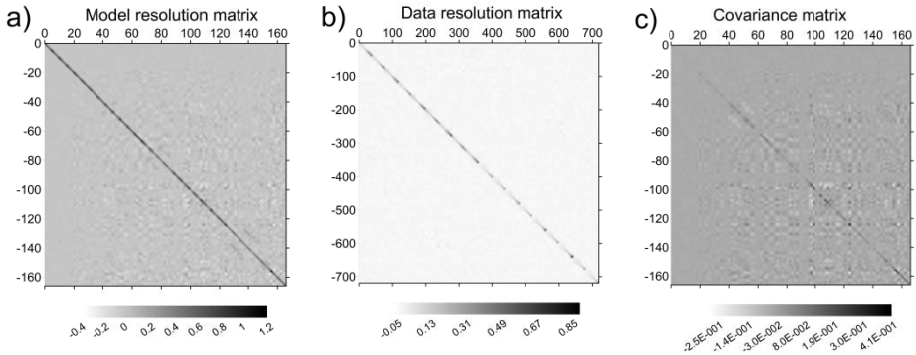

Figure 4.15. *SVD analysis of matrix **A** (complex signals) composed of 40×40×10 m^3 cells: a) model resolution matrix; b) data resolution matrix; c) covariance matrix for estimated model parameters*

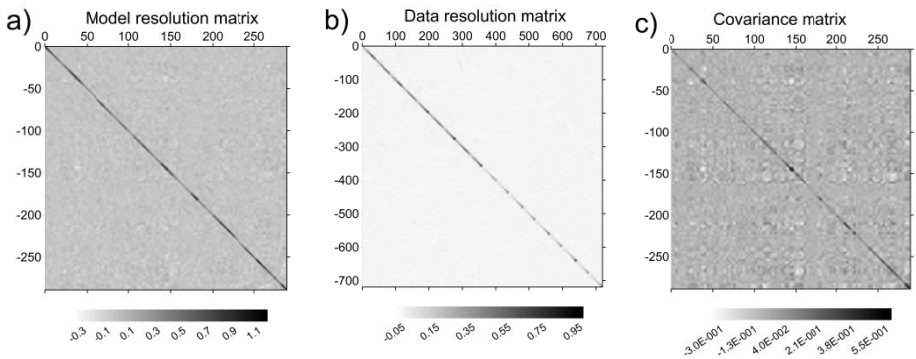

Figure 4.16. *SVD analysis of matrix **A** (complex signals) composed of 20×20×5m^{3}cells: a) model resolution matrix; b) data resolution matrix; c) covariance matrix for estimated model parameters*

3-D resolution plotting, taking into account cell positions, is displayed in Figure 4.17. It shows that when using 40×40×10 m^3 cells for discretization, inversion is able to resolve cells down to approximately 60 m. However, when using 20×20×5m^3 cells for discretization the resolution capacity is focalized in the shallow part and cells can be resolved down to approximately 20 m. These results are summarized in Table 4.2 showing that the volume where the resolution is reliable is much larger when matrix **A** is composed of 40×40×10 m^3 cells.

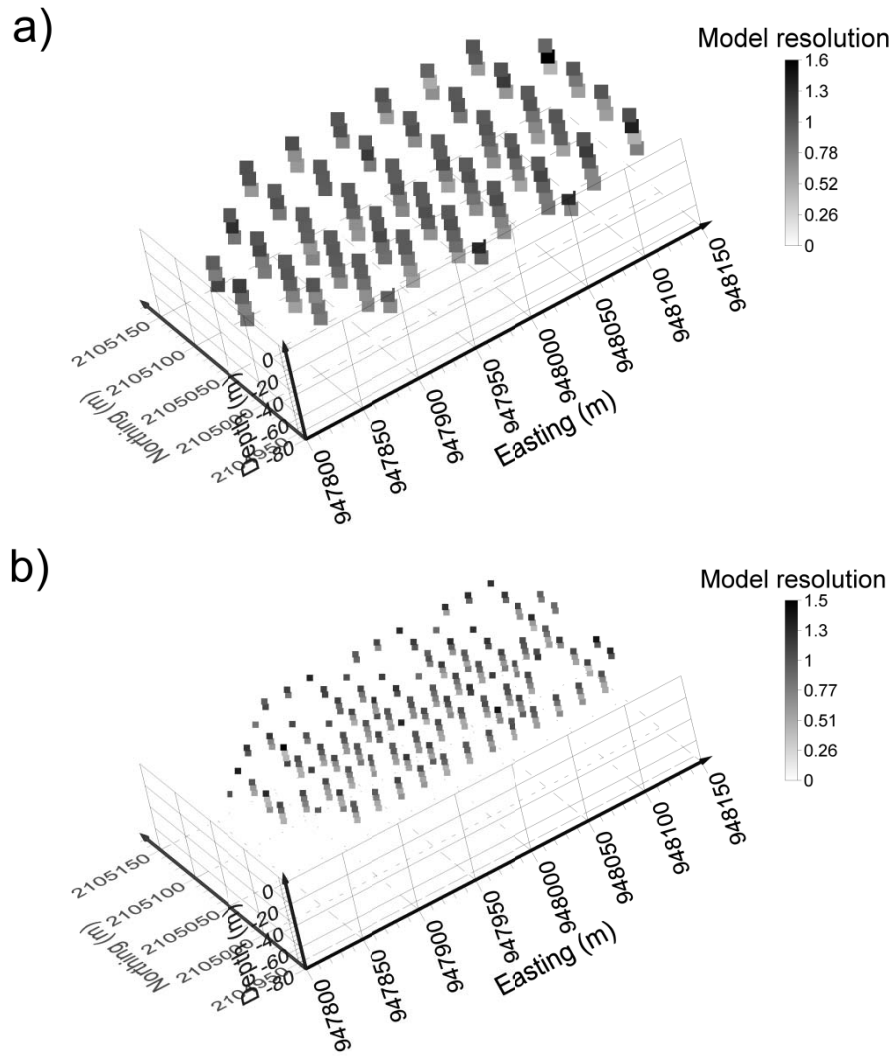

Figure 4.17. *SVD estimated 3-D resolution of SNMR inversion: a) 40×40×10 m^3 cells; b) 20×20×5 m^3 cells*

It would be instructive to plot the resolution and the uncertainty estimates together as shown in Figure 4.18. One can see that for very low noise (1 nV) matrix **A** composed of 40×40×10 m^3 cells shows relatively reliable resolution for approximately 100 cells. Matrix **A**, composed of 20×20×5 m^3 cells, has no cells

with such a resolution. The very high sensitivity of the 3-D SNMR inversion to noise is due to a high value of the condition number of matrix **A**. Indeed, for the 1-D inversion *cond* (**A**), presented in Table 4.1, was more than 100 times smaller than for the 3-D inversion (Table 4.2) and consequently the inversion was more stable.

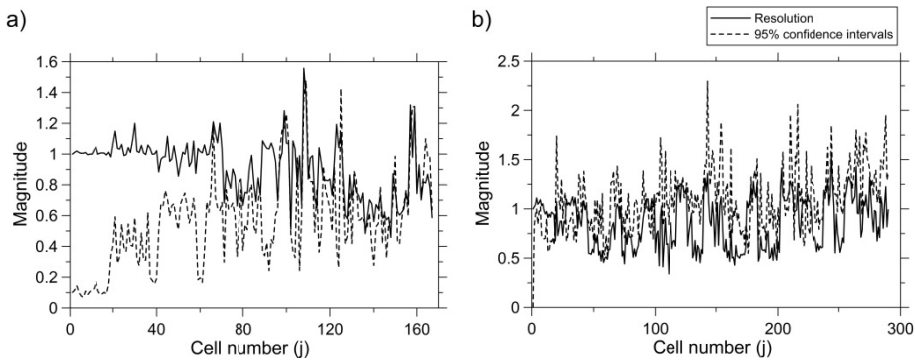

Figure 4.18. *SVD estimated resolution and 95% confidence intervals plotted versus the cell number of matrix **A** (complex signals) composed of: a) 40×40×10 m^3 cells; b) 20×20×5 m^3 cells. For this estimate we assume a1-nV-noise*

The results of the spike test under noiseless conditions show a rather good recuperation of the model when cells are well defined (SVD estimated resolution is close to one). For example, when using a matrix with 40×40×10 m^3 cells, the positions of the cell filled with water (the water content is equal to 1) with the SVD resolution estimated at 1.07 was correctly resolved. The recovered water content was 0.93 with the 95% confidence interval of +/-0.65. When using a matrix discretized with 20×20×5 m^3 cells, the position of the cells (resolution estimate of 0.97) was also correctly resolved. The water content in this cell was found equal to 0.86 instead of 1 with the 95% confidence interval of +/-0.66. However, it was not possible to correctly resolve cells with low SVD estimated resolution.

Thus, the resolution of the 3-D SNMR inverse problem estimated as the minimum size of cells used for the discretization of matrix **A** is limited by the magnetic resonance signals generated by one cell. Similar to the 1-D SNMR inverse problem, the resolution decreases with increasing depth. SVD analysis of the 3-D inversion, with nine coincident 80-m-side square loops suggests that in order for a 3-D target, located at the depth between 0 and 20 m, to be resolved, it should be larger than approximately 20×20×5 m^3. Below 20 m this target has to be larger than approximately 40×40×10 m^3. Targets deeper than approximately 60 m cannot be accurately resolved.

Thus, our analysis suggests that the SNMR inverse problem has inherently low resolution and is limited by the sensitivity of the method (the impossibility of accurately measuring small signals, less than a few nV) and by the properties of the integral equation. The resolution can be improved using specific optimizations of the measuring procedure and measuring setup, but significant improvements to the resolution, without using additional information for constraining inversion, seems impossible.

4.4. Linear inverse problems

It has been shown that the SNMR inverse problem can be linearized and resolved using linear least squares or minimum norm solutions. In this case, the uncertainty intervals can be estimated assuming Gaussian noise. The solution is the water content in the subsurface and physical meaning of the water content which allows a constraining inversion by the interval between 0 and 1. The inverse problem can still be considered as linear if an inversion is carried out using complex signals (when the phase shift takes place) or amplitudes (no phase shift). In practice, accurate measuring and modeling of the phase shift is not always possible and the use of complex signals may cause biased results in inversion. A solution was found which consisted of using complex signals in matrix **A**, and minimizing the only discrepancy between measured and calculated amplitudes. In this case the inverse problem is not linear, and for estimating inversion resolution one can assume that the resolution may be similar to the resolution estimated for linear inversion and assumption of Gaussian noise. Otherwise the uncertainty in the inversion results can be estimated with, for example, a Monte Carlo based approach. The Monte Carlo method is time consuming and is not very popular in geophysics. However, there are reports that it has been applied to the inversion of SNMR data with success [GUI 02b] and [MOH 02]. The Monte Carlo inversion of a 1-D data set is actually quite fast and can be easily realized in practice; but, the 3-D Monte Carlo inversion is much slower. For example, inversion of a data set corresponding to a measuring setup with nine loops provides the solution and the uncertainty estimate, but inversion takes about 10 hours with an ordinary laptop computer – although leaving the computer running overnight and getting the results in the morning is one solution. Moreover, when using methods based on a regularization that is much faster, it is possible to spend quite a lot of time analyzing and optimizing the inversion and so the total time consumption may, in practice, be comparable with the Monte Carlo inversion.

Inversion of SNMR data is ill-posed. Different methods for resolving ill-conditioned inverse problems can be found in the literature [TAR 05]. In this book we limit our presentation to the most popular Tikhonov regularization method [TIK 77]. The water content distribution $\mathbf{w}$ is the solution of matrix equation

$\mathbf{Aw}=\mathbf{e_0}$. To find an approximate solution, this method presupposes a minimization of Tikhonov's functional

$$TF(\alpha)=\left\|\mathbf{Aw}-\mathbf{e_0}\right\|_{L_2}+S^{damp}=\min, \qquad [4.34]$$

where $S^{damp}_{1D}=\alpha_z\times\left(\frac{\partial}{\partial z}\mathbf{w}\right)^2$, $S^{damp}_{2D}=\alpha_x\times\left(\frac{\partial}{\partial x}\mathbf{w}\right)^2+\alpha_z\times\left(\frac{\partial}{\partial z}\mathbf{w}\right)^2$ and $S^{damp}_{3D}=\alpha_x\times\left(\frac{\partial}{\partial x}\mathbf{w}\right)^2+\alpha_y\times\left(\frac{\partial}{\partial y}\mathbf{w}\right)^2+\alpha_z\times\left(\frac{\partial}{\partial z}\mathbf{w}\right)^2$ are the estimates of the smoothness of the solution and $\alpha_x,\alpha_y,\alpha_z>0$ are the smoothing factors in each direction.

For optimization we prescribe the non-negative water content ($\mathbf{w}$). The misfit between theoretical ($\mathbf{Aw}$) and experimental ($\mathbf{e_0}$) signals (residual mean square, RMS) used for calculating gradients is calculated as

$$RMS=I^{-1}\sum_i\left((\mathbf{Aw})_i-e_{0i}\right)^2, \qquad [4.35]$$

where matrix $\mathbf{A}=\left[\sqrt{\mathrm{Re}(\mathbf{A})^2+\mathrm{Im}(\mathbf{A})^2}\right]$ and the data vector $\mathbf{e_0}=\left[\sqrt{\mathrm{Re}(\mathbf{e_0})^2+\mathrm{Im}(\mathbf{e_0})^2}\right]$ are composed of amplitudes (amplitudes' inversion) or they are composed of complex signals (complex signals' inversion): $\mathbf{A}=\begin{bmatrix}\mathrm{Re}(\mathbf{A})\\ \mathrm{Im}(\mathbf{A})\end{bmatrix}$ and $\mathbf{e_0}=\begin{bmatrix}\mathrm{Re}(\mathbf{e_0})\\ \mathrm{Im}(\mathbf{e_0})\end{bmatrix}$. In practice, optimization of the amplitudes after calculating complex signals is often used. In this case the misfit is calculated as

$$RMS=I^{-1}\sum_i\left(\left(\sqrt{\mathrm{Re}(\mathbf{Aw})^2+\mathrm{Im}(\mathbf{Aw})^2}\right)_i-e_{0i}\right)^2, \qquad [4.36]$$

where $\mathbf{A} = \begin{bmatrix} \mathrm{Re}(\mathbf{A}) \\ \mathrm{Im}(\mathbf{A}) \end{bmatrix}$ and $\mathbf{e_0} = \left[\sqrt{\mathrm{Re}(\mathbf{e_0})^2 + \mathrm{Im}(\mathbf{e_0})^2} \right]$.

Otherwise, the SNMR inversion has no special features in comparison with other geophysical inverse problems and does not require detailed presentation. For the optimization itself, we use the conjugate gradient method [STO 80]. Successful use of the Gauss–Newton method developed for electrical resistivity tomography [GÜN 06] has been also reported [HER 07].

When performing inversions for the relaxation times using the TSI approach presented in section 4.2, we need to find $w_T(\mathbf{r},t)$ for each time step t_i. For that we use the same routine as presented above, but additionally we prescribe smoothness to the solution in the time domain by adding a penalty to the minimization function. In this case equation [4.34] becomes

$$\begin{aligned} TF(\alpha) &= \left\| \mathbf{Aw} - \mathbf{e_0} \right\|_{L_2} + S^{damp} + \\ &\alpha_T \sum \left((w_{t_{i-1}} - w_{t_i})^2 + (w_{t_{i+1}} - w_{t_i})^2 \right) = \min \end{aligned} , \qquad [4.37]$$

where α_T is the smoothness constraint in the time domain. Depending on the practical realization, inversions can be carried out in one or two steps. If two steps were selected then the first run contains individual inversions for each moment of time t_i using only smoothness constraints in spatial distribution (equation [4.34]). For the second run equation [4.37] is used. Decomposition of the solution $w_T(\mathbf{r},t)$ into exponential functions is carried out using the simple least square inversion.

4.5. Nonlinear inverse problems

In the majority of applications the SNMR inverse problem is linearized and interpretation is carried out using linear least squares inversion. However, in some cases linearization cannot be done accurately which causes biases in the inversion results. A nonlinear inversion can also be used for improving interpretation of SNMR measurement or for performing a joint inversion when using different geophysical measurements. In this chapter we will present two examples when the SNMR inverse problem was treated as a nonlinear inversion.

4.5.1. *Inversion of the geomagnetic field variations*

For performing SNMR measurements, the instrument's reference frequency should be set equal to the Larmor frequency as defined by the Earth's magnetic field.

In this case the Earth's magnetic field is assumed to be constant. However, this is not always possible as the Earth's magnetic field may vary in time and have lateral variations, caused by the presence of magnetic rocks. In these cases measurements may be carried out under off-resonance conditions. Knowledge of the frequency offset between the Larmor frequency and the instrument reference frequency is important for the correct interpretation of experimental data. Thus, knowledge of the Earth's magnetic field is important when working with the SNMR method.

Measurements of the geomagnetic field during an SNMR survey using a proton magnetometer is the simplest way to obtain the frequency offset caused by time variations to the Earth's magnetic field. The problem is much more complex when the Earth's magnetic field in the subsurface is not constant. In this case the Earth's magnetic field in the investigated area should be measured in boreholes and then extrapolated between the boreholes.

Another way of determining the Earth's magnetic field is by using SNMR measurements. Indeed, the SNMR instrument is a large magnetometer and, in the presence of water saturated formations, the frequency of the SNMR signal contains information about variations in the Larmor frequency. This information can be provided by the inversion of recorded SNMR time series.

When modeling the frequency offset, it is important to know whether the Larmor frequency varies in time or in space. In the previous chapters we have considered that the pulse moment is the imaging parameter, which makes resolving water distribution in the subsurface possible. In order for this to happen, it is assumed that the Earth's magnetic field is constant during measuring time. However, SNMR measurements at one station may take a few hours and if the Earth's magnetic field varies then these time variations may be interpreted as spatial variations in the Earth's magnetic field.

When calculating the SNMR signal under off-resonance conditions ($\Delta\omega \neq 0$) using equations [4.4] – [4.6], the frequency offset $\Delta\omega(\mathbf{r})$ can be taken into account in three different ways:

– If $\Delta\omega(\mathbf{r}) = const$ then this value is set for all pulse moments and for the entire subsurface.

– If $\Delta\omega(\mathbf{r}) = \text{var}$, but $\Delta\omega(t) = const$ then the Earth's magnetic field varies in space and known values of $\Delta\omega$ distribution should be used for calculating the SNMR signal generated by corresponding volumes of the subsurface (by different depth intervals when using 1-D inversion). For a given model layer the same value of $\Delta\omega$ is set for all pulse moments.

– If $\Delta\omega(\mathbf{r}) = const$, but $\Delta\omega(t) = \text{var}$ then the Earth's magnetic field varies in time. In this case time variations of $\Delta\omega$ should be converted in variations of the frequency offset versus pulse moment $\Delta\omega(q)$ and the values of $\Delta\omega$ should be used for computing SNMR signal for the corresponding values of the pulse moment. In this case the same distribution $\Delta\omega(q)$ should be used for all model layers.

In practice, for distinguishing between time and space variations of the Larmor frequency, measurements are carried out using disordered values of the pulse moment. It means that instead of progressively increasing or decreasing values of the pulse moment during measuring, the instrument is programmed to mix large and small pulse moments. Otherwise, one should regularly check the Earth's magnetic field with a proton magnetometer.

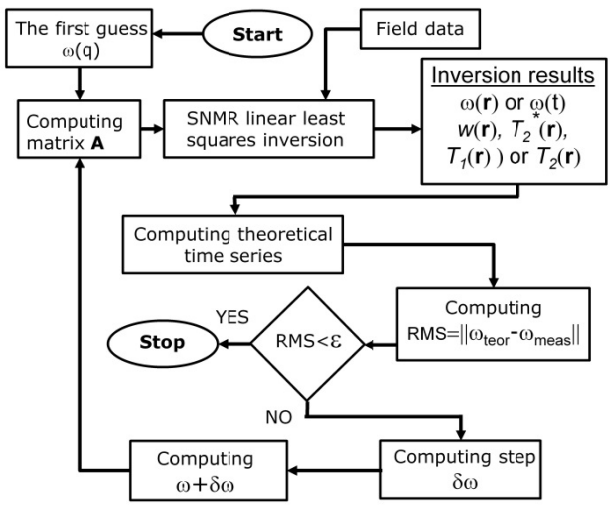

Figure 4.19. *Flowchart of the SNMR frequency offset inversion*

The inversion scheme that allows recovering variations of the frequency offset is presented in Figure 4.19. An inversion algorithm is based on linear least squares inversions, with an iterative adjustment of the frequency offset. The first estimate is derived from the spectra of time records. These data are used for calculating matrix

A. Experimental data are inverted, assuming a linear inverse problem, thus providing distribution of the water content and the relaxation times for the corresponding frequency offset. Inversion results make it possible to calculate the theoretical time series and to compare these time series with measured time series. If the discrepancy between the two is smaller than the experimental error, then inversion is stopped and results provided by the inversion are considered as the solution. Otherwise a gradient of the frequency offset is calculated and matrix **A** is calculated with the modified values of $\Delta\omega$. Remember that for this algorithm it is necessary to know which variation of the Earth's magnetic field (space or time) was present.

This algorithm was verified with real data and showed sufficiently fast convergence. Detailed analysis of this inverse problem is beyond the scope of this book.

4.5.2. *Inversion of the resistivity distribution*

It follows from equations [4.4] – [4.6] that an SNMR signal is sensitive to the distribution of the electromagnetic field $\beta_{\perp}(\mathbf{r})$ generated by the surface loop [SHU 96]. $\beta_{\perp}(\mathbf{r})$ depends on the electrical resistivity of the subsurface and hence inversion of SNMR measurements can provide information on the resistivity. This information may be of particular interest when no other data about the investigated area is available. The inverse problem which enables us to resolve the resistivity is nonlinear.

A successful implementation of the inversion of field data was reported in [BRA 08]. Inversion was carried out using a limited number of layers (block inversion). Results show that the resistivity of the subsurface derived from SNMR inversion was comparable to those obtained with DC resistivity and transient electromagnetic measurements. An algorithm for resolving this nonlinear inverse problem is summarized in Figure 4.20.

For practical realization, an assumption was made that the boundaries of water saturated layers and the boundaries of geological layers with different resistivity coincide. The algorithm is now composed of two steps. Firstly, the SNMR signals (either amplitudes or complex signals) are inverted based on an assumption on the resistivity distribution (the first guess). The SNMR inversion enables the distribution of the water content and of the relaxation times. However, inversion results may be biased if the resistivity assumed for calculating matrix **A** does not correspond to the true resistivity in the test site. Secondly, the resistivity is inverted using a nonlinear

algorithm, assuming the number and the boundaries of layers for the resistivity model to coincide with the number and the boundaries of layers from the SNMR inversion for the water content model with fixed resistivity. The nonlinear resistivity inversion aims to minimize the discrepancy between measured and theoretical SNMR signals by varying the resistivity of each layer. If the water content distribution and the resistivity distribution obtained in the iteration i were not changed in comparison with the iteration $i-1$, then inversion is done. Otherwise the new value of the resistivity distribution is used to calculate matrix **A** and to start the iteration $i+1$.

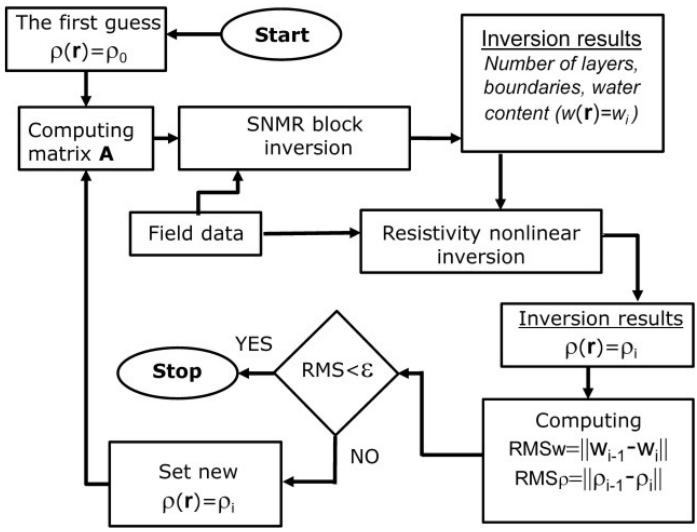

Figure 4.20. *Flowchart of the SNMR resistivity inversion*

5

Link Between SNMR and Aquifer Parameters

SNMR is one of the recent geophysical methods developed specifically for groundwater investigation. This method is selectively sensitive to groundwater, a competitive advantage when compared to other non-invasive geophysical tools used for hydrogeological purposes. The SNMR method could be presented as a combination of the time and frequency domain electromagnetic methods used in geophysics, and of the NMR logging (NML) petrophysical method. SNMR takes the calculation of EM fields in the subsurface, and large-scale imaging techniques, based on the resolution of the inverse problem, from geophysics. Experience gained in the laboratory concerning NMR methods and NML allows us to develop the capability of SNMR to characterize water-saturated porous media.

Laboratory NMR and NML are widely used in petrophysics. An excellent review of petrophysical applications of the NMR phenomenon is presented in [DUN 02]. SNMR is based on the same theory as NML and both methods have much in common, but the differences are also significant and, unfortunately, the application of the experience gained in NML to the interpretation of SNMR data is not straightforward. When using SNMR, one should be aware of the following differences:

1) SNMR uses a much lower static magnetic field (Earth's magnetic field) than laboratory or NML instruments, which use special magnets for creating an artificial magnetic field. Many processes that influence the NMR response are magnetic field dependent, hence the results of laboratory and SNMR experiments often have only qualitative correspondence. A low static magnetic field imposes low sensitivity, which is compensated by a large volume of investigated samples.

2) The volume investigated with an SNMR sample is much larger than the volume investigated in a laboratory or in a borehole with NML. Laboratory and

NML instruments are able to resolve small volumes – a few cubic millimeters to a few tens of cubic centimeters. The minimum volume that can be characterized with SNMR is more than a few hundred cubic meters. Thus, SNMR provides results averaged over a few hundred cubic meters of rock.

3) Operating at low frequency (800–2600 Hz), SNMR is not able to quantify the total porosity due to the difficulties associated with measuring short signals. Short signals also make it difficult to identify water because of the additional transient signals generated by electrically conductive rocks. Measuring short signals requires short pulses, thus reducing SNMR's depth of investigation.

4) SNMR should work in any type of geology and often in unconsolidated materials. The serious difficulties of obtaining undisturbed samples, different static magnetic fields, and its high dependence on hydrogeological processes render it difficult to directly compare field results obtained by SNMR with results obtained in a laboratory with rock samples.

SNMR is used for investigating aquifers, but it also has potential for investigating water in the unsaturated zone [ROY 05; COS 11a; COS 11b]. SNMR efficiency is proven in practice and has been the subject of many scientific publications. The majority of the reported results either show a development in the SNMR method, or different aspects of aquifer characterization. However, SNMR results are also seen as a source of data for hydrogeological modeling. Usually SNMR is used as an interpolation tool for obtaining information between boreholes where calibration is possible. The reported integration of SNMR in the modeling scheme demonstrates the potential of this approach [BOU 09b; BOU 12; HER 12; VOU 12a; WYN 04].

SNMR is an emerging method, but it should not be seen as a miraculous solution for all the problems in hydrogeology. Thus, in order to use SNMR correctly, it is important to know the specificity of this method – an analysis of the SNMR method as a geophysical tool for hydrogeologists is the subject of this chapter. In order to make the presentation of this subject easy to read for non-hydrogeologists, we will go over some basic hydrogeological definitions.

5.1. Parameters used for characterizing an aquifer

An aquifer can be defined as a geological formation accumulating groundwater and in which water may flow through interconnected pores or fractures. Water is extracted by boreholes and then used for human needs. Aquifers may be classified by the hydrostatic pressure [MAR 86]. Different types of aquifer are schematically presented in Figure 5.1. An unconfined aquifer is an aquifer in which water and

rocks are under atmospheric pressure and thus the static water level (SWL) coincides with the top of this aquifer. An example of an unconfined aquifer is a 20-m-thick sand deposit over a clay formation with the static water level at 5 m. In this case the layer from 5 to 20 m is an unconfined, or free, aquifer. A confined aquifer is a geological formation in which water and rocks are under a pressure higher than atmospheric pressure. Another example of a confined aquifer could be a water saturated sand formation located between two low permeable clay layers with the static water level above the top of the sand formation. Water may also accumulate in small sand lenses overlying low permeable formation (clay), thus creating local unconfined aquifers, often temporary (perched aquifers). The static water level in such an aquifer may be above the regional water table. Aquitard is a layer with low hydraulic conductivity (clay or non-porous rock).

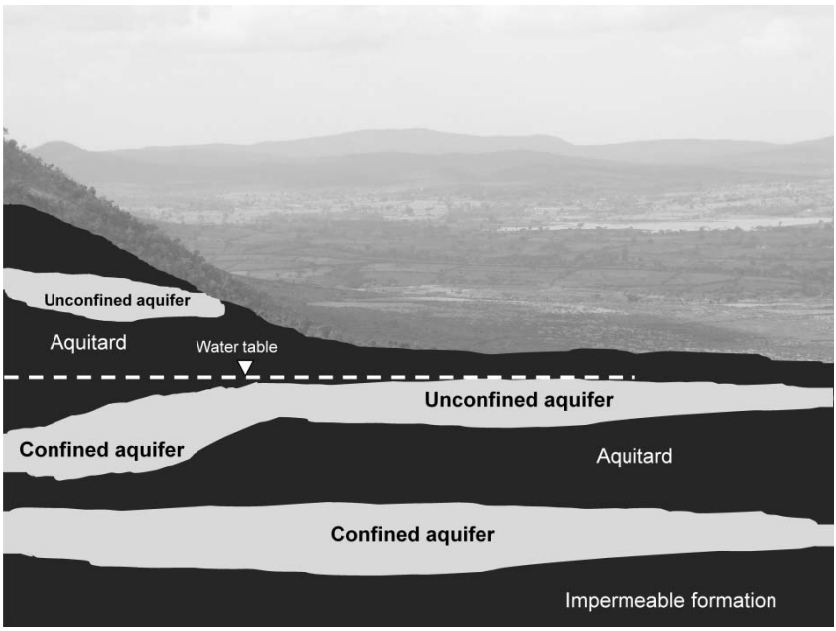

Figure 5.1. *Different types of aquifers classified after the hydrostatic pressure*

Different aquifers may exist in one area and can be either isolated or interconnected. Detection and localization of aquifers is the first step of a hydrogeological study. In practice, information on the geometry, extension and, if possible, interconnectivity of different aquifers is often obtained using surface geophysical methods.

Water quality is one of the issues that determine the practical importance of an aquifer as a water resource. Water salinity is one of the parameters that characterizes water quality. In coastal areas, salinization of aquifers is one of the key parameters that should be taken into account for optimal water management. A strong relationship between water salinity and the electrical resistivity of the aquifer formation renders electrical and electromagnetic methods an efficient tool for evaluating water quality.

An aquifer's ability to provide water is characterized using the storage-related parameters and flow related parameters.

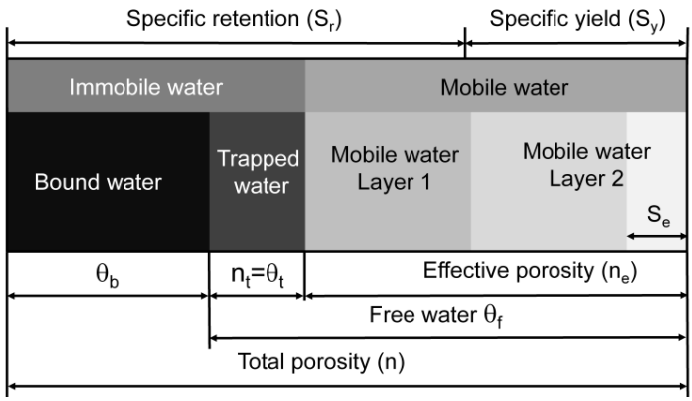

Figure 5.2. *Conceptual storage parameters of an aquifer (after [LUB 05])*

The storage-related parameters are schematically presented in Figure 5.2 [LUB 05]. The total porosity n represents the percentage of voids in the total volume of rock and soil. Voids can be filled with water and air. An aquifer is usually considered to be a fully water saturated formation and so we can assume that all voids are filled with water. Water in the aquifer is divided into two parts: mobile and immobile water. Immobile water is attached to the rock by the force of molecular attraction and does not contribute to water flow. θ_b is the water content corresponding to the quantity of bound water and θ_f corresponds to free water, which is not attached to rocks. Some free water may be located in non-connected voids and hence cannot move. This portion of water is called trapped water and is characterized by the trapped porosity $n_t = \theta_t$. Mobile water is characterized by the effective porosity n_e. The portion of water that can be removed by the forces of

gravity is quantified by the specific yield and other water by the specific retention S_r. In confined aquifers water that can be released because of the compressibility of the rock is characterized by the elastic storativity S_e

$$S_e = \rho g(\alpha + n\beta)\Delta z, \qquad [5.1]$$

where Δz is the thickness of the aquifer formation, ρ is the water density, g is acceleration due to gravity, α is the compressibility of the rock, β is the compressibility of water under given stress and n is the porosity.

The hydrostatic water column provides a volumetric estimation of free water content and allows us to evaluate the potential of an aquifer and comparison aquifers. It is defined as

$$H_w = \theta_f \Delta z, \qquad [5.2]$$

where θ_f is the free water content and Δz is the thickness of the aquifer formation.

It is important for hydrogeologists to know all the storage parameters of an aquifer, but knowledge of the specific yield S_y and the elastic storativity S_e is critical because it enables us to quantify the amount of extractable water.

The flow-related parameters describe the capacity of an aquifer to conduct water. Figure 5.3a offers an example of the aquifer formation, with a hydraulic head gradient estimated in two boreholes. The water flow in an aquifer is characterized by the hydraulic conductivity K. In a simple case, K is the proportionality coefficient between the Darcy velocity V and hydraulic head drop Δh observed over the distance L

$$V = -K \times \Delta h / L. \qquad [5.3]$$

Figure 5.3b shows water-filled pores (light gray areas) in rock (dark gray areas). We can see that the quantity of stored water depends primarily on the volume of pore bodies (porosity), and that the capacity of water to flow through the porous media depends on the cross section of pore throats (interconnection between the pores). A more complete characteristic of water flow through an aquifer is given by the transmissivity

$$T = K \times \Delta z, \qquad [5.4]$$

where Δz is the thickness of the aquifer formation.

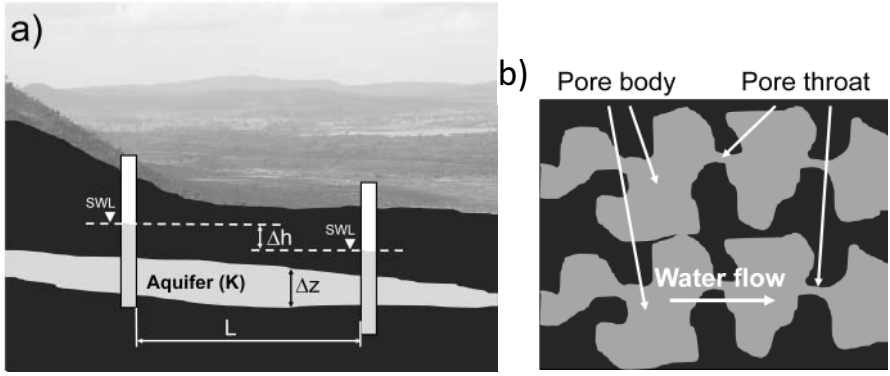

Figure 5.3. *Flow-related parameters of an aquifer: a) Darcy flow; b) pore geometry*

Hydrogeologists would like to obtain the following information about the area of investigation at a reasonable cost: 1) detection (whether aquifers exist in the area of investigation, how many, etc.); 2) geometry (depth, thickness, extension of each detected aquifer); 3) storage-related parameters (primarily S_y and/or S_e); 4) flow-related parameters (K and T); 5) water quality (only water salinity can be estimated by geophysical surface methods).

Hydrogeologists use different methods for characterizing aquifers, but the most universal method is the pumping test. Pumping tests consist of pumping water from a well and observing the water level in one or more neighboring wells. The dynamics of the water level variations in response to the pumping rate can be interpreted in terms of the porosity and the transmissivity of the aquifer being investigated. Boreholes also provide information on aquifer geometry.

5.2. Available SNMR estimates on aquifer parameters

5.2.1. *Detection of groundwater*

The detection of water-saturated geological formations is the most reliable information provided by an SNMR survey. An SNMR signal is generated by groundwater molecules and a simple observation of the SNMR response is a very reliable indicator of groundwater. However, SNMR is sensitive to the total volume of water below the measuring loop and, in practice, the capacity of water detection is limited by the signal-to-noise ratio. Detectable water volume can be estimated by a product of the SNMR water content and the thickness of the aquifer. For example, let us consider a 50×50 m^2 loop (two turns) and a 10-nV-threshold. Modeling results

show that SNMR is able to detect a 20-m-thick weathered rock aquifer with a water content of 1% down to 20 m (top of the aquifer) and with a water content of 2% down to approximately 50 m. If the fractured part of the hard-rock aquifers is characterized by an average effective porosity of 0.1% to 0.2%, then the total water volume is small and would be barely detectable [LEG 06].

In the presence of magnetic rocks, the Earth's magnetic field is often heterogeneous and SNMR measurements may be disturbed. This problem can be resolved, in part, by using the SE measurements, however the SE signal is smaller and hence the performance of the method in the SE mode is not as good as in the FID mode.

A very convincing demonstration of the sensitivity of the method to the volume of water below the loop has been obtained during investigation of the Tête Rousse glacier in French Alps [VIN 12]. SNMR study of this glacier was aiming either to detect water accumulation in the glacier body or to confirm that the glacier does not contain much water, which would be potentially dangerous for the local population and infrastructure. Figure 5.4 shows the amplitude of the SNMR signal observed with a loop located over the cavern (solid line). An SNMR signal was observed well above the noise level, suggesting a water filled cavern in the glacier. Then, 3-D SNMR inversion located the cavern at a depth of between 30–65 m below the glacier's surface. The estimate of the volume of accumulated water revealed 55,000 m^3 with the uncertainty of ±20% [LEG 11a]. This volume was considered as dangerous and about 48,000 m^3 of water was pumped out. Pumping stopped when the cavern became empty. SNMR measurements after the draining of the cavern have been performed with the same loop and at the same location as prior to pumping and the amplitude of the signal was observed at about 15 nV, which is close to the noise level (Figure 5.4).

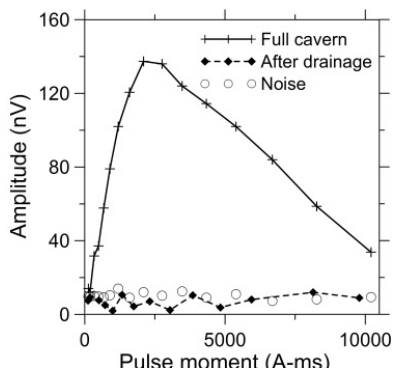

Figure 5.4. *Experimental verification of the capability of the SNMR method to detect groundwater: amplitude of the SNMR signal versus pulse moments before and after drainage of the cavern in the Tête Rousse glacier*

5.2.2. *Aquifers and geometry*

The location and geometry of aquifers can be reliably derived from SNMR inversion. It has been shown in Chapter 4 that the SNMR inverse problem is ill-posed and, consequently, the spatial resolution of the method is limited by the uncertainty in the inversion results. Inversion accuracy depends on many factors. In general, the resolution of the method allows for a definition of the geometry of the aquifers being investigated, at best, with an uncertainty of a few meters for shallow aquifers and with an uncertainty of more than 10 m for deeper aquifers (Figure 4.10). Inversion results concerning the aquifers being investigated are reliable without any additional information (only resistivity of the subsurface need be known), but if such information is available then constrained inversion may provide better accuracy. In our experience, two to three aquifers can be identified after SNMR results.

For MRS measurements carried out in Saint-Cyr-en-Val area (France), a 100-m-side square loop was used. The reliable depth of investigation for this loop is about 100–120 meters. Information about the resistivity distribution was obtained using the Time Domain Electromagnetic Method (TDEM). Block inversion results are presented in Figure 5.5c.

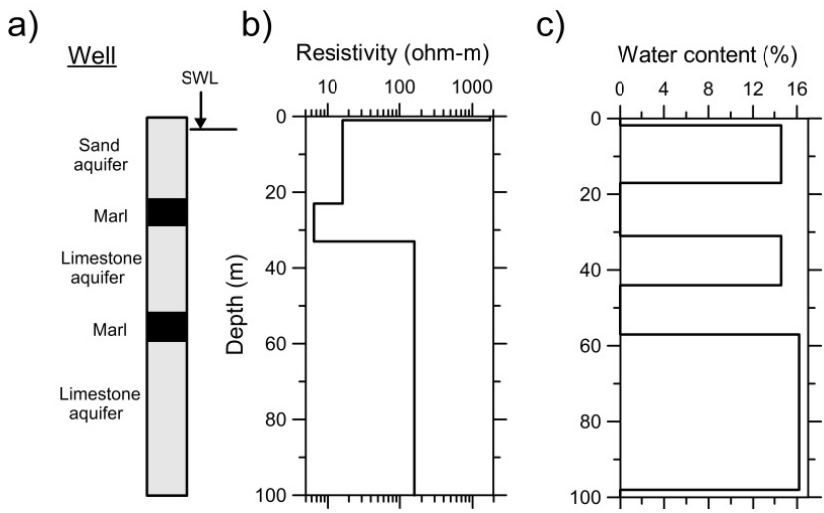

Figure 5.5. *Example of 1-DSNMR inversion near borehole in France: a) borehole log; b) geoelectrical cross section derived from TDEM measurements; c) SNMR water content versus depth*

The borehole at this site shows three aquifers separated by marl layers (Figure 5.5a). TDEM results (Figure 5.5b) reveal the location of the shallow aquifer and the first aquitard. The second aquitard was not detected by the TDEM as this

deep marl layer contains high quantities of limestone materials and therefore has the resistivity value close to that of limestone. It should be noted that the second marl layer is close to the limit of the resolution capacity of the SNMR method and experimental data can be fairly well fitted with two aquifers: one shallow and one thick deep aquifer. Under these conditions the three aquifer structures are retained, taking into account the borehole results.

An evaluation of the SNMR capacity to detect the top of the aquifer has been reported in [VOU 07b]. The summary of the investigation of aquifers in France and in Niger composed of essentially sand materials is presented in Figure 5.6. The depth to the top of the aquifer derived from the SNMR inversion is presented in contrast with the static water level measured in boreholes. These experimental results demonstrate that SNMR is able to resolve the depth to groundwater. The method's limited resolution observed was found to correspond with the mathematical estimates of the uncertainty of SNMR inversion results.

For 1-D SNMR inversion, the subsurface can be considered as homogeneous if water saturated formations do not vary at a distance of roughly three times the loop size. However, heterogeneous formations like karst or fractured rock aquifers may change their hydrodynamic properties at smaller distances. For investigating and modeling heterogeneous aquifers SNMR should be applied in the 2-D and 3-D modes. Reported applications of 2-D SNMR measuring and inversion procedures show that the accuracy of the results was significantly improved [VOU 03; BOU 06; GIR 07; HER 07; LEH 11b; LEG 11b]. The 3-D SNMR application is a new development and only one case study has previously been reported [LEG 11a].

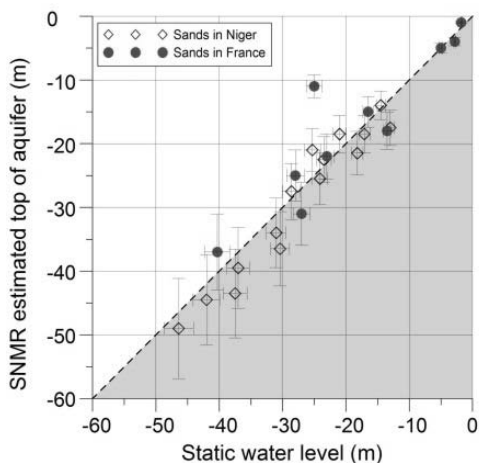

Figure 5.6. *Comparison of the depth to water in unconfined aquifers derived from 1-D SNMR inversion with the static water level measured in boreholes (after [VOU 07b])*

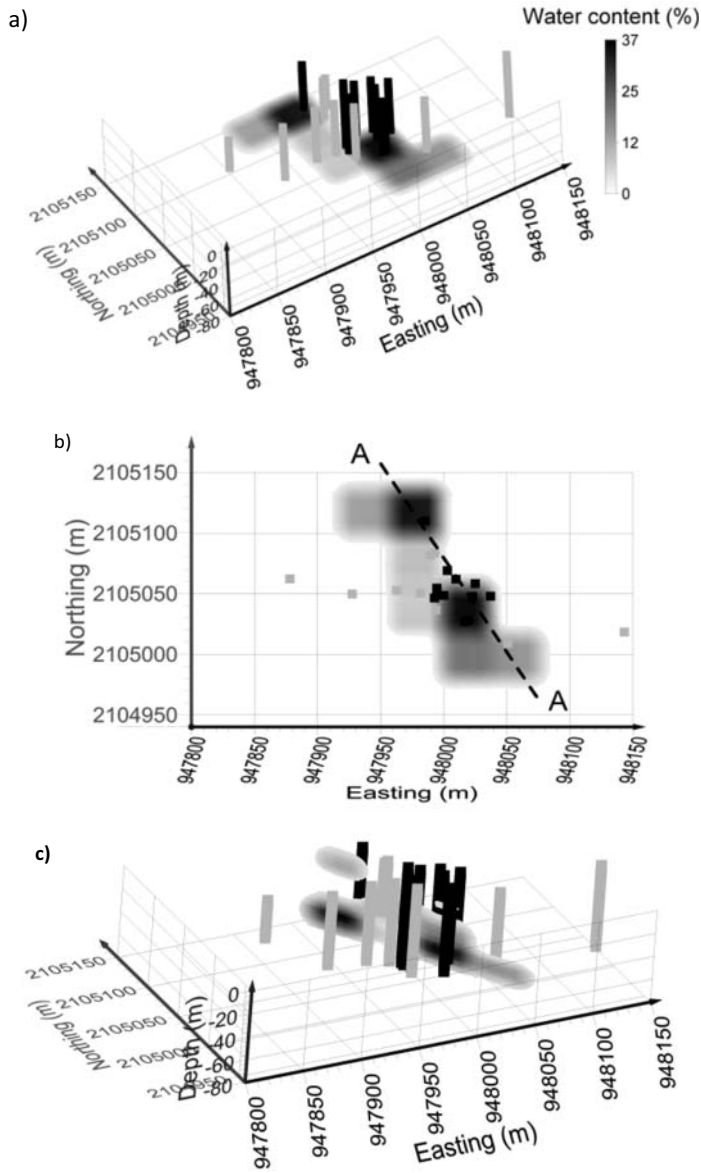

Figure 5.7. *Results of 3-D inversion show location of the water filled cavern in the Tête Rousse glacier. Black bars show position of boreholes, which crossed the cavern and grey bars show boreholes in ice. The cavern body is shown is three different views: a) a horizontal slice at the depth of 60 m; b) the plan of the cavern at the depth of 60 m and location of the cross-section A-A; c) the cross-section A-A*

For demonstrative purposes we will continue to use the results of a 3-D SNMR application for the investigation of water accumulation in the Tête Rousse glacier [LEG 11a; VIN 12]. An example of measured signals is presented in Figure 5.4. The measuring setup, which we have used during our 3-D survey in the Tête Rousse glacier, is presented in Figure 4.12. Thus, the analysis of the resolution of the 3-D SNMR inverse problem for the Tête Rousse data set is available from the presentation in Chapter 4. The inversion was carried out using the cells of $40\times40\times10\ m^3$. Figure 5.7 shows the results of the 3-D inversion of the data measured before the cavern was drained.

As the size of this cavern is smaller than the resolution of the inversion, the water content was averaged over a larger volume, and the average water content was found to be at only 37% instead of 100% in the real cavern. This example shows that, despite the limited resolution, 3-D SNMR results were confirmed to be reliable and very useful for local authorities when making decisions about the drainage of this cavern. Note that the cavern was detected with the SNMR alone and the drilling program was guided by the 3-D SNMR results.

5.2.3. *Storage-related parameters*

Laboratory NMR and NML instruments are able to quantify the total water saturated porosity. The classification of water in porous media used in petrophysics is presented in Figure 5.8. Bound water is characterized by a relaxation time shorter than 33 ms and water in clay can be identified by a relaxation time shorter than 3 ms. For longer than 33 ms relaxation time surface relaxation processes dominate over bulk relaxation (relaxation in bulk fluid). The bulk relaxation time for water is longer than 800 ms and between 33 and 800 ms – the relaxation time depends on the surface-to-volume ratio of the pores.

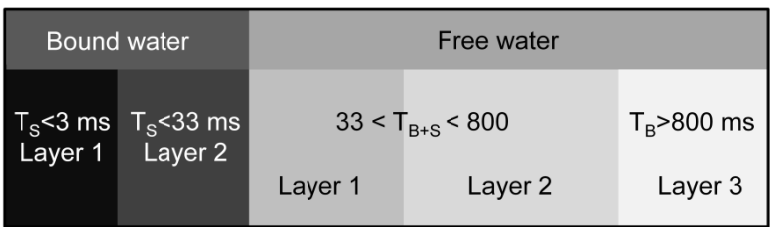

Figure 5.8. *Petrophysical classification of groundwater (after [DUN 02])*

SNMR has much lower resolution and only a small portion of bound water can be detected with SNMR instruments. A classification of groundwater observed with SNMR instruments is presented in Figure 5.9.

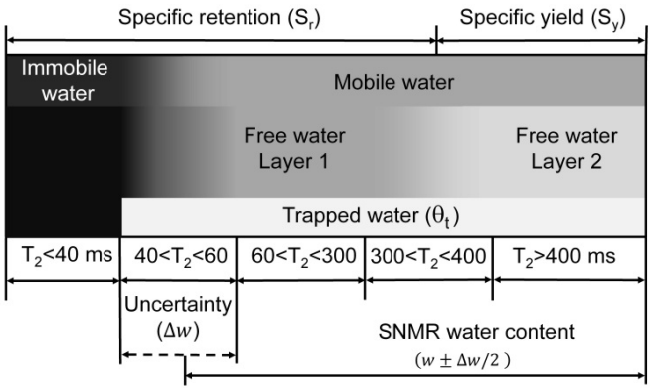

Figure 5.9. *Approximate classification of the groundwater being investigated with SNMR and definition of the SNMR derived water content*

Depending on the magnetic susceptibility of rocks and on the surface relaxivity rate, SNMR can either see some portion of bound water (for example in chalk or limestone) or some portion of mobile water can be lost. The magnetic susceptibility of rocks may vary a lot and thus, when rocks are magnetic (for example in basalt or magnetite) SNMR may lose a large portion of free water, or SNMR may in fact not be applicable. However, assuming small variations to magnetic susceptibility, we can approximately consider the uncertainty in an SNMR estimate of the free water content Δw as water corresponding to the relaxation time between 40 and 60 ms. Note, that even verification of this threshold is a difficult task owing to the large volume being investigated and thus, possible heterogeneity of the aquifer material.

Our experience shows that in coarse material water is characterized by a relaxation time longer than 400 ms and an SNMR estimate of the water content can be considered as an approximate value of the specific yield S_y. In order to acquire reliable results, calibration of the SNMR water content using a pumping test is recommended [VOU 08]

$$S_y = C_y w, \qquad [5.5]$$

where C_y is the calibration constant and w is an SNMR derived water content.

The relaxation time between 60 and 400 ms characterizes water in rocks with smaller to larger pore sizes respectively [SCH 91]. In small grain materials (fine sand, silt) surface relaxation processes dominate over bulk relaxation and SNMR

results are less accurate. In this case, equation [5.5] may be invalid and a linear approximation using two calibration constants has been proposed in [BOU 09a] as

$$S_y = C_y w + C_0 . \qquad [5.6]$$

Trapped water contributes to SNMR signals in the same way that mobile water does, however, trapped water is not available for extraction, and consequently it may cause additional error in SNMR results.

In confined aquifers the elastic storativity S_e is given by equation [5.1]. SNMR is not sensitive to the compressibility of rocks and water, but SNMR water content is related to the porosity. Thus, assuming that SNMR water content is an approximation of the porosity, S_e can be estimated as [VOU 07b]

$$S_e = C_e w \Delta z , \qquad [5.7]$$

where C_e is an empirical constant.

Note that only a few results reporting experimental verification of the correlation between SNMR derived water content and the specific yield or the elastic storativity are available, and it is not overlooked that the observed correlation for small grain materials may be nonlinear.

Examples of experimental verification of SNMR estimates of storage-related parameters are presented in Figure 5.10. Figure 5.10a presents results of an SNMR study of a sand aquifer in Niger [BOU 09a]. In this aquifer sand is not homogeneous and clay material is often intercalated with sand. Taking into account three values of S_y (small, medium and large), observed correlation can be considered as promising, even given that the number of experimental points is insufficient for reliable conclusions to be drawn. For smaller values of S_y we do not observe a clear correlation. It is unsurprising as surface relaxation is the principal component and SNMR estimates are less accurate for shorter relaxation times, corresponding to small S_y. Results of the investigation of a sand aquifer in Burma are presented in Figure 5.10b [VOU 07a]. We observe a greater number of measuring points for

comparison and hence we observe a more convincing correlation between S_e estimated using SNMR results and S_e measured with pumping tests. Note that in both cases, uncertainty in SNMR estimates due to measuring accuracy was comparable with the uncertainty estimated for pumping test results.

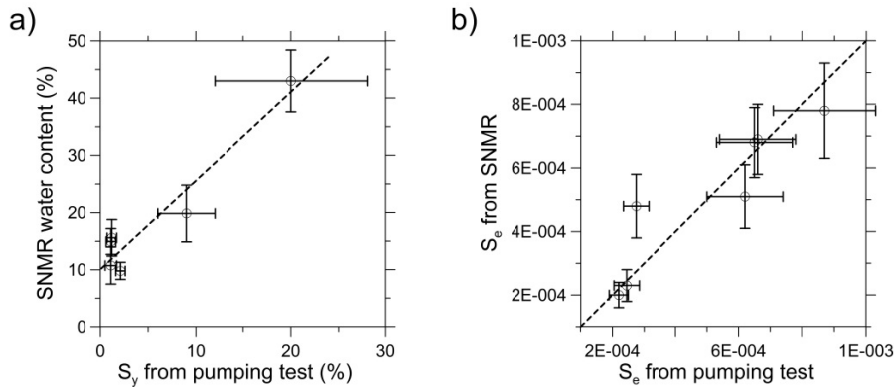

Figure 5.10. *Correlation between the storage related parameters and SNMR derived water content: a) SNMR water content plotted against specific yield estimated with pumping tests; b) elastic storativity estimated using SNMR derived water content versus elastic storativity obtained by pumping tests (after [VOU 07a])*

5.2.4. *Flow-related parameters*

Figure 5.3b shows schematically the structure of a porous medium with water filled pores. One can see that in this sketch water is principally located in pore bodies, but the water flow is governed by the size of pore throats. The amount of water in porous media is characterized by the porosity and the capacity of the medium to conduct water by the hydraulic conductivity. When conducting pumping tests hydrogeologists obtain direct information on both the porosity and the hydraulic conductivity. Obviously, trapped water is not seen by pumping tests because trapped water does not contribute to water flow caused by pumping.

SNMR measurements provide two parameters: the water content and the relaxation times $\left(T_1, T_2, T_2^*\right)$. All three relaxation times provide similar information, but T_2^* is additionally sensitive to local (at pore size) heterogeneities in

the Earth's magnetic field. SNMR is not able to investigate each individual pore and so measured parameters are averaged out over the volume being investigated, depending on the method's resolution capacity. For SNMR, the volume being investigated is more than a few hundred cubic meters of water saturated rock. Most water is located in pore bodies and, consequently, an SNMR signal provides information about water in pore bodies. Pore throats containing a small amount of water are not characterized by SNMR and hence SNMR cannot provide direct information on the capacity of the porous media to conduct water. Note that trapped water generates magnetic resonance signals indistinguishable from mobile water and consequently is identified by SNMR as mobile water.

It has been shown by many authors that the pores size estimates can be used for the prediction of hydraulic conductivity [NEL 94; SCH 98; NEL 05]. The pore size could be estimated from NMR measurements because the relaxation times are proportional to pore size [KOR 62; KEN 88; BAN 87; KLE 94; KEN 97]

$$T_1 \approx \frac{V}{\rho_1 S} \quad \text{and} \quad T_2 \approx \frac{V}{\rho_2 S}, \qquad [5.8]$$

where V/S is the pore volume-to-surface ratio, and ρ_1, ρ_2 are the surface relaxivity rates for T_1 and T_2 respectively.

Consequently, the hydraulic conductivity can be estimated using the NMR provided water content w and either T_1 or T_2 as

$$K = c \times T_1^b \times w^a \quad \text{and} \quad K = c \times T_2^b \times w^a, \qquad [5.9]$$

where a, b, c are empirically determined values that may be different for different rocks.

For sandstones a good permeability prediction was obtained on rock samples using $a = 4$ and $b = 2$ [KEN 88]. However, for SNMR data better results for sand aquifers were obtained using $a = 1$ and $b = 2$ [LEG 02b] and [LEG 04b] using estimators proposed by Seevers [SEE 66].

$$K = C_p \times T_1^2 \times w, \qquad [5.10]$$

where C_p is an empirical prefactor obtained after the calibration of SNMR with pumping tests. T_2 is rarely used in SNMR and only the use T_1 and T_2^* was reported in the literature. T_2^* is easier to measure and when investigating rocks with low magnetic susceptibility, (<10^{-5}SIU) can be safely used by replacing T_1 in equation [5.10].

In practice, for characterizing aquifer transmissivity T is often used. Transmissivity can be estimated using the thickness of aquifer Δz also derived from an SNMR inversion as

$$T = K \times \Delta z = C_p \times T_1^2 \times w \times \Delta z \,. \qquad [5.11]$$

In NMR logging the estimator $K \approx T_2^2 \times w^4$ is considered to be more accurate [KEN 97], but in SNMR $K \approx T_1^2 \times w$ has the advantage because it is more stable.

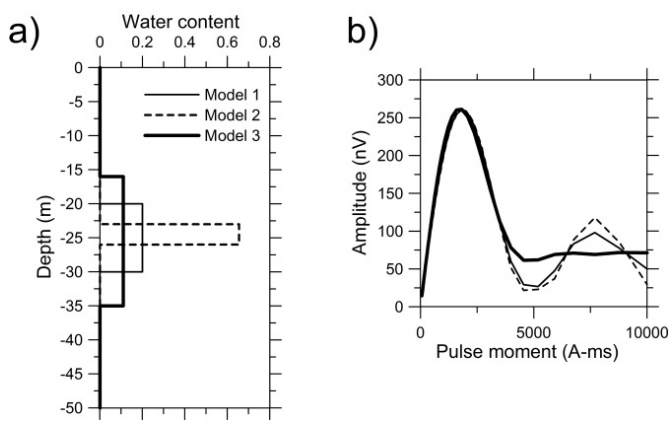

Figure 5.11. *Numerical demonstration of the equivalence problem in SNMR inversion: a) three different models; b) corresponding amplitude of SNMR signal versus pulse moment*

Indeed, an SNMR inversion is ill-posed and has a non-unique solution. These equivalent solutions may be different, but all of them fit experimental data within experimental error. However, it is known that w and Δz separately are less stable than their product $w \times \Delta z$. Consequently, when using equation [5.10] transmissivity

is estimated using the product $w \times \Delta z$ and when using $a = 4$ and $b = 2$ in equation [5.9] the estimator will be $w^4 \times \Delta z$. Now, let us see how these two estimators influence transmissivity predictions assuming the same T_1 value. In order to demonstrate this, we propose three models (Figure 5.11a). Models 1 and 2 are fully equivalent and model 3 is slightly less equivalent, but can often be considered as equivalent when interpreting experimental data. Figure 5.11b shows the amplitudes of an SNMR signal versus the pulse moment calculated for these models. Results presented in Table 5.1 clearly demonstrate that $w \times \Delta z$ is a more stable parameter than $w^4 \times \Delta z$.

Model	***Water content w***	***Thickness Δz (m)***	***Norm. estimator $w^4 \times \Delta z$***	***Norm. estimator $w \times \Delta z$***
Model 1	0.2	10	2.90E-02	9.57E-01
Model 2	0.655	3	1.00E+00	9.40E-01
Model 3	0.11	19	5.04E-03	1.00E+00

Table 5.1. *Transmissivity estimates based for three equivalent models presented in Figure 5.6 and calculated assuming a=1 and a=4 in equation [5.1]*

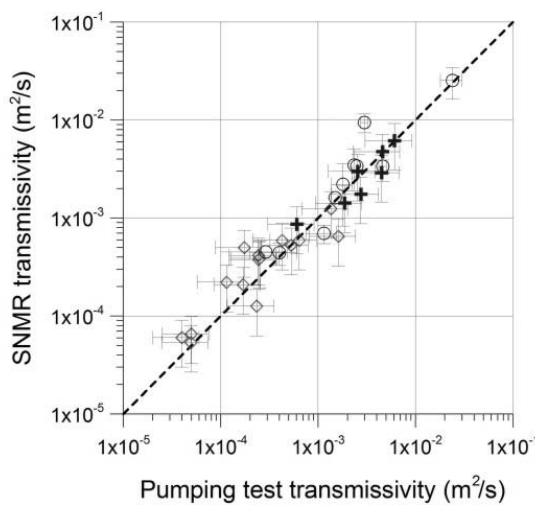

Figure 5.12. *Experimental verification of SNMR provided estimates of the transmissivity and transmissivity obtained by pumping tests (after [VOU 07b]). Circles represent sand aquifers in France; squares sand aquifers in Burma; and crosses sand aquifers in Niger*

Experimental verifications of SNMR prediction of transmissivity has been reported by many authors [VOU 05; CHA 08; PLA 08; VOU 08; BOU 09a; NIE 11]. They each underline the dependence of the empirical prefactor C_p on the rock type and recommend selecting representatives for local site conditions for calibration. Comparisons between SNMR predicted transmissivity and transmissivity estimated using pumping tests reported for sand aquifers is presented in Figure 5.12. We observe a very reasonable correspondence between the two. Note that the uncertainty of the SNMR prediction was close to that obtained by pumping tests.

A new approach for estimating hydraulic properties of aquifers was reported in [VOU 12b]. SNMR results have been compared with both specific yield calculated from pumping tests and effective porosity calculated from tracer tests. The SNMR water content was found to be equal to or higher than the specific yield and the effective porosity, thus confirming that SNMR measures capillary water in the unsaturated zone and a portion of bound water in rocks. Application of the newly developed, SNMR apparent-cutoff-time approach to the investigation of clayey sandstone aquifers of Cambodia allowed for the calculation of the specific yield with an average error of 23% and the effective porosity with an average error of 11%.

5.3. Joint use of SNMR and resistivity data

Joint inversion of different geophysical data sets is one of the research fields in applied geophysics. It has been shown in many papers that, under favorable conditions, joint inversion may significantly improve interpretation results. From the physical point of view SNMR measurements can be very naturally combined with the resistivity measurements. There is no particular mathematical difficulty for the practical realization of the inversion, and reports on successful applications of different algorithms of joint inversion of SNMR and TDEM data [ROM 98; BEH 12b] or SNMR and DC resistivity data [HER 02; GÜN 12] can be found in the literature. Often the use of joint inversions can reduce the uncertainty in the results provided by both SNMR and resistivity methods. In this book we do not intend to present a review of existing algorithms of joint inversions. Instead, we want to discuss how to use both SNMR results and electrical resistivity of geological formations derived either from TDEM (1-D) or DC resistivity electrical measurements (1-D and 2-D).

Examples of joint interpretations of SNMR results and the resistivity can be found in the literature [GOL 94; GEV 96; VOU 02; VOU 03; BAL 05; LAN 05; VOU 05; VOU 07a; DES 08; LEG 08; EZE 10]. Data measured with each method can either be inverted independently or joint inversions can be performed. The next step after inversion is joint interpretation. This entails the conversion of the physical parameters of the resolved structures into geological or hydrogeological descriptions of these formations.

The idea is based on the observation that different rocks may have equal electrical resistivity but different water content or relaxation time, and rocks with equal water content and relaxation time may have different resistivity. The combination of the water content, relaxation time and resistivity allows for a better interpretation of experimental results. Examples of the physical parameters of different rocks are presented in Table 5.2. The values presented in the table are rather general and a much more comprehensive description could be developed for a limited area where rock parameters are well known.

Formation	Rock material	w_{av} (%)	T_1 (ms)	Resistivity (ohm-m)	Comments
Magnetic rocks	Basalt, sand with 2% magnetite	0	na	na	In magnetic rocks MRS cannot deliver any information about the subsurface
Low permeable rocks (non-aquifer)	Clay	< 3	< 100	< 30	In the absence of mineralized water
	Dry sand, unsaturated weathered granite	< 1	< 100	> 1000	
	Solid granite			> 10000	
	Unsaturated zone: chalk, limestone	$2 \div 6$	< 100	$50 \div 200$	
Aquifer	Fissured granite, sandstone, non-fractured limestone	$2 \div 8$	< 200	Sea water < 3	Formation resistivity mainly depends on the resistivity of the water
	Highly fractured granite, sandstone, limestone		$350 \div 600$	Brackish water $3 \div 30$	
	Karst	$2 \div 3$	> 500		
	Compact chalk	$15 \div 20$	< 150	Fresh water $30 \div 200$	
	Highly fractured chalk		$350 \div 600$		
	Fine sand	$5 \div 15$	< 250		
	Medium sand		$250 \div 350$		
	Coarse sand		$350 \div 500$		
	Gravel		> 500		

Table 5.2. *Examples of different aquifers and their geophysical characteristics (after [LEG 04b])*

As an example, we propose a simplified algorithm to follow for joint interpretation (Figure 5.13). We assume three parameters: SNMR water content as the porosity estimate, SNMR prediction of the hydraulic conductivity and resistivity. For simplicity we adopt a gradation of just two values: low and high.

Figure 5.13a shows that high water content and high hydraulic conductivity correspond to an aquifer. A low resistivity of this formation indicates a salt-water aquifer. Figure 5.13b points to clay a formation. Note that if in this case the resistivity was high, SNMR and resistivity results would be interpreted as a hard rock formation.

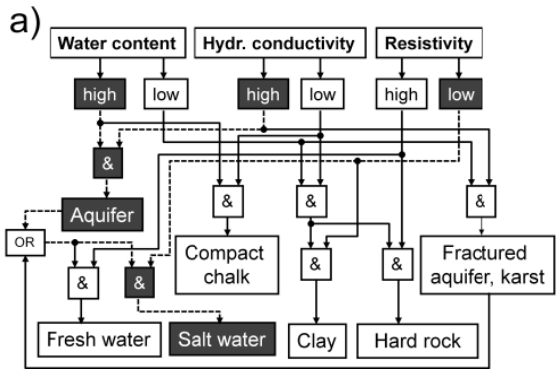

Figure 5.13a. *Example of an algorithm to follow for joint interpretation of SNMR and resistivity results*

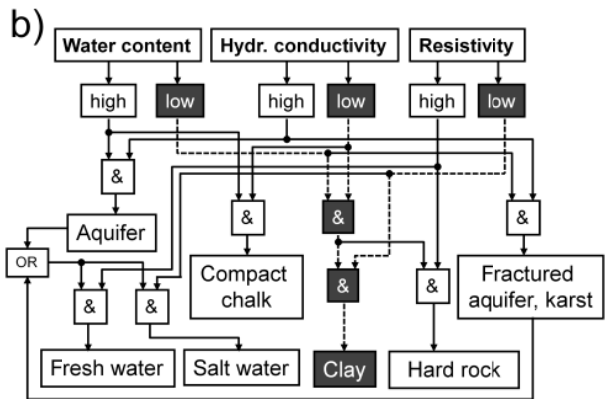

Figure 5.13b. *Example of an algorithm to follow for joint interpretation of SNMR and resistivity results*

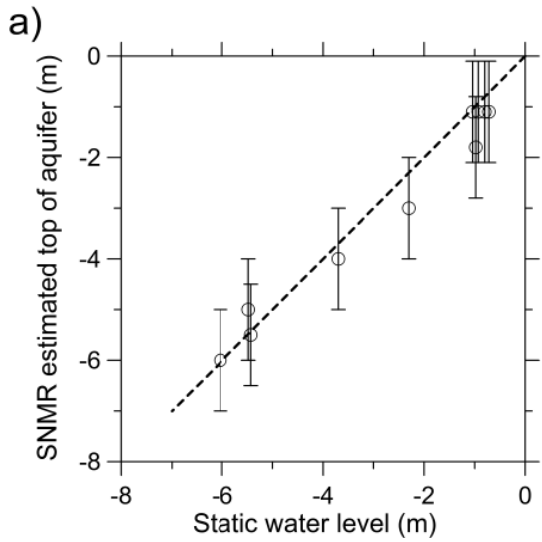

Figure 5.14a. *Field demonstration of the joint use of SNMR and ERT: a) comparison of the static water level measured in boreholes and the top of aquifer estimated by SNMR*

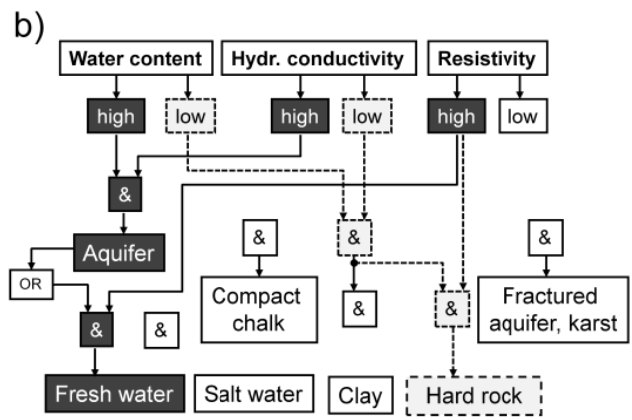

Figure 5.14b. *Field demonstration of the joint use of SNMR and ERT: b) interpretation of SNMR and ERT results in the central part of the profile (weathered granite aquifer) and in the northern part of the profile (hard rock)*

This approach is routinely used in practice. A case study of the joint use of SNMR and ERT (electrical resistivity tomography) methods is presented in [LEG 04b]. A small watershed in granitic environments was studied in Brittany,

France. SNMR provides a profile of 1-D soundings interpolated in 2-D cross sections, whilst ERT provides a 2-D cross-section of the resistivity. Comparisons of SNMR estimated depth to water is shown in Figure 5.14a. The aquifer is unconfined and the water level measured in boreholes corresponds to that derived from SNMR results. The resistivity was measured between 80 ohm-m and 10,000 ohm-m. Resistivity of 80 ohm-m may correspond to a fresh water aquifer and 10,000 ohm-m points to a hard rock. However, 80 ohm-m may also correspond to other formations (Table 5.2). Figure 5.14b shows an example of interpretations corresponding to the central part of the profile (Figure 5.15), pointing to fresh water aquifers and to the northern part of the profile suggesting that the subsurface is composed of hard rock. Geological interpretation shown in Figure 5.15d was made taking into account the general geological context of the area being investigated.

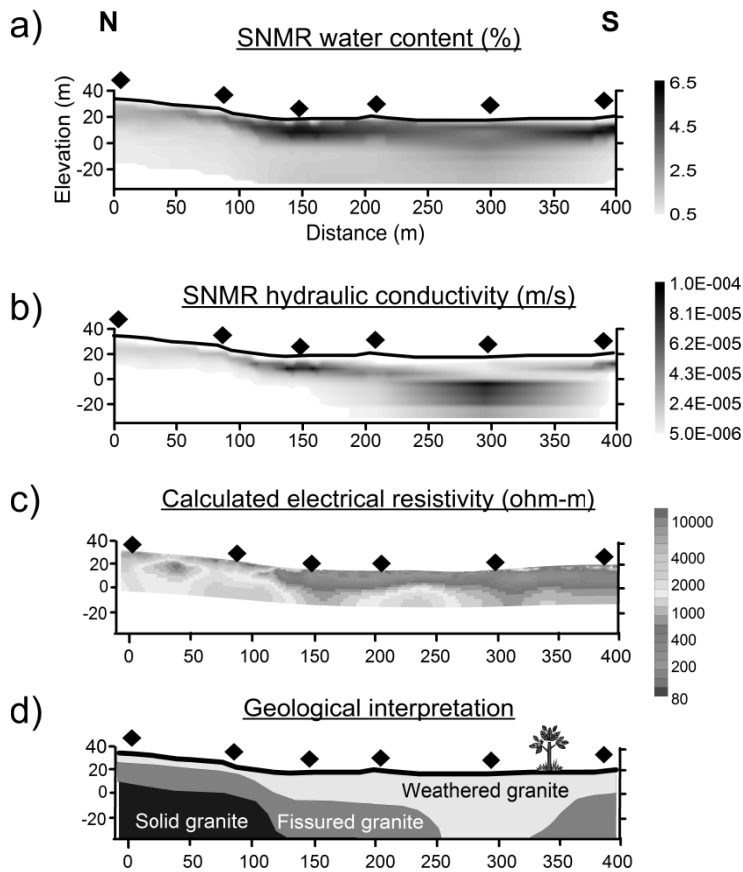

Figure 5.15. *Final results of SNMR and ERT study in French Brittany: a) SNMR water content; b) SNMR hydraulic conductivity; c) resistivity; d) geological interpretation*

Bibliography

[ABR 61] ABRAGAM A., *The Principles of Nuclear Magnetism*, Clarendon Press, Oxford, 1961.

[AND 79] ANDERSON W.L., "Numerical integration of related Hankel transforms of orders 0 and 1 by adaptive digital filtering", *Geophysics*, 44, 1287–1305, 1979.

[AND 89] ANDERSON W.L., "A hybrid fast Hankel transform algorithm for electromagnetic modelling", *Geophysics*, 54, 263–266, 1989.

[APP 06] APPELT S., KÜHN H., HÄSING F.W., BLÜMICH B., "Chemical analysis by ultrahigh-resolution nuclear magnetic resonance in the Earth's magnetic field", *Nature Physics 2*, 105–109, 2006.

[AST 05] ASTER R.C., BORCHERS B., THURBER C.H., *Parameter Estimation and Inverse Problems*, Elsevier Academic Press, 2005.

[BAL 05] BALTASSAT J.M., LEGCHENKO A., AMBROISE B., MATHIEU F., LACHASSAGNE P., WYNS R., MERCIER J.L., SCHOTT J.J., "Magnetic Resonance Sounding (MRS) and resistivity characterization of a mountain hard rock aquifer: the Ringelbach catchment", *Near Surface Geophysics*, 3, 267–274, France, 2005.

[BAN 87] BANAVAR J.R., SCHWARTZ L.M., "Magnetic resonance as a probe of permeability in porous media", *Physical Review Letters*, 58, 1411–1414, 1987.

[BEH 12a] AHMAD A., BEHROOZMAND A.A., AUKEN E., FIANDACA G., CHRISTIANSEN A.V., CHRISTENSEN N.B., "Efficient full decay inversion of MRS data with a stretched-exponential approximation of the T_2^* distribution", *Geophysical Journal International*, 190, 900–912, 2012.

[BEH 12b] BEHROOZMAND A.A., AUKEN E., FIANDACA G., CHRISTIANSEN A.V., "Improvement in MRS parameter estimation by joint and laterally constrained inversion of MRS and TEM data", *Geophysics*, 77, 4, 2012.

[BEN 90] BENDEL P.J., "Spin-echo attenuation by diffusion in non-uniform field gradients", *Journal of Magnetic Resonance*, 86, 509–515, 1990.

[BLO 46] BLOCH F., HANSEN W.W., PACKARD M., "Nuclear induction", *Physical Review*, 69, 127, 1946.

[BLO 55] BLOOM A.L., "Nuclear induction in inhomogeneous fields", *Physical Review*, 98, 1955.

[BOU 06] BOUCHER M., GIRARD J.-F., LEGCHENKO A., BALTASSAT J-M., DÖRFLIGER N., CHALIKAKIS K., "Using 2D inversion of magnetic resonance soundings to locate a water-filled karst conduit", *Journal of Hydrology*, 330, 413–421, 2006.

[BOU 09a] BOUCHER M., FAVREAU G., VOUILLAMOZ J.-M., NAZOUMOU Y., LEGCHENKO A., "Estimating specific yield and transmissivity with magnetic resonance sounding in an unconfined sandstone aquifer (Niger)", *Hydrogeology Journal*, 17, 7, 1805–1815, 2009.

[BOU 09b] BOUCHER M., FAVREAU G., DESCLOITRES M., VOUILLAMOZ J.-M., MASSUEL S., NAZOUMOU Y., CAPPELAERE B., LEGCHENKO A., "Contribution of geophysical surveys to groundwater modelling of a porous aquifer in semiarid Niger: an overview, C. R.", *Geoscience*, 341, 10–11, 800–809, 2009.

[BOU 12] BOUCHER M., FAVREAU G., NAZOUMOU Y., CAPPELAERE B., MASSUEL S., LEGCHENKO A., "Constraining groundwater modeling with Magnetic Resonance Soundings", *Journal of Ground Water*, 50(5), 775–784, 2012.

[BRA 05] BRAUN M., HERTRICH M., YARAMANCI U., "Study on complex inversion of magnetic resonance sounding signals", *Near Surface Geophysics*, 3, 155–163, 2005.

[BRA 07] BRAUN M., Influence of the resistivity on Magnetic Resonance Sounding: 1D inversion and 2D modeling, PhD Thesis, Technical University of Berlin, 2007.

[BRA 08] BRAUN M., YARAMANCI U., "Inversion of resistivity in Magnetic Resonance Sounding", *Journal of Applied Geophysics*, 66, 3–4, 151–164, 2008.

[CAL 82] CALLAGHAN P.T., LE GROS M., "Nuclear spins in the Earth's magnetic field", *American Journal of Physics 50*, 709–713, 1982.

[CAL 98] CALLAGHAN P.T., ECCLES C.D., HASKELL T.G., LANGHORNE P.J., SEYMOUR J.D., "Earth's field NMR in Antarctica: a pulsed gradient spin echo NMR study of restricted diffusion in sea ice", *Journal of Magnetic Resonance*, 133, 148–154, 1998.

[CAR 54] CARR H.Y., PURCELL E.M., "Effects of diffusion on free precession in nuclear magnetic experiments", *Physical Review*, 94, 3, 630–638, 1954.

[CHA 83] CHAVE A.D., "Numerical integration of related Hankel-transforms by quadrature and continued fraction expansion", *Geophysics*, 48, 1671–1686*,* 1983.

[CHO 08] CHO H., SONG Y.Q., "NMR measurement of the magnetic field correlation function in porous media", *Physical Review Letters*, 100, 2008.

[CHO 09] CHO H., RYU S., ACKERMAN J.L., SONG Y.Q., "Visualization of inhomogeneous local magnetic field gradient due to susceptibility contrast", *Journal of Magnetic Resonance*, 198, 88–93, 2009.

[COS 11a] COSTABEL S., YARAMANCI U., "Relative hydraulic conductivity in the vadose zone from magnetic resonance sounding – Brooks-Corey parameterization of the capillary fringe", *Geophysics*, 76(3), B1–B11, 2011.

[COS 11b] COSTABEL S., YARAMANCI U., "Relative hydraulic conductivity and effective saturation from earth's field nuclear magnetic resonance – A method for assessing the vadose zone", *Near Surface Geophysics*, 9(2), 155–167, 2011.

[DES 08] DESCLOITRES M., RUIZ L., SEKHAR M., LEGCHENKO A., BRAUN J-J., MOHAN KUMAR M.S., SUBRAMANIAN S., "Characterization of seasonal local recharge using Electrical Resistivity Tomography and Magnetic Resonance Sounding", *Hydrological Processes*, 22(3), 384–394, 2008.

[DUN 02] DUNN K.J., BERGMAN D.J., LATORRACA G.A., *Nuclear Magnetic Resonance Petrophysical and Logging Applications*, Elsevier Science Ltd., Oxford, 2002.

[EZE 10] EZERSKY M., LEGCHENKO A., CAMERLYNCK C., AL-ZOUBI A., EPPELBAUM L., KEYDAR S., BOUCHER M., CHALIKAKIS K., "The Dead Sea sinkhole hazard – new findings based on a multidisciplinary geophysical study", *Zeitschrift Fur Geomorphologie*, 54 (Suppl. 2), 69–90, 2010.

[FRE 06] FREEDMAN R., "Advances in NMR logging", *Journal of Petroleum Technology*, 58, 1, 60–66, 2006.

[FUK 81] FUKUSHIMA E., ROEDER S.B.W., *Experimental Pulse NMR: A Nuts and Bolts Approach*, Westview Press, 1981.

[CHA 08] CHALIKAKIS K., NIELSEN M.R., LEGCHENKO A., "MRS applicability for a study of glacial sedimentary aquifers in Central Jutland", *Journal of Applied Geophysics*, 66 (3–4), 176–187, Denmark, 2008.

[GEV 96] GEV I., GOLDMAN M., RABINOVICH B., RABINOVICH M., ISSAR A., "Detection of the level in fractured phreatic aquifers using nuclear magnetic resonance (NMR) geophysical measurements", *Journal of Applied Geophysics*, 34, 277–282, 1996.

[GIR 07] GIRARD J-F, BOUCHER M., LEGCHENKO A., BALTASSAT J-M., "2D magnetic resonance tomography applied to karstic conduit imaging", *Journal of Applied Geophysics*, 63 (3–4), 103–116, 2007.

[GOL 94] GOLDMAN M., RABINOVICH B., RABINOVICH M., GILAD D., GEV I., SCHIROV M., "Application of integrated NMR-TDEM method in ground water exploration in Israel", *Journal of Applied Geophysics*, 31, 27–52, 1994.

[GRO 62] GROVER F.W., *Inductance Calculations*, Dover, New York, 1962.

[GRA 65] GRANT F.S., WEST G.F., *Interpretation Theory in Applied Geophysics*, McGraw Hill Inc., New York, 1965.

[GRU 11] GRUNEWALD E., KNIGHT R., "Non-exponential decay of the surface-NMR signal and implications for water content estimation", *Geophysics*, 77, 2011.

[GRU 12] GRUNEWALD E., KNIGHT R., "The effect of pore size and magnetic susceptibility on the surface NMR relaxation parameter T_2^*", *Near Surface Geophysics*, 9, 169–178, 2011.

[GUI 02a] GUILLEN A., LEGCHENKO A., "Application of linear programming techniques to the inversion of proton magnetic resonance measurements for water prospecting from the surface", *Journal of Applied Geophysics*, 50, 149–162, 2002.

[GUI 02b] GUILLEN A., LEGCHENKO A., "Inversion of surface nuclear magnetic resonance data by an adapted Monte Carlo method applied to water resource characterization", *Journal of Applied Geophysics 50*, 193–205, 2002.

[GÜN 06] GÜNTHER T., RÜCKER C., SPITZER K., "Three-dimensional modelling and inversion of dc resistivity data incorporating topography–II. Inversion", *Geophysical Journal International*, 166, 2, 506–517, 2006.

[GÜN 12] GÜNTHER T., MÜLLER-PETKE M., "Hydraulic properties at the North Sea island Borkum derived from joint inversion of magnetic resonance and electrical resistivity soundings", *Hydrology and Earth System Sciences 9*, 2797–2829, 2012.

[JAC 99] JACKSON J.D., *Classical Electrodynamics*, Wiley, 1999.

[HAH 50] HAHN E.L., "Spin echoes", *Physical Review*, 80, 4, 580–594, 1950.

[HER 12] HERCKENRATH D., AUKEN E., CHRISTIANSEN L., BEHROOZMAND A.A., BAUER-GOTTWEIN P., "Coupled hydrogeophysical inversion using time-lapse magnetic resonance sounding and time-lapse gravity data for hydraulic aquifer testing: will it work in practice?", *Water Ressources Research*, 48, 2012.

[HER 02] HERTRICH M., YARAMANCI U., "Joint inversion of surface nuclear magnetic resonance and vertical electrical sounding", *Journal of Applied Geophysics*, 50, 179–191, 2002.

[HER 05] HERTRICH M., BRAUN M., YARAMANCI U., "Magnetic Resonance Soundings with separated transmitter and receiver loops", *Near Surface Geophysics*, 3, 141–154, 2005.

[HER 07] HERTRICH M., BRAUN M., GÜNTHER T., GREEN A., YARAMANCI U., "Surface nuclear magnetic resonance tomography", *IEEE Transactions on Geoscience and Remote Sensing*, 45, 11, 3752–3759, 2007.

[HER 08] HERTRICH M., "Imaging of groundwater with nuclear magnetic resonance", *Progress in Nuclear Magnetic Resonance Spectroscopy*, 53, 227–248, 2008.

[HÜR 98] HÜRLIMANN M.D., "Effective gradients in porous media due to susceptibility differences", *Journal of Magnetic Resonance*, 134, 232–240, 1998.

[HÜR 02] HÜRLIMANN M.D., VENKATARAMANAN L., FLAUM C., "The diffusion-spin relaxation time distribution function as an experimental probe to characterize fluid mixtures in porous media", *Journal of Chemical Physics*, 117, 22, 2002.

[KAU 83] KAUFMAN A.A., KELLER G.V., "Frequency and Transient Soundings", *Elsevier*, 1983.

[KEL 66] KELLER G.V., FRISCHKNECHT F.C., *Electrical Methods in Geophysical Prospecting*, Pergamon Press, Oxford, 1966.

[KEN 88] KENYON W.E., DAY P.I., STARLEY C., WILLEMSEN J.F., "A three-part study of NMR longtitudal relaxation properties of water-saturated sandstones", *SPE Formation Evaluation*, 622–636, September 1988.

[KEN 97] KENYON W.E., "Petrophysical Principles of Applications of NMR Logging", *The Log Analyst*, 21–43, March–April 1997.

[KLE 94] KLEINBERG R.L., KENYON W.E., MITRA P.P., "Mechanism of NMR relaxation of fluids in rock", *Journal of Magnetic Resonance*, 108, 206–214, 1994.

[KOR 62] KORRINGA J., SEEVERS D.O., TORREY H.C., "Theory of spin pumping and relaxation in systems with a low concentration of electron spin resonance centers", *The Physical Review*, 127, 1962.

[LAN 05] LANGE G., MOHNKE O., GRISSEMANN C., "SNMR measurements in Thailand to investigate low-porosity aquifers", *Near Surface Geophysics*, 197–203, 2005.

[LAC 05] LACHASSAGNE P., BALTASSAT J-M., LEGCHENKO A., DE GRAMOT H.M., "The links between MRS parameters and the hydrogeological parameters", *Near Surface Geophysics*, 3, 259–266, 2005.

[LEG 95] LEGCHENKO A., SHUSHAKOV O.A., PERRIN J., PORTSELAN A.A., "Noninvasive NMR study of subsurface aquifers in France", *Abstracts of The International Exposition and SEG'95 Annual Meeting*, Houston, 365–367, 1995.

[LEG 97] LEGCHENKO A., BEAUCE A., GUILLEN A., VALLA P., BERNARD J., "Natural variations in the magnetic resonance signal used in PMR groundwater prospecting from the surface", *European Journal of Environmental and Engineering Geophysics*, 2, 173–190, 1997.

[LEG 98a] LEGCHENKO A., SHUSHAKOV O.A., "Inversion of surface NMR data", *Geophysics*, 63, 75–84, 1998.

[LEG 98b] LEGCHENKO A., VALLA P., "Processing of proton magnetic resonance signals using non-linear fitting", *Journal of Applied Geophysics*, 39, 77–83, 1998.

[LEG 02a] LEGCHENKO A., VALLA P., "A review of the basic principles for proton magnetic resonance sounding measurements", *Journal of Applied Geophysics*, 50, 3–19, 2002.

[LEG 02b] LEGCHENKO A., BALTASSAT J.-M., BEAUCE A.,BERNARD J., "Nuclear magnetic resonance as a geophysical tool for hydrogeologists", *Journal of Applied Geophysics*, 50, 21–46, 2002.

[LEG 04a] LEGCHENKO A., "Magnetic Resonance Sounding: enhanced modeling of a phase shift", *Applied Magnetic Resonance*, 25, 621–636, 2004,

[LEG 04b] LEGCHENKO A., BALTASSAT J.-M., BOBACHEV A., MARTIN C., ROBAIN H., VOUILLAMOZ J.-M., "Magnetic resonance sounding applied to aquifer characterization", *Ground Water*, 42, 363–373, 2004.

[LEG 06] LEGCHENKO A., DESCLOITRES M., BOST A., RUIZ L., REDDY M., GIRARD J-F., SEKHAR M., KUMAR M.S., BRAUN J-J., "Resolution of MR Soundings applied to the characterization of hard rock aquifers", *Journal of Ground Water*, 44, (4), 547–554, 2006.

[LEG 08] LEGCHENKO A., EZERSKY M., CAMERLINK C., AL-ZOUBI A., CHALIKAKIS K., GIRARD J-F., "Locating water-filled karst caverns and estimating their volume using magnetic resonance soundings", *Geophysics*, 73, (5), 51–61, 2008.

[LEG 10] LEGCHENKO A., VOUILLAMOZ J.-M., ROY J., "Application of the magnetic resonance sounding method to the investigation of aquifers in the presence of magnetic material", *Geophysics*, 75 (6), 2010.

[LEG 11a] LEGCHENKO A., DESCLOITRES M., VINCENT C., GUYARD H., GARAMBOIS S., CHALIKAKIS K.,EZERSKY M., "Three-dimensional magnetic resonance imaging for groundwater", *New Journal of Physics*, 13, 2011.

[LEG 11b] LEGCHENKO A., CLÉMENT R., GARAMBOIS S., MAURY E., MIC L-M., LAURENT J-P., DESPLANQUE C., GUYARD H., "Locating water storage of the Luitel lake peat bog using MRS, ERT and GPR", *Near Surface Geophysics*, 9, 201–209,2011.

[LEE 74] LEE T., LEWIS R., "Transient response of a large loop on a layered earth", *Geophysical Prospecting*, 22, 430–444, 1974.

[LEH 11a] LEHMANN-HORN J.A., HERTRICH M., GREENHALGH S.,GREEN A.G., "Three-dimensional magnetic field and nmr sensitivity computations incorporating conductivity anomalies and variable-surface topography", *IEEE Transactions on Geoscience and Remote Sensing*, 49(10), 3878–3891, 2011.

[LEH 11b] LEHMANN-HORN A., WALBRECKER J.O., HERTRICH M., LANGSTON G., MCCLYMONT A.F., GREEN A.G., "Imaging groundwater beneath a rugged proglacial moraine", *Geophysics*, 76, B165–B172, 2011.

[LIE 94] LIEBLICH D.A., LEGCHENKO A., HAENI F.P., PORTSELAN A., "Surface nuclear magnetic resonance experiments to detect subsurface water at Haddam Meadows", *Proceedings of the Symposium on the Application of Geophysics to Engineering and Environmental Problems, Boston, Massachusetts*, 2, 717–736, Connecticut, 27–31 March 1994.

[LUB 04] LUBCZYNSKI M., ROY J., "Magnetic Resonance Sounding: new method for ground water assessment", *Ground Water*, 42, 291–303, 2004.

[LUB 05] LUBCZYNSKI M., ROY J., "MRS contribution to hydrogeological system parametrization", *Near Surface Geophysics*, 3, 131–139, 2005.

[MAN 79] MANSFIELD P., MAUDSLEY A.A., MORRIS P.G., PYKETT I.L., "Selective pulses in NMR imaging: replay to criticism", *Journal of Magnetic Resonance*, 33, 261–274, 1979.

[MAJ 86a] MAJUMDAR S., ORPHANOUDAKIS S.C., GMITRO A., O'DONNELL M., GORE J.C., "Errors in the measurements of T_2 using multiple-echo MRI techniques. I. Effects of radiofrequency pulse imperfections", *Magnetic Resonance in Medicine*, 3(3), 397–417, 1986.

[MAJ 86b] MAJUMDAR S., ORPHANOUDAKIS S.C., GMITRO A., "Errors in the measurements of T_2 using multiple-echo MRI techniques. II. Effects of static field inhomogeneity", *Magnetic Resonance in Medicine*, 3 (4), 562–574, 1986.

[MAR 86] MARSYLI G., *Quantitative Hydrogeology*, Academic Press Inc., San Diego, California, 1986.

[MEI 58] MEIBOOM S., GILL D., "Modified spin-echo method for measuring nuclear relaxation times", *Review of Scientific Instruments,* 29, 688–691,1958.

[MIC 10] MICHAL C.A., "A low-cost spectrometer for NMR measurements in the Earth's magnetic field", *Measurement Science and Technology*, 21, 2010.

[MOH 02] MOHNKE O., YARAMANCI U., "Smooth and block inversion of surface NMR amplitudes and decay times using simulated annealing", *Journal of Applied Geophysics*, 50, 163–177, 2002.

[MOH 05] MOHNKE O., YARAMANCI U., "Forward modeling and inversion of MRS relaxation signals using multi-exponential decomposition", *Near Surface Geophysics*, 3, 165–185, 2005.

[MOO 20] MOORE E.H., "On the reciprocal of the general algebraic matrix", *Bulletin of the American Mathematical Society*, 26, 394–395, 1920.

[MÜL 08] MÜLLER-PETKE M., YARAMANCI U., "Resolution studies for Magnetic Resonance Sounding (MRS) using the singular value decomposition", *Journal of Applied Geophysics*, 66, 165–175, 2008.

[MÜL 10] MUELLER-PETKE M., YARAMANCI U., "QT inversion – comprehensive use of the complete surface NMR data set", *Geophysics*, 75, 4, 2010.

[MÜL 11] MÜLLER-PETKE M., DLUGOSCH R., YARAMANCI U., "Evaluation of Surface Nuclear Magnetic Resonance estimated subsurface water content", *New Journal of Physics*, 13, 2011.

[NEL 94] NELSON P.H., "Permeability-porosity relationships in sedimentary rocks", *The Log Analyst*, 38–62, May–June 1994.

[NEL 05] NELSON P.H., "Permeability, porosity and pore-throat size – a three-dimensional perspective", *Petrophysics*, 46, 452–455, 2005.

[NEU 74] NEUMAN C.H., "Spin echo of spins diffusing in a bounded medium", *Journal of Chemical Physics*, 60, 4508, 1974.

[NIE 11] RYOM NIELSEN M., HAGENSEN T.F., CHALIKAKIS K., LEGCHENKO A., "Comparison of transmissivities from MRS and pumping tests in Denmark", *Near Surface Geophysics*, 9, 211–223, 2011.

[PAC 54] PACKARD M., VARIAN R., "Free nuclear induction in the earth's magnetic field", *Physical Review*, 93, 941, 1954.

[PLA 08] PLATA J, RUBIO F., "The use of MRS in the determination of hydraulic transmissivity: the case of alluvial aquifers", *Journal of Applied Geophysics*, 66, 128–139, 2008.

[POM 08] POMERANTZ A.E., SONG Y.Q., "Quantifying spatial heterogeneity from images", *New Journal of Physics*, 10, 221–231, 2008.

[PEN 55] PENROSE R., "A generalized inverse for matrices", *Proceedings of the Cambridge Philosophical Society*, 51, 406–413, 1955.

[PUR 46] PURCELL E., TORREY H., POUND R., "Resonance absorption by nuclear magnetic moments in a solid", *Physical Review*, 69, 37, 1946.

[ROM 98] ROMANOV V.G, GOTTLIEB J., "Joint inversion of transient electromagnetic and proton resonance surface data by coupled Maxwell's and Bloch's equations", *Journal of Inverse and Ill-Posed Problems*, 6, 3, 263–279, 1998.

[ROY 03] ROY J., LUBCZYNSKI M., "The magnetic resonance sounding technique and its use for groundwater investigations", *Hydrogeology Journal*, 11, 455–465, 2003.

[ROY 05] ROY J., LUBCZYNSKI M., "MRS multi-exponential decay analysis: aquifer pore size distribution and Vadose zone characterization", *Near Surface Geophysics*, 3(4), 287–298, 2005.

[RYU 70] RYU J., MORRISON F., WARD S., "Electromagnetic fields about a loop source of current", *Geophysics*, 35, 862–896, 1970.

[SCH 91] SCHIROV M., LEGCHENKO A., CREER G., "New direct non-invasive ground water detection technology for Australia", *Exploration Geophysics*, 22, 333–338, 1991.

[SCH 98] SCHÖN J.H., *Physical properties of rocks: fundamentals and principles of petrophysics*, 2nd ed., Pergamon, 583, 1998.

[SEM 89] SEMENOV A.G., SCHIROV M.D., LEGCHENKO A., BURSHTEIN A.I., YU A., PUSEP A.J., Device for measuring the parameter of underground mineral deposit, Patent number GB2198540, 1989.

[SEN 86] SENGERS J.V., WATSON J.T.R., "Improved international formulations for the viscosity and thermal conductivity of water substance", *Journal of Physical and Chemical Reference Data*, 15, 1291, 1986.

[SEE 66] SEEVERS D.O., "A nuclear magnetic method for determining the permeability of sandstones", *Paper L, in Annual Logging Symposium Transactions: Society of Professional Well Log Analysts*, 1966.

[SHU 96] SHUSHAKOV O.A., "Groundwater NMR in conductive water", *Geophysics*, 61, 998–1006, 1996.

[SIN 05] SINGH N.P., MOGI T., "Electromagnetic response of a large circular loop source on a layered earth: a new computation method", *Pure and Applied Geophysics*, vol. 162, 1, 181–200, 2005.

[SMY 50] SMYTHE W.R., *Static and Dynamic Electricity*, McGraw-Hill, New York, 1950.

[STE 90] STEPIŠNIK J., ERŽEN V., KOS M., "NMR imaging in the Earth's magnetic field", *Magnetic Resonance in Medicine*, 15, 3, 386–391, 1990.

[STO 80] STOER J., BULIRSCH R., *Introduction to Numerical Analysis*, Springer-Verlag, Berlin, 1980.

[SUK 01] SUKSTANSKII A.L., YABLONSKIY D.A., "Theory of FID NMR signal dephasing induced by mesoscopic magnetic field inhomogeneities in biological systems", *Journal of Magnetic Resonance*, 151, 107–117, 2001.

[SUN 02] SUN B., DUNN K.J., "Probing the internal field gradients of porous media", *Physical Review E*, 65, 2002.

[TAR 05] TARANTOLA A., "Inverse problem theory and methods for model parameter estimation", *Society for Industrial and Applied Mathematics (SIAM),* Philadelphia, 2005.

[TAI 02] TAICHER G.Z., NMR logging in the Earth's magnetic field, US patent WO/2002/086541, 2002.

[TIK 77] TIKHONOV A., ARSENIN V., *Solution of Ill-posed Problems*, John Wiley & Sons, Inc., 1977.

[TRU 95] TRUSHKIN D.V., SHUSHAKOV O.A., LEGCHENKO A., "Surface NMR applied to an electroconductive medium", *Geophysical Prospecting*, 43, 623–633,1995.

[VAL 02] VALLA P., LEGCHENKO A., "One-dimensional modelling for proton magnetic resonance sounding measurements over an electrically conductive medium", *Journal of Applied Geophysics*, 50, 217–229, 2002.

[VAR 62] VARIAN R.H., Ground liquid prospecting method and apparatus, US patent 3019383, 1962

[VIN 12] VINCENT C., DESCLOITRES M., GARAMBOIS S., LEGCHENKO A., GUYARD H., LEFEBVRE E., GILBERT A., "Detection of a subglacial lake in Glacier de Tete Rousse (Mont Blanc area, France)", *Journal of Glaciology*, 58, 211, 866–878, 2012.

[VOU 02] VOUILLAMOZ J.-M., DESCLOITRES M., BERNARD J., FOURCASSIÉ P., ROMAGNY L., "Application of integrated magnetic resonance sounding and resistivity methods for borehole implementation. A case study in Cambodia", *Journal of Applied Geophysics*, 50, 67–81, 2002

[VOU 03] VOUILLAMOZ J.-M., LEGCHENKO A., ALBOUY Y., BAKALOWICZ M., BALTASSAT J.-M., AL-FARES W., "Localization of saturated karst aquifer with magnetic resonance sounding and resistivity imagery", *Ground Water*, 41, 578–587, 2003.

[VOU 05] VOUILLAMOZ J.-M., DESCLOITRES M., TOE G., LEGCHENKO A., "Characterization of crystalline basement aquifers with MRS: comparison with boreholes and pumping test data in Burkina Faso", *Near Surface Geophysics*, 3, 205–213, 2005.

[VOU 07a] VOUILLAMOZ J.-M., CHATENOUX B., MATHIEU F., LEGCHENKO A., "Efficiency of joint use of MRS and VES to characterize coastal aquifer in Myanmar", *Journal of Applied Geophysics*, 61 (2), 142–154, 2007.

[VOU 07b] VOUILLAMOZ J.-M., BALTASSAT J.M., GIRARD J.F., PLATA J., LEGCHENKO A., "Hydrogeological experience in the use of MRS", *Boletin Geológico y Minero*, 118 (3), 531–549, 2007.

[VOU 08] VOUILLAMOZ J.-M., FAVREAU G., MASSUEL S., BOUCHER M., NAZOUMOU Y., LEGCHENKO A., "Contribution of magnetic resonance sounding to aquifer characterization and recharge estimate in semiarid Niger", *Journal of Applied Geophysics*, 64 (3–4), 99–108, 2008.

[VOU 11] VOUILLAMOZ J.-M., LEGCHENKO A., NANDAGIRI L., "Characterizing aquifers when using magnetic resonance sounding in a heterogeneous geomagnetic field", *Near Surface Geophysics*, 9, 135–144, 2011.

[VOU 12a] VOUILLAMOZ J.-M., HOAREAU J., GRAMMARE M., CARON D., NANDAGIRI L., LEGCHENKO A., "Quantifying aquifer properties and freshwater resource in coastal barriers: a hydrogeophysical approach applied at Sasihithlu (Karnataka, India)", *Hydrology and Earth System Sciences*, 16, 4387–4400, 2012.

[VOU 12b] VOUILLAMOZ J.-M., SOKHENG S., BRUYERE O., CARON D., ARNOUT L., *Journal of Hydrology*, 458–459, 51–58, http://dx.doi.org/10.1016/j.jhydrol.2012.06.044, 2012.

[WAI 82] WAIT J.R., *Geo-Electromagnetism*, Academic Press, 1982.

[WAL 08] WALSH D.O., "Multi-channel surface NMR instrumentation and software for 1D/2D groundwater investigations", *Journal of Applied Geophysics*, 66, 140–150, 2008.

[WAL 11] WALBRECKER J.O., HERTRICH M., GREEN A.G., "Off-resonance effects in surface nuclear magnetic resonance", *Geophysics*, 76, G1–G12, 2011.

[WAN 84] WANNAMAKER P.E., HOHMANN G.W., SAN FILIPO W.A., "Electromagnetic modeling of three-dimensional bodies in layered earths using integral equations", *Geophysics*, 49, 60–74, 1984.

[WAR 88] WARD S.H., HOHMANN G.W., "Electromagnetic theory for geophysical applications, in electromagnetic methods in applied geophysics", *Society of Exploration Geophysicists*, Tulsa, 1988.

[WEI 75] WEIDELT P., "Electromagnetic induction in three-dimensional structures", *Journal of Geophysics*, 41, 85–109, 1975.

[WEI 00] WEICHMAN P.B., LAVELY E.M., RITZWOLLER M.H., "Theory of surface nuclear magnetic resonance with applications to geophysical imaging problems", *Physical Review*, 62, 1290–1312, 2000.

[WEI 02] WEICHMAN P.B., LUN D.R., RITZWOLLER M.H., LAVELY E.M., "Study of surface nuclear magnetic resonance inverse problems", *Journal of Applied Geophysics 50*, 129–147, 2002.

[WEI 05] WEIDELT P., "Geoelektrik Grundlagen", KNÖDEL K., KRUMMEL H., LANGE G. (eds), *Handbuch zur Erkundung des Untergrundes von Deponien. Geophysik*, 3, Springer-Verlag, Berlin Heidelberg, 71–100, 2005.

[WYN 04] WYNS R., BALTASSAT J.M., LACHASSAGNE P., LEGTCHENKO A., VAIRON J., "Application of proton magnetic resonance soundings to groundwater reserve mapping in weathered basement rocks (Brittany, France)", *Bulletin de la Société Géologique de France*, 1, 175, 21–34, 2004.

[XIO 89] XIONG Z., "Electromagnetic fields of electric dipoles embedded in a stratified anisotropic earth", *Geophysics*, 54, 1643–1646, 1989.

[ZHA 01] ZHANG G.Q, HIRASAKI G.J., HOUSE W.V., "Effect of internal field gradients on NMR measurements", *Petrophysics*, 42, 37–47, 2001.

[ZHD 09] ZHDANOV M.S., *Geophysical Electromagnetic Theory and Methods*, Oxford, Elsevier, 2009.

Index

1–D, 1, 11, 12, 47, 59, 60, 67, 68, 76–79, 81, 86, 92, 94, 102, 106, 107, 109, 112–113, 117, 128–129, 138, 142
2–D, 1, 11–12, 81, 86, 92, 129, 138, 142

A, B, C

amplitude, 3–4, 6–9, 18, 30–32, 34–39, 41–43, 54, 57, 60–67, 69–82, 86, 92–93, 96– 98, 102–103, 107–108, 113–114, 118, 127, 136–137
aquifer, 6–8, 12–13, 58, 60, 68, 80, 121–126, 128–129, 132–133, 135–142
B_0, 5, 55
B_1, 5, 23, 24, 25
Bloch equations, 17–19, 22, 25, 45, 47–48, 50, 57
Boltzmann constant, 17
bound water, 124, 131–132, 138
coil, 2, 4, 31, 49
coincident, 8, 49, 52, 59, 87, 107, 112
condition number, 101, 112
confidence intervals, 100, 103–105, 112
confined aquifer, 123, 125, 133
conjugate gradient method, 115
co-rotating component, 18
covariance, 94, 100, 103–104, 110
  matrix, 94, 100, 103–104, 110
CPMG method, 42–44
current pulse, 9, 51, 86, 87

D, E, F

data acquisition, 2
DC, 118, 138
depth of investigation, 7, 9, 66–67, 73, 81, 82, 105, 122, 128
detection, 1, 2, 4, 12, 81, 93, 123, 126
diffusion, 26–31, 41–43, 68
  coefficient, 27, 42
discretization, 12, 86, 92, 94–96, 102, 105, 107, 110, 112
elastic storativity, 125, 133–134
electromagnetic field, 2, 6, 45, 118
electromagnetic noise, 3, 12
elliptically polarized, 47–48, 52
enhanced relaxation, 27–30
envelope, 8, 32, 41, 43, 77, 80, 90
equilibrium spin magnetization, 17
equipment, 1, 5, 59
ERT, 81, 82, 141–142
experimental, 12, 29, 31, 48, 76–79, 81–83, 85–86, 90, 93, 100, 114, 116, 118, 127, 129, 133, 136–139
  verification, 76, 83, 127, 133, 137, 138

FID, 31–33, 39, 50, 58–59, 67–68, 76–80, 82, 86, 127
field setup, 8, 11, 45, 89, 105
flip angle, 6, 20, 32–34, 36–37, 39–41, 51
flow related parameters, 124
Fredholm integral equation, 92
free induction decay, 8, 31, 58, 59
free water, 124–125, 132

G, H, I

geomagnetic field, 2, 5–7, 19, 48, 54, 57, 58, 60, 64, 73–76, 78, 80, 116
groundwater, 1, 2, 4, 6, 8, 12–14, 48, 121–122, 126–127, 129, 131–132
gyromagnetic ratio, 2, 6, 15, 16, 26
H^1, 2
heterogeneous, 38, 53, 127, 129
homogeneous magnetic field, 17, 57
hydraulic conductivity, 12–13, 123, 125, 134–135, 140, 142
hydraulic head, 125
hydrogen, 2, 4, 15
hydrostatic water column, 125
identified, 128, 131, 135
identity matrix, 101, 102
imaginary, 21, 103, 107
imaging equation, 45, 51–52, 76, 83, 87–89
immobile water, 124
interpolated, 142
inverse problem, 85–87, 89, 91–92, 98, 99, 102, 105, 107, 109, 112–113, 115, 118, 121, 128, 131
inversion, 8, 12, 13, 33–34, 77, 80–82, 85, 86, 90, 91, 92, 94, 97, 100–107, 109–119, 127–131, 136, 138
  recovery, 33, 34

J, L, M

joint interpretation, 138, 140
joint inversion, 115, 138
laboratory frame, 17, 18
Larmor frequency, 2–3, 6–7, 16, 18, 20, 26–27, 32, 38, 45, 49–50, 59, 64–68, 76, 78, 86–87, 89, 116–117
least squares, 98, 100, 113, 115, 117
linear, 3, 13, 89, 91–92, 94, 97–98, 104, 109, 110, 113, 115, 117, 133
linearization, 89, 115
linearly dependent, 95, 109
linearly polarized, 18, 47, 50
logging, 121, 136
longitudinal relaxation time, 22
loop, 4–12, 45–54, 57, 59, 63, 66–76, 78, 81, 86–87, 89–90, 105, 107, 108, 113, 118, 126–129
macroscopic, 2, 5–7, 16, 17, 24, 40, 48
magnetic field, 2–6, 8–10, 15–29, 31, 36, 41–42, 46–55, 57, 59–61, 63–76, 83, 86–87, 89, 116–118, 121, 127, 134
  gradient, 27–29, 32, 41–42, 83
magnetic moments, 2, 23–24, 26, 27, 38
Magnetic Resonance Sounding (MRS), 1, 5–8, 128, 139
Magnetic Resonance Tomography, 1
magnetic rock, 57–58, 76, 116, 127, 139
magnetization, 16, 20–25, 32–35, 37, 39, 40
measurement, 2–4, 6–7, 11, 31, 38, 47, 49, 51, 54, 57– 59, 67, 76–77, 79–83, 85–92, 115–118, 127–128, 134–135, 138
measuring setup, 8, 10, 59, 105, 107, 113, 131

minimum length solution, 100
model resolution, 100–104, 109–110
modified saturation recovery, 36–38, 88

N, P, R

non-homogeneous magnetic field, 26
non-invasive, 1, 2, 12, 121
nonlinear, 89, 115, 118–119, 133
normal distribution, 100
nuclear, 1, 2, 15, 21–22, 26, 30, 32–35, 37–39, 42, 53, 88
  magnetization, 21, 30, 32–35, 37–39, 42, 53, 88
Nuclear Magnetic Resonance (NMR), 1, 2, 4–6, 9, 15–17, 21–22, 25–27, 31, 34, 36–38, 45, 48, 57, 58, 76, 83, 86, 121, 131, 134–136
parameter, 12, 13, 57, 68, 87, 100, 116, 137
phase, 2, 3, 21, 23–25, 32, 48, 50, 52, 54, 62–64, 66, 77–82, 86, 97, 102, 103, 113
Planck constant, 17
porosity, 13, 80, 122, 124–127, 131, 133–134, 138, 140
porous media, 28, 31, 76, 121, 125, 131, 134–135
property, 2, 13, 16, 85, 86
protons, 2, 4, 6, 7, 15, 17, 93
pseudoinverse, 99, 100
pulse moment, 8, 51, 59, 61, 62, 64–67, 78–82, 86–89, 91, 93–96, 102, 105, 107, 116–117, 127, 136–137
real, 21, 88, 92, 103, 107, 118, 131
receiving, 8, 9, 45, 49, 51–53, 87, 105
regularization, 113
resistivity, 60, 139, 142
resolution, 5, 11, 13, 83, 86, 97, 98, 100–101, 103–107, 110–113, 121, 128, 129, 131, 135
resonance conditions, 20, 22, 41, 50, 66, 77, 89, 116
response, 2–4, 6, 13, 45, 53, 61, 62, 64, 83, 86, 121, 126
RMP, 1
rotating frame, 18, 20, 25, 38, 49, 50, 53
Rx, 8, 10, 49, 51–53, 59, 81, 87, 89, 105, 107

S

S/N, 9
saturation recovery, 33, 35–36, 88
SE, 38–42, 58, 67–68, 76–79, 86, 88–89, 127
sensitivity, 6, 12, 68, 72–74, 76, 112–113, 121, 127
signal, 2, 3, 4, 6–10, 12–14, 21, 25, 27, 31–42, 45, 49–50, 54, 57–83, 86, 89–94, 96–97, 102–103, 105, 107–108, 116–118, 126–127, 135–137
signal-to-noise ratio, 3–4, 9–10, 13, 81
singular value decomposition, 98
smoothing factor, 114
SNMR, 1–9, 11–14, 45, 47, 48, 49, 53, 54, 57–83, 85–92, 94– 97, 102–103, 105–109, 111–113, 115–119, 121, 122, 126–129, 131–138, 140–142
sounding, 6–8, 59, 82, 96
specific retention, 125
specific yield, 125, 132–134, 138
spike test, 104–105, 112
spin echo, 26, 38, 39, 40–43, 58, 68, 127

spin magnetization, 8, 16–25, 40, 48
spin-lattice relaxation time, 18
spin-spin relaxation time, 18
square loop, 2, 8, 9, 60, 66–68, 70, 72, 74–76, 80–81, 93, 95, 96, 107, 112, 128
static magnetic field, 2, 4–6, 21, 22, 25–31, 33, 38, 44, 48, 57, 121
static water level, 123, 129, 141
storage related parameters, 124, 134
storativity, 134
subsurface, 1–2, 4, 8, 12–14, 45, 47–50, 52–54, 59, 60, 63, 66–68, 73, 74, 76, 81, 85, 86, 90–91, 93– 95, 97, 105, 107, 113, 116–118, 121, 128, 129, 139, 142
surface, 1, 4, 6, 8, 13, 36, 45, 47–49, 54, 58, 68, 80–81, 118, 123, 126, 127, 131–132, 133, 135
SVD, 98–99, 102–104, 107, 109–112
SWL, 123

T, U, W

T_1, 33–38, 60, 62–63, 82
T_2, 24–25, 29, 30, 43, 61–66
TDEM, 80, 81, 90, 128, 138
Tikhonov regularization, 113
tomography, 81, 115, 141
transmitting, 2, 8–10, 39, 45, 49, 51, 53, 86, 87, 90, 105
transverse relaxation time, 42
trapped water, 124, 133–134
truncated SVD, 99
Tx, 8, 9, 10, 49, 51–53, 59, 81, 87, 89, 105, 107
uncertainty, 13, 100, 103–104, 111, 113, 127–129, 132, 134, 138
unconfined aquifer, 122, 129
water content, 8, 12, 13, 50, 58, 80–82, 86–87, 93, 108, 112–114, 118–119, 124, 126, 128, 131–140, 142
water level, 80, 123, 126, 142
water table, 123